National Library
of Canada

Acquisitions and
Bibliographic Services Branch

395 Wellington Street
Ottawa, Ontario
K1A 0N4

Bibliothèque nationale
du Canada

Direction des acquisitions et
des services bibliographiques

395, rue Wellington
Ottawa (Ontario)
K1A 0N4

Your file *Votre référence*

Our file *Notre référence*

NOTICE

The quality of this microform is heavily dependent upon the quality of the original thesis submitted for microfilming. Every effort has been made to ensure the highest quality of reproduction possible.

If pages are missing, contact the university which granted the degree.

Some pages may have indistinct print especially if the original pages were typed with a poor typewriter ribbon or if the university sent us an inferior photocopy.

Reproduction in full or in part of this microform is governed by the Canadian Copyright Act, R.S.C. 1970, c. C-30, and subsequent amendments.

AVIS

La qualité de cette microforme dépend grandement de la qualité de la thèse soumise au microfilmage. Nous avons tout fait pour assurer une qualité supérieure de reproduction.

S'il manque des pages, veuillez communiquer avec l'université qui a conféré le grade.

La qualité d'impression de certaines pages peut laisser à désirer, surtout si les pages originales ont été dactylographiées à l'aide d'un ruban usé ou si l'université nous a fait parvenir une photocopie de qualité inférieure.

La reproduction, même partielle, de cette microforme est soumise à la Loi canadienne sur le droit d'auteur, SRC 1970, c. C-30, et ses amendements subséquents.

Canada

University of Alberta

Mid-Span Optical Time-Domain Reflectometry

by

Samson Shun-Tong Lee

A thesis submitted to the Faculty of Graduate Studies and Research in partial fulfillment of the requirements for the degree of Master of Science.

Department of Electrical Engineering

Edmonton, Alberta

Spring, 1993.

National Library
of Canada

Acquisitions and
Bibliographic Services Branch

395 Wellington Street
Ottawa, Ontario
K1A 0N4

Bibliothèque nationale
du Canada

Direction des acquisitions et
des services bibliographiques

395, rue Wellington
Ottawa (Ontario)
K1A 0N4

Your file Votre référence

Our file Notre référence

The author has granted an irrevocable non-exclusive licence allowing the National Library of Canada to reproduce, loan, distribute or sell copies of his/her thesis by any means and in any form or format, making this thesis available to interested persons.

L'auteur a accordé une licence irrévocable et non exclusive permettant à la Bibliothèque nationale du Canada de reproduire, prêter, distribuer ou vendre des copies de sa thèse de quelque manière et sous quelque forme que ce soit pour mettre des exemplaires de cette thèse à la disposition des personnes intéressées.

The author retains ownership of the copyright in his/her thesis. Neither the thesis nor substantial extracts from it may be printed or otherwise reproduced without his/her permission.

L'auteur conserve la propriété du droit d'auteur qui protège sa thèse. Ni la thèse ni des extraits substantiels de celle-ci ne doivent être imprimés ou autrement reproduits sans son autorisation.

ISBN 0-315-82237-6

Canada

The University of Alberta

Release Form

Name of Author:	**Samson Shun-Tong Lee**
Title of Thesis:	**Mid-Span Optical Time-Domain Reflectometry**
Degree:	**Master of Science**
Year this degree granted:	**Spring, 1993**

Permission is hereby granted to The University of Alberta Library to reproduce single copies of this thesis and to lend or sell such copies for private, scholarly or scientific research purposes only.

The author reserves other publication and other rights in association with the copyright in the thesis, and except as hereinbefore provided, neither the thesis nor any substantial portion thereof may be printed or otherwise reproduced in any material whatsoever without the author's prior written permission.

Samson Lee

4665 W. 16th Avenue,
Vancouver, British Columbia,
Canada, V6R 3E9

Date: 18/DECEMBER/1992

"The day will yet come when the progress of research through long ages will reveal to sight the mysteries of nature that are now wholly concealed. A single lifetime, though it were wholly devoted to the study of the sky, does not suffice for the investigation of problems of such complexity [as those of astronomy]. ... The day will yet come when posterity will be amazed that we remained ignorant of things that will to them seem so plain."

— Seneca: *Quaestiones Naturales*

"I have offended God and mankind because my work didn't reach the quality it should have."

— [*attributed to*] Leonardo da Vinci

"I can't give you a brain, but I can give you a degree."

— The Wizard of Oz

University of Alberta

Faculty of Graduate Studies and Research

The undersigned certify that they have read, and recommend to the Faculty of Graduate Studies and Research for acceptance, a thesis entitled **Mid-Span Optical Time-Domain Reflectometry**, submitted by **Samson Shun-Tong Lee** in partial fulfillment of the requirements for the degree of **Master of Science**.

Dr. R. Ian MacDonald (co-supervisor)

Dr. James N. McMullin (co-supervisor)

Dr. Jan Conradi (internal examiner)

Dr. James P. Pinfold (external examiner)

Date: 18 December, 1992.

To my parents and my sister, who gave me
understanding, encouragement and support.

Abstract

Optical time-domain reflectometry (OTDR) for non-intrusively testing optical fibres in mid-span has been shown to be feasible. The study used a model which accounts for effects of non-intrusive tapping. The model is based on a fibre backscattering impulse response that includes effects of common discrete transmission and reflection characteristics of an optical fibre. Quantitative studies accomplished with a simulator based on this impulse response helped define a target system. The adaptation of local detection techniques for high (electrical) frequency operation was identified as the area for the most intensive investigation. An efficient, consistent, non-intrusive tap compatible with wavelengths from 800 nm to 1550 nm was produced. It taps 30% (or more) of light in a fibre out of a macro-bend and couples up to 30% of the tapped light to a photodetector with a 0.5-mm active diameter. Two pre-amplifiers were designed to accommodate the larger than normal photodetector and its associated capacitance. One was built entirely with commercially available components. The other was a custom design. Further calculation and simulation confirmed the viability of mid-span OTDR with our bend-tap and receiver combination.

Acknowledgement

I would like to thank Dr. Ian MacDonald who gave me a first experience of research in my undergraduate years and the opportunity of graduate studies, for his understanding, trust and faith in my ability, for intellectual and financial support.

Equal gratitude is extended to Dr. James McMullin for his help with the physical aspects of my research, for lending me his various bend-tap prototypes, for his support and for his patience and confidence in me.

Sincere thanks go to other members of my examination committee, Dr. Jan Conradi and Dr. James Pinfold, for taking time to read and correct my thesis.

Deep appreciation is expressed toward Telecommunications Research Laboratories (TRLabs) for financial support and a unique educational opportunity. The staff at TRlabs has been amiable and has *withstood* my immaturity. In particular, I thank Nona McDonagh for providing me with help with the word processor and for handling the distribution of copies of my thesis (and not actually holding me responsible for my spiders).

Recognition goes to Dr. Barrie Keyworth and Rohit Sharma for their help with packaging the broad-area quantum-well laser diodes. Much is owed to David Clegg, Laboratory Manager at TRLabs (Edmonton), for technical support and practical suggestions which have shortened many learning processes.

I would like to thank David Patrosky of Alberta Government Telephone (AGT), whose proposal led to the genesis of my research project, and Hilton Sinclaire, also of AGT, for initial help with fibre systems.

Peter Pilon, John spencer and Shawn Morrison, all of Northern Telecom, Saskatoon, SK., deserve thanks for their material and technical contributions to this project.

I also thank Christy Cholak, my proof-reader, for her suggestions to the non-technical aspects of my thesis. Lastly, I would like to express my appreciation for my fellow students at TRLabs who provided most of the interesting incidents. In particular, I thank Terrence Rosadiuk, who gave me a few good suggestions, for being a good source of data sheets and a good office-mate, and Dobby Lam for his help at various time.

Table of Contents

List of Tables
List of Figures
List of Symbols

CHAPTER 1 Introduction 1

1.1 The Need for Optical Reflectometry 1
1.2 Optical Time-Domain Reflectometry 2
1.3 Modern OTDR 3
1.4 Inconveniences in Using OTDR 5
1.5 Local Detection through Bending 6
1.6 The Objectives of this Thesis 7
1.7 The Organisation of this Thesis 7

CHAPTER 2 Theories of Optical Time-Domain Reflectometry 8

2.1 Relevant Properties of Optical Fibres 8
2.1.1 Attenuation 8
2.1.2 Fresnel Reflection 10
2.1.3 Rayleigh Scattering 11
2.2 Equations of OTDR 11
2.2.1 The impulse response of fibre backscattering 12
2.2.2 Receiver characteristics 15
2.2.3 Signal processing gains 19
2.2.4 The range equation (OTDR maker's formula) 20
2.3 A Simulated OTDR 22
2.3.1 From ideal fibre response to practical fibre response 22
2.3.2 The simulation system 23
2.4 The Merits (and Demerits) of Local Launch 27
2.5 Summary and Directions 29

CHAPTER 3 Local Detection 30

3.1 Leakage Through A Fibre Bend 30

3.2 Power Distribution of Leakage 32

3.3 Bend Tap 35

3.3.1 The Identifiber window 36

3.3.2 Modifications to the identifiber window 37

3.3.3 Summary of ray tracing matrices 39

3.3.4 Bend tap with GRIN lenses 40

3.4 Local Launch 44

3.5 Summary 47

CHAPTER 4 Electronics 48

4.1 Detector Choice and Receiver Design Target 48

4.1.1 Influences of detector capacitance 48

4.1.2 Detector choice 49

4.1.3 Receiver Design Targets 50

4.2 Pre-amplifier Topology 51

4.3 A Simple Receiver Design 52

4.4 Desensitised Pre-amplifier 53

4.4.1 General feedback amplifiers 54

4.4.2 Transimpedance pre-amplifier 56

4.4.3 Noise Considerations 57

4.4.4 The final design 59

4.5 Summary 66

CHAPTER 5 Summary and Prospects 67

5.1 Summary 67

5.2 Current Standing 69

5.2.1 Head-launched OTDR 69

5.2.2 Local-launched OTDR 71

5.3 Prospects 72

References 73

Appendices 77

A Derivation of the correction factor for Rayleigh scattering capture ratio in a large-core fibre 78

B Expanded block diagrams of simulation subsystems 80

B.1 Pulse generator 80

B.2 Laser 80

B.3 White Noise 81

B.4 Fiber 82

C Ray matrices used as building blocks in this thesis 83

C.1 Basic Ray Matrices 84

C.2 Graded-index lens with curved entry and exit surfaces. 85

D GRIN lens data 87

E Photo-detector specifications 88

E.1 NEC NDL2208 88

E.2 Epitaxx ETX 500T 89

E.3 EG&G C30619 90

E.4 Detector packages 90

F Amplifier specifications 91

F.1 Transistors 91

F.2 Packaged amplifiers 100

G Circuit design documentation 106

G.1 Driver for quantum-well laser diodes 106

G.2 OTDR Receiver Revision C 111

List of Tables

	Title	*Page*
Table 1	Measured pre-amplifier bandwidths	62
Table 2	Specifications on GRIN lenses	87
Table 3	Specifications of NDL2208 silicon p-i-n photo-diode under 10V reverse bias	88
Table 4	Specifications of C30619E p-i-n InGaAs photo-diode under 5V reverse bias	89
Table 5	Specifications of C30619E p-i-n InGaAs photo-diode under 5V reverse bias	90
Table 6	Part List for High Current Laser Driver, Revision B	109
Table 7	Part List for OTDR Receiver, Revision C	114

List of Figures

	Title	*Page*
Fig. 1•1	General configuration of an optical time-domain reflectometer.	2
Fig. 1•2	Time needed to measure 0.1-dB faults versus two-way range, for different sequence lengths in a correlating OTDR.	4
Fig. 2•1	Intrinsic attenuation of silica-based fibre, as a function of wavelength.	9
Fig. 2•2	Power splitting at an interface.	10
Fig. 2•3	Schematic diagram of mid-span OTDR.	11
Fig. 2•4	Energy loss in a fibre element.	12
Fig. 2•5	Geometric optics for scattering.	13
Fig. 2•6	Cascade of amplifiers.	16
Fig. 2•7	Calibration error of A/D conversion.	18
Fig. 2•8	Smoothing of ADC error using input noise.	19
Fig. 2•9	Comparison between conventional and mid-span OTDR.	22
Fig. 2•10	Block diagram of simulated OTDR.	23
Fig. 2•11	Expanded view of the block "Multi-stage Backscatter."	25
Fig. 2•12	Sample simulator outputs: (a) optical power, (b) amplified signal.	26
Fig. 2•13	Backscattering levels at 830 nm and 1310 nm, with equal launched power.	28
Fig. 3•1	Bent fibre: (a) 3-D view, (b) an elemental section.	31
Fig. 3•2	Experimental set-up for leakage measurements.	33
Fig. 3•3	Bend leakage versus bending radius for various bend angles.	34
Fig. 3•4	Apparatus for measuring leakage intensity distribution.	34
Fig. 3•5	Leakage pattern from a 30-degree bend with a radius of 1.5 mm.	35
Fig. 3•6	Optical window of Northern Telecom's Identifiber.	36
Fig. 3•7	Modified Identifiber window for measuring output distribution.	37
Fig. 3•8	Two schemes of modification on Identifiber window.	38
Fig. 3•9	Coordinates for ray matrix.	39
Fig. 3•10	Cascade of optical components.	39
Fig. 3•11	Rays in a GRIN lens and nomenclature.	40
Fig. 3•12	Two schemes for using GRIN lenses with identifiber window.	41

Fig. 3•13	Comparison of different GRIN lens configurations.	42
Fig. 3•14	Coupling function of modified identifiber window.	43
Fig. 3•15	Arrangement for local injection experiment.	47
Fig. 3•16	Locally launched power and fibre bend-lens/laser misalignment.	47
Fig. 4•1	Noise's dependence on detector capacitance, C_D.	49
Fig. 4•2	Schematic diagram (simplified) of the receiver.	52
Fig. 4•3	Miller's Theorem.	54
Fig. 4•4	Bootstrapping: (a) passive, (b) active.	54
Fig. 4•5	General feedback schematic and frequency response.	55
Fig. 4•6	A common realisation of a transimpedance amplifier.	56
Fig. 4•7	High frequency BJT model.	56
Fig. 4•8	Passive equalisation.	59
Fig. 4•9	Final design of the mid-span OTDR receiver.	60
Fig. 4•10	Method for measuring transimpedance with a network analyser.	62
Fig. 4•11	Frequency response of 50-MHz pre-amplifier.	63
Fig. 4•12	Replacement gain channel for MC1733.	65
Fig. 5•1	Predicted head-launch mid-span OTDR output with currently achievable bend tap and receiver performance figures.	70
Fig. 5•2	Predicted local-launch mid-span OTDR performance.	71

List of Symbols

Symbol[*]	*Description*	*Page*[†]
$A(\omega)$	open-loop transfer function of an amplifier	54
$A(x,y)$	admittance function of a measuring device	37
α_b[‡]	bending attenuation constant, infinite cladding layer	31
α_{bc}	bending attenuation constant of a coated fibre	31
α_i	intrinsic attenuation constant	8
α_R	attenuation constant if only Rayleigh scattering loss is present	12
β	propagation constant of wave in a fibre	31
B_a	amplifier -3dB bandwidth	17
β_f	feedback ratio, fraction of output that is fed back	54
B_n	equivalent noise bandwidth	17
C_D	photo-detector dynamic capacitance	52
C_μ	collector-base junction capacitance of a bipolar junction transistor	56
C_π	capacitance corresponding to the emitter-base transit time in a bipolar junction transistor	56
c_R	capture ratio for Rayleigh scattering in a fibre	13
c_t	output coupling of the bend tap	15
Δ	differential refractive index variation (between core and cladding)	13
$E(z,t)$	energy density of a probe pulse	12
E_R	energy returned to the test site	12
η_C	coupling efficiency between fibre bend and detector	15
F	noise factor (of electronic components)	16
f_T	transistor transition frequency, unity current gain-bandwidth	59
f_t	fraction of power tapped out per pass through a bend tap	15
g_m	transistor transconductance	56

[*] Symbols are listed in alphabetical order. Transliteration for greek letters are used.
[†] Page is the page on which the variable first appears or is given a definition.
[‡] Variables in lower case, when specified in decibels, are written in upper case while the subscripts remain the same. Exceptions include upper case symbol which has been listed in here, e.g. V_q and v_q.

$H_E(\omega)$	electronic equaliser transfer function	58
$h_R(t)$	impulse response of fibre backscattering (including Rayleigh scattering, Fresnel reflection and discrete transmission losses).	23
$h_{Ri}(t)$	"ideal" impulse response of fibre backscattering (including only Rayleigh scattering) for a piece of infinitely long fibre	13
$<i_E^2>$	mean-square equivalent input noise contributed by equaliser	58
$<i_n^2>$	mean-square noise current, general	17
k	wavenumber, magnitude of wavevector	31
k_B	Boltzmann's constant (1.38×10^{-23} J/K)	15
L	length of fibre between test point and point under observation	11
L_t	length of fibre between test point and transmitter	11
$\boldsymbol{M}$	ray matrix, subscripts identify the type of optical component	39
m_a	number of sample measurements taken for averaging	19
m_c	number of pulses in a correlation code sequence	19
NF	noise figure (of electronic components)	16
n_1	(real) refractive index of fibre core	10
n_2	(real) refractive index of fibre cladding	10
n_3	(real) refractive index of fibre coating	31
n_{eff}	effective refractive index of a piece of fibre under stress	30
nep	noise equivalent power	17
Ω_{region}	solid angle of a region	15
p_i	incident power	10
p_{in}	injected power	8
p_{out}	power output	8
p_r	returned power	10,20
p_{sh}	shot noise power	15
p_t	transmitted power	10
p_{th}	thermal noise power	15
q	electronic charge (1.6×10^{-19} Coulomb)	15
$\mathcal{R}_0$	photo-detector responsivity	17
r_b	effective radius of a bend	30
r_0	critical radius of a bend	33
$\boldsymbol{r}$	ray trajectory	39
snr	signal-to-noise ratio	15

T	absolute temperature	15
t	time (return time of probe signal)	13
θ_D	divergence angle of the fundamental mode in a fibre	14
θ_C	critical angle at the interface between core and cladding in a fibre	13
V_{err}	calibration error of an analogue-to-digital converter	17
$<v_n^2>$	mean-square noise voltage, general	18
V_q	voltage quantisation step in an analogue-to-digital converter	18
$<v_q^2>$	mean-square quantisation noise voltage	17
v_g	group velocity of light in a fibre's core	13
$w(x)$	beam width parameter	32
w_0	waist (minimum spot size) of a Gaussian beam	14
ω	angular frequency	54
ξ	correction factors for anisotropy in c_R in large core fibres	13
ξ_S	correction factor for anisotropy in c_R in single-mode fibres	14
ζ	equalisation ratio, pole-zero ratio of an equaliser	58
$\Im$	discrete loss profile of a piece of non-ideal fibre	22
$\Re$	discrete reflection profile of a piece of non-ideal fibre	23

CHAPTER 1 Introduction

Advances in the manufacture of optical fibres and related electronic technologies have made possible routine deployment of telecommunication fibres and eventual replacement of existing copper-based systems for many communications applications [1,2]. While new testing techniques for the new medium are being developed, some testing methods for copper cables have been carried over to the new regime. Among them, the reflectometer was given a new implementation in the optical domain.

Although modern optical reflectometers are reliable and accurate, some aspects still have room for improvements. This thesis will describe studies conducted on **mid-span optical time-domain reflectometry** which could augment conventional implementations by circumventing some of their inconveniences.

1.1 The Need for Optical Reflectometry

Fibre intrinsic attenuation, extrinsic attenuation (from splices, connectors, etc.) and faults are the characteristics most frequently required to be identified. All these, except faults, can be obtained by transmission tests but the required access to both fibre ends is impractical. Optical cables run in continuous stretches measured in kilometres, usually buried at depths up to two meters.

From measurements at one end of a fibre, a reflectometer gives reflection and scattering levels as a function of distance. There are two general types of reflectometers. Optical Frequency-Domain Reflectometry (OFDR) can measure the fibre's optical characteristics by sweeping through a range of optical wave-

lengths (i.e. controlling the *electric field* at ~10^{14} Hz). Optical Time-Domain Reflectometry (OTDR) modulates the *intensity* of a *single* optical wavelength (at ~10^{7} Hz). There is a hybrid, Frequency-Domain Optical Reflectometry (FDOR) [3]. It modulates the intensity like OTDR but sweeps the modulation's frequency the way OFDR sweeps the optical frequency. Instead of controlling the *electric field* at ~10^{14} Hz, it controls the *intensity* at ~10^{7} Hz. In general, OTDR's simpler electronic requirements give it wider popularity[1]. One needs only electronics in the HF/ VHF regime (10^{6} - 10^{8} Hz).

1.2 Optical Time-Domain Reflectometry

Optical time-domain reflectometry (OTDR) was first demonstrated by Barnoski *et al.* in 1976 [4] as a means of characterising optical fibres. The first theoretical effort came from Personick in 1977 [5]. The general configuration of their systems is shown in Figure 1·1. The principle of this method remained the same, though many variants exist.

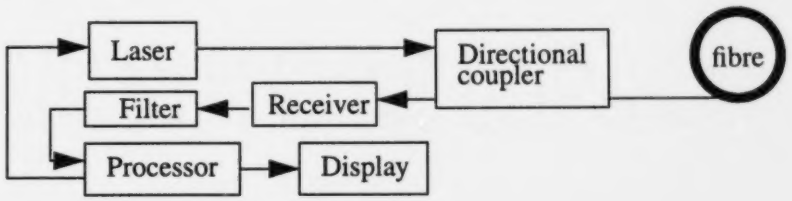

Fig. 1•1 General configuration of an optical time-domain reflectometer. [6]

An OTDR set interrogates a fibre with an optical pulse. Minute non-uniformities in the fibre scatter some of the pulse's energy as it traverses the length of the fibre. In a modern fibre, scattering is responsible for most of the intrinsic attenuation of light at frequencies higher than 300 THz. **Rayleigh scattering** is

1. This scenario is bound to change because of the development of integrated optics and the ever wider availability of high-frequency analogue ICs. In fact, frequency domain optical network analysers are currently available commercially, such as the HP8703A by Hewlett Packard.

predominant among the scattering mechanisms. It is the scattering caused by irregularities smaller than the wavelength of the incident light. Some of the scattered light is captured by the fibre and is guided *backward*, travelling toward the source. An OTDR set searches for and analyses this portion of the scattered light. This "backscattering" contains information on all the fibre's features, both distributed (such as attenuation characteristics) or localised (discontinuities).

1.3 Modern OTDR

The figures of merit of an OTDR are its **maximum spatial resolution** and its **dynamic range**. The maximum spatial resolution[2] is the minimum distance between two discontinuities (or 'events') the OTDR set can distinguish. It is determined by the system bandwidth which is in turn related to, or limited by:

1. the length of the probe pulse,
2. the receiver bandwidth,
3. the rise and fall times of the probe pulses,
4. the signal processing speed and
5. the receiver saturation characteristics.

In general, a finer resolution requires shorter pulses, larger bandwidth and a faster signal processor.

The dynamic range is the maximum power attenuation the probing signal can suffer before it disappears into the noise of the system. Together with the attenuation and scattering/reflection levels of the fibre, the dynamic range determines the maximum test range of the OTDR set. Significant gains in both figures of merit can be obtained by the application of noise-reducing signal processing techniques.

2. All modern OTDR equipment let the user choose the spatial resolution because spatial resolution is often traded for a longer measurement distance or a shorter measurement time. Only the *maximum* spatial resolution can be used as a figure of merit.

Modern OTDR sets usually have maximum spatial resolutions in the order of ten meters and dynamic ranges upwards of $27dB_{optical}$ which corresponds to test ranges of better than 100 km for non-reflective faults (such as splices and good connectors)[3]. Averaging (over repeated measurements), although time-consuming, is simple to implement, and is now *de rigueur*. Correlation OTDR was developed as a time saving alternative to straight averaging [7-10]. Using orthogonal coded sequences, a correlating OTDR set can send multiple probe pulses without confusion, whereas a conventional OTDR set must wait until a pulse has reached a pre-determined range before sending the next pulse. The time saving could be phenomenal. For instance, an OTDR set using 64-bit sequences can complete in one minute what would take a conventional OTDR set well over an hour [10]. Figure 1·2 graphically shows the difference.

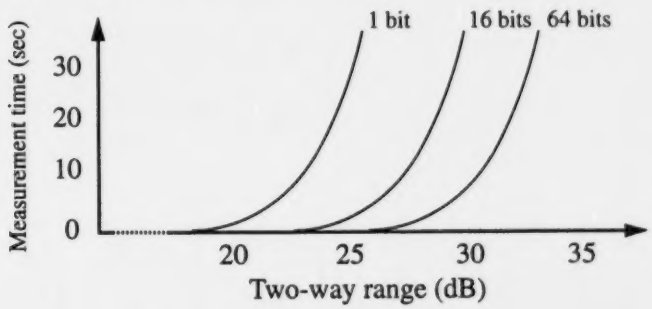

Fig. 1•2 Time needed to measure 0.1-dB faults versus two-way range, for different sequence lengths in a correlating OTDR, after [11].

3. Specifications of HP8145A (HP Test & Measurement Catalogue, 1990) claim an 8-m resolution and a 28-dB dynamic range. Specifications of HP8146A (HP Test & Measurement Catalogue, 1992) claim distance accuracy of 0.5m + sample spacing + measurement distance x 10^{-4} and a 30-dB dynamic range.

1.4 Inconveniences in Using OTDR

A break of an optical cable is a typical case for the use of OTDR. The maintenance personnel at the telephone office would transfer the fibre to an OTDR set and locate the break by measuring the fibre length from the test point to the break. However, this length has no fixed relation to the surface distance from the test site to the break because the fibres in a cable are loosely wound around a core and the cable itself does not run in a straight line. Most OTDR sets need a fibre/cable ratio for correction. Often, close-by landmarks such as known splices are identified from the measurement and a road crew is sent to search for the fault. In most cases, it involves looking for a construction crew, a backhoe or the like. The search for out-of-sight breaks would be very time-consuming. Measurements could be performed again at a point near the break but breaking the fibre to create the required end is undesirable.

Even if a good fibre end is available, reflection from the connection between instrument and fibre can saturate the receiver for a period of time corresponding to a testing distance of up to half a kilometre. No information about the fibre can be obtained in this so-called **dead zone**. Should the dead zone be of interest, a spool of fibre is fusion-spliced on as a buffer. Measurements from the extra length is gated out. Various methods had been used to eliminate the dead zone [4, 5 & 13]. None offered convenience. The best one can do is to use angled-facet connectors and/or trade spatial resolution for Rayleigh scattering strength[4]. We will dwell more on this relation in the next chapter.

4. At a spatial resolution of approximately 10 m, the maximum Rayleigh scattering strength is 60 dB below launched power. The best connector available, with angled contacts (FC/APC) has a guaranteed return loss of 60 dB, typically 63 dB when in use.

1.5 Local Detection through Bending

Some of these inconveniences could be overcome if the OTDR design does not require a fibre end for coupling. Guided light in an optical fibre can be tapped through a bend. When entering a region with changing geometry, some guided modes become leaky modes. Previous work, both theoretical and experimental, has shown that there are well defined relations between bend geometry and leakage patterns [14-18] (this is only a representative list of papers; limited space prevents a comprehensive listing).

Much effort has gone into the search for repeatable methods of local detection; commercial products are currently available. Although these products are fairly efficient in collecting the leakage from a fibre bend, they are adapted only for low-frequency operations[5]. An OTDR affording high spatial resolution needs a bandwidth in the HF range.

If an OTDR set is equipped with a bend tap, it can perform measurements in mid-span to supplement tests done at the head end, without breaking the fibre. Although high resolution is available in conventional OTDR sets, it is more meaningful in local tests than in remote ones. In mid-span, the test set might use the signal provided by the head-end transmitter or it might inject its own signal. Both options have significant difficulties. The former cannot be used with correlation codes without full clock recovery. The latter is limited by the notoriously ineffective injection techniques currently available.

5. One exception, with a 2-MHz bandwidth, is to be found in Reference 19.

1.6 The Objectives of this Thesis

This thesis is a feasibility study on realising a mid-span optical time-domain reflectometer with established techniques and with as many commercially available components as possible. We seek to identify areas which need and deserve further investigations. The major goal is to adapt the local detection techniques for HF/VHF operations. We will also study the feasibility of local launching. Design repeatability (or manufacturablilty) will be of concern.

1.7 The Organisation of this Thesis

In Chapter 2 a system level survey will identify the effects of local detection on the figures of merit and how these figures should be interpreted in the context of mid-span OTDR. A target system will be described.

Chapter 3 will present the optical aspects of this project. It will describe the relation between bending geometry and leakage, results of bending experiments and a bend tap design. In addition, we will survey local launching techniques.

Chapter 4 will document studies on the electronic requirements of local detection at high electrical frequency: photoreceivers which are tolerant to the idiosyncratic optoelectronic requirements of bend taps.

The last chapter will return to the general OTDR equation developed in Chapter 2 with figures gathered from studies described in Chapters 3 and 4. It will discuss the head-launched local-detected OTDR and the current standing of local launch. A survey of emerging, potentially useful technologies will conclude this thesis.

CHAPTER 2

Theories of Optical Time-Domain Reflectometry

In this chapter we will summarise the relevant parameters of an OTDR system and their effects on system performance. We will introduce parameters associated with local-detection and reinterpret the dynamic range. After developing the system equation and power budget, we will describe our targets.

2.1 Relevant Properties of Optical Fibres

For OTDR operations, the most important properties of a piece of fibre are attenuation and reflection. (For convenience, we use "backscattering" synonymously with the portion of Rayleigh scattered light that is sent backward.)

2.1.1 Attenuation

The minimum attenuation in silica-based optical fibres is set by Rayleigh scattering and infrared absorption. The combined attenuation minimum is near 1.55 μm. From this point, absorption increases with wavelength and Rayleigh scattering increases with decreasing wavelength (Figure 2·1). The large attenuation around 1.4 μm is due to the absorption by OH^- ions.

The intrinsic attenuation is related to the length of the fibre. In terms of optical power,

$$p_{out} = p_{in} \cdot e^{-\alpha_i L}, \qquad \text{(Eq. 2•1)}$$

or, in logarithmic terms:

$$P_{out} - P_{in} = -A_i L, \qquad \text{(Eq. 2•2)}$$

where α_i and A_i are the intrinsic attenuation constant, specified in nepers per kilometre and decibels per kilometre, respectively. L is the fibre length and p denotes power (when a quantity is specified in decibels, it is changed to upper case). The two forms of the attenuation constant are related by:

$$A_i Ln\,(10) = 10\alpha_i. \qquad \text{(Eq. 2•3)}$$

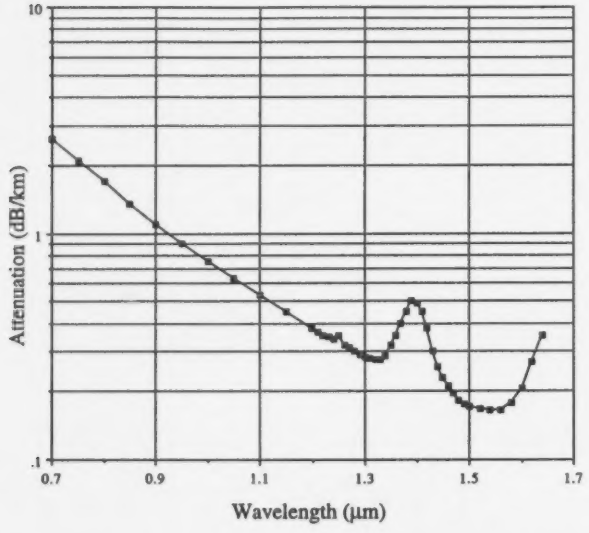

Fig. 2•1 Intrinsic attenuation of silica-based fibre, as a function of wavelength, after [12].

Connectors and splices have varying losses, depending on core offset, misalignment and separation between fibre ends (in connectors). Loss increases with offset and misalignment in either splices or connectors. The dependence of connector loss on fibre end separation is more complicated because of multiple reflection. It becomes an etalon type of problem. The amount of leakage due to bending depends on the radius of the bend and the fibre type. It has a exponential dependence on bending radius [12]. Given a fixed fibre core diameter, electro-magnetic waves of longer wavelengths penetrates the cladding further than

waves of shorter wavelengths. Therefore waves of longer wavelengths are more prone to loss in a bend, given the same bend shape. Hence they are better suited for local detection since tapping can be done with milder bends (larger bending radii), which induce less stress in the fibre.

2.1.2 Fresnel Reflection

Fresnel reflection occurs at the boundary of two media of different refractive indices. In the context of OTDR, the name means only the portion of the reflection that is captured and guided backward by the fibre. The angle between the fibre axis and the interface, the refractive index of the outside medium and the surface roughness of the interface determine the strength of the reflection.

For a perfectly smooth end face perpendicular to the fibre axis (normal incidence), the reflectance is given by:

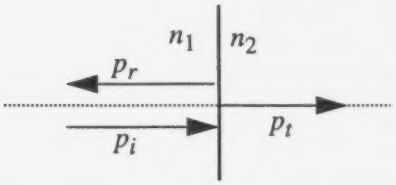

$$\frac{p_r}{p_i} = \left(\frac{n_2 - n_1}{n_1 + n_2}\right)^2. \qquad \text{(Eq. 2•4)}$$

Fig. 2•2 Power splitting at an interface.

where and p_i, p_r and p_t are the powers of the incident, reflected and transmitted waves, respectively. For a single perfect glass-to-air interface the reflectance is approximately 0.04, or -14dB. Although this is the maximum Fresnel reflection, in a fibre break, reflection from the other end face can increase the total Fresnel reflection. On the other hand, the reflectance of the fault can be much lower. Given the wide possible range of Fresnel reflection strength, OTDR designs anticipate, but do not rely on, Fresnel reflection.

2.1.3 Rayleigh Scattering

Rayleigh scattering is the scattering of electromagnetic waves by irregularities in an otherwise uniform, homogeneous medium. When a fibre is manufactured (drawn), microscopic non-uniformities are formed in the core. Being smaller than the wavelength of the propagating light, these imperfections behave like sets of induced multipoles, radiating energy from the incident electromagnetic wave. The strength of Rayleigh scattered light depends on the wave number (raised to the 4^{th} order) and the fibre's properties. Rayleigh scattering is the primary mechanism on which OTDR relies.

2.2 Equations of OTDR

The various factors affecting the performance of an OTDR set may be summarised in a range equation. We will derive the range equation for mid-span OTDR. Probe pulses are launched into the head end (head-launch). Local-launch (probe pulses launched locally) will be considered as a special case. A linear receiver and a digital signal processor are assumed. Discussion in this section will include the impulse response of fibre backscattering, receiver and signal processor noises and the effects of their characteristics on system performance.

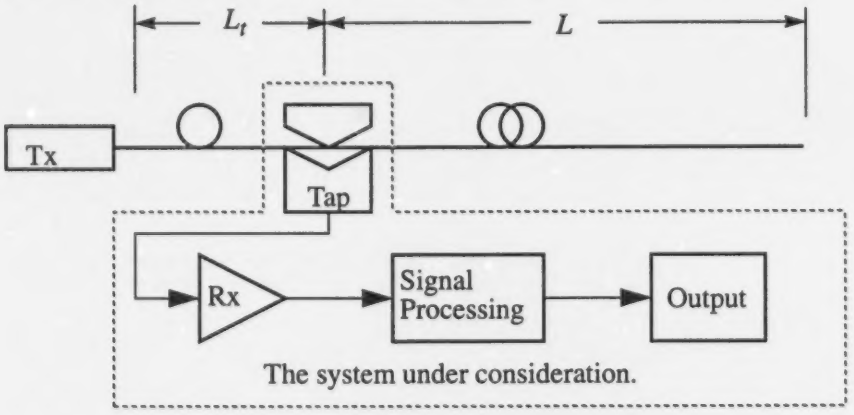

Fig. 2•3 Schematic diagram of mid-span OTDR.

2.2.1 The impulse response of fibre backscattering

We first seek a basic backscattering impulse response, $h_{Ri}(t)$, of a piece of fibre with no discontinuities such that the back-propagating power at zero position, $z = 0$, is given by convolving $h_{Ri}(t)$ with the launched power. In essence, we seek to reduce the backscattering to a linear system like a filter.

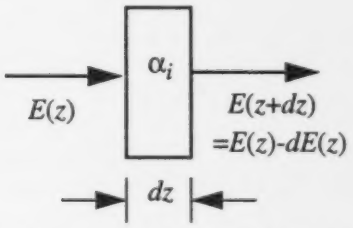

Fig. 2·4 Energy loss in a fibre element.

Analogous to Eq. 2·1, the energy (per unit length) of an impulse travelling in a piece of uniform fibre is described by:

$$E(z,t) = E_0 \delta(z - v_g t)\, e^{-\alpha_i z} \qquad \textbf{(Eq. 2•5)}$$

where E_0 is the total energy and v_g is the group velocity of the pulse. Referring to Figure 2·4, the energy not transmitted through dz is:

$$\begin{aligned} dE(z) &= E_0 \delta(z - v_g t)\, e^{-\alpha_i z}\left(1 - e^{-\alpha_i dz}\right) \\ &= E_0 \delta(z - v_g t)\, \alpha_i e^{-\alpha_i z} dz \end{aligned} \qquad \textbf{(Eq. 2•6)}$$

We have used a first order approximation for $\left(1 - e^{-\alpha_i dz}\right)$ because $\alpha_i dz \ll 1$. To separate the scattering loss from the total intrinsic loss, we need to introduce the ratio between their attenuation constants, α_R/α_i. A **capture ratio**, c_R, is required to account for the fact that only a portion of the scattered light is captured by the fibre. This portion of light is then subject to further attenuation travelling back, $e^{-\alpha_i z}$. Combining these factors with Eq. 2·6 gives the energy scattered at position z and detected at $z = 0$:

$$dE_R = E_0 \delta(z - v_g t)\, \alpha_R c_R e^{-2\alpha_i z} dz. \qquad \textbf{(Eq. 2•7)}$$

The energy detected at $z = 0$ from a fibre of length L is

$$E_R = \int_0^L dE_R(z) = \frac{1}{2} E_0 c_R \frac{\alpha_R}{\alpha_i} \left(1 - e^{-2\alpha_i L}\right). \qquad \text{(Eq. 2•8)}$$

This equation holds for $z = v_g t$, a condition imposed by the δ-function. The time it takes to reach and return from a distance L is $L/2v_g$. Substituting this relation into Eq. 2·8 and differentiating with respect to time yields the detected *power*. Normalising the result with respect to energy (dividing by E_0) gives the impulse response we seek,

$$h_{Ri}(t) = \frac{1}{2} c_R \alpha_R v_g e^{-\alpha_i v_g t}. \qquad \text{(Eq. 2•9)}$$

There remains the capture efficiency, c_R, to be defined. As shown below, part of the scattered light is captured by the fibre and is guided backward.

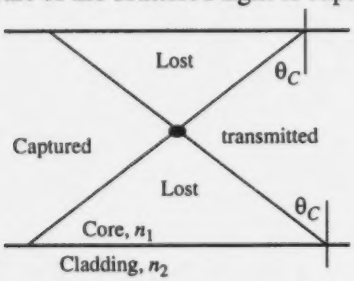

Fig. 2•5 Geometric optics for scattering.

The capture ratio, c_R, can be approximated with geometric optics. If the scattering is isotropic, then c_R equals the solid angle ratio between the "not transmitted" regions (Figure 2·5).

But scattering is not isotropic, so we introduce a correction factor, ξ, to the solid angle ratio[6].

$$c_R \cong \frac{\xi \Omega_{captured}}{\Omega_{lost} + \Omega_{captured}} = \xi \frac{1 - \sin\theta_C}{1 + \sin\theta_C} = \xi \frac{n_1 - n_2}{n_2} = \xi\Delta. \qquad \text{(Eq. 2•10)}$$

6. We are justified to suspect anisotropy in the scattering because the dipole term is usually dominant in a multipole expansion. If one models the scattering site as a non-conductive spherical region behaving like an induced dipole, then the differential scattering cross-section is proportional to $(1+\cos^2\theta)$. See appendix A for details.

We have used the definition of the critical angle, $\sin\theta_C = n_2/n_1$ and the definition of the differential index variation, $\Delta = (n_1 - n_2)/n_2$. The value of ξ is about 0.75 for step-index fibres and 0.5 for parabolic graded-index fibres [22].

The mode field of a wave propagating close to the cladding penetrates the cladding more than that of a wave propagating on the fibre axis. A corollary to this is that the probability of the light's being captured changes less rapidly with radial position in a fibre core of 50 μm diameter than in a core of 9 μm diameter. The geometric optics assumptions made earlier correspond to the limiting case of a very large core diameter. In a fibre core of 9 μm diameter, the value of the correction factor has a strong dependence on fibre geometry and wavelength. Reference 21 re-derived the capture ratio for the fundamental mode in a 9-μm core:

$$c_R = \frac{3}{4}\left(\frac{\lambda}{w_0\pi}\right)^2 \frac{\Delta}{n_1^2 - n_2^2} = \xi_S \Delta \qquad \textbf{(Eq. 2•11)}$$

where a is the radius of the core, w_0 is the minimum spot size of the fundamental mode and ξ_S is the correction factor for a single-mode fibre[7]. In terms of the divergence angle of this mode, $\theta_D = \lambda/(\pi w_0 n_1)$, Eq. 2·11 can be written as:

$$c_R = \frac{3}{8}\theta_D^2. \qquad \textbf{(Eq. 2•12)}$$

θ_D can be obtained by measuring the fibre's output divergence.

The above derivations for the capture ratio, although simplified, provide a basis for further discourse on OTDR's basic mechanism and limitations. One expects reasonable figures from these formulae for later calculations, but not precise numerical results because other factors in the range equation are good approximations at best, as we shall see in the coming sections.

7. There had been an interesting dialogue between the authors of [21] and [22], concerning a factor of 0.5 in Eq. 2·12. See [24].

2.2.2 Receiver characteristics

After a probe pulse is sent, the scattered power (as described in §2.2.1) is detected and amplified by a receiver. Given a fixed source power, the characteristics of this receiver set the performance of an OTDR system. Receiver noise limits the dynamic range. Maximum spatial resolution is set in part by receiver bandwidth. The length of the dead zone is set by the receiver's recovery time after saturation. In a non-intrusive OTDR receiver, the -6 dB coupling efficiency of the direction coupler (Figure 1·1) is replaced by the bend tap coupling factor, c_t:

$$c_t = (1 - f_t) f_t \eta_C, \qquad \text{(Eq. 2•13)}$$

where f_t is the fraction of power lost in each pass through the tap and η_C is the tap's efficiency in coupling the leakage to a detector.

The minimum detectable signal power is set by noise contributions from both transmitter and receiver. Transmitter noise (e.g. relative intensity noise) is relatively weak and is generally ignored[8]. Receiver noise is dominated by thermal noise and shot noise. Their spectral densities are given by, respectively,

$$\frac{d}{df}\langle p_{th} \rangle = 2k_B T, \qquad \text{(Eq. 2•14)}$$

$$\frac{d}{df}\langle p_{sh} \rangle = qIR, \qquad \text{(Eq. 2•15)}$$

where k_B is Boltzmann's constant, T is the absolute temperature of the device, q is the elementary charge, I is the total current and R is the resistance through which the current flows.

The signal-to-noise ratio at the final stage of the OTDR receiver/signal processor is important. Depending on the type of fault, the minimum required snr

8. In fact noise sources which are considered important in transmitters used for communication are not considered important in OTDR transmitters. General purposes transmitters can be used. The usual signal-to-noise ratio (snr) at an OTDR receiver, being close to or even less than unity, hides transmitter flaws very well.

varies. Each of the many stages from the pre-amplifier to the signal processor contributes some noise. But it is well known that noise contribution by an early stage is more significant than that of a later stage.

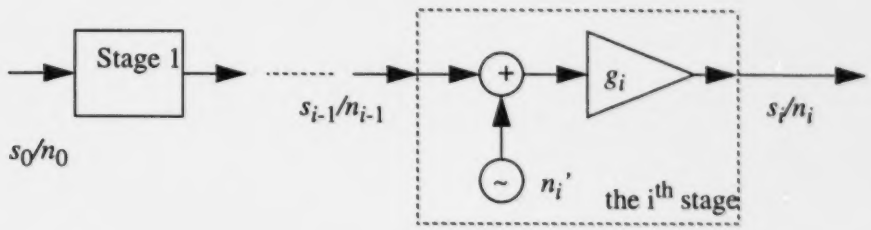

Fig. 2•6 Cascade of amplifiers. Each has a power gain, g, and equivalent input noise, n'.

Referring to Figure 2·6, the output snr of the i^{th} stage is

$$\frac{s_i}{n_i} = \frac{s_0 g_1 g_2 \cdots g_i}{(n_0 + n_1')\, g_1 g_2 \cdots g_i + n_2' g_2 g_3 \cdots g_i + \ldots + n_i' g_i}. \qquad \textbf{(Eq. 2•16)}$$

It is best to use a high-gain, low-noise pre-amplifier so that the signal gain would be matched only by the gain of the first noise term. Other noise terms, not having the gain g_1, are in effect diminished.

Noise performance of electronic amplifiers are commonly specified by noise figures (NF) or noise factor (F) defined as the ratio of output snr to input snr[9]. Eq. 2·16 can be rewritten as

$$\frac{s_i}{n_i} = \frac{s_0}{n_0} \cdot \left(F_1 + \frac{F_2 - 1}{g_1} + \ldots + \frac{F_i - 1}{g_1 g_2 \cdots g_{i-1}} \right)^{-1} = \frac{s_0}{n_0} \frac{1}{F_{sys}}, \qquad \textbf{(Eq. 2•17)}$$

9. Convention has it that noise figure (NF) is noise factor (F) specified in decibels.

which is more useful in selecting electronics components[10]. Here F_{sys} is the noise factor of the whole system. (Note F_1's prominence in the definition.)

Noise is represented in the range equation by a noise equivalent power (nep) which is the optical power needed at the detector to achieve a unity snr. Both noise and spatial resolution increase with system bandwidth; there is always a trade-off between the two. It is common that the input resistance of an amplifier controls both the bandwidth and noise. If the amplifier is thermal noise-limited and has a dominant pole set by its equivalent input resistance and capacitance, R_{in} and C_{in}, the mean square noise current is $(4k_BTB_n)/R_{in}$, where B_n is the noise equivalent bandwidth, a quantity proportional to the amplifier bandwidth: $B_n = \varepsilon B_a$. B_a is the amplifier's signal bandwidth, $B_a = 1/(2\pi R_{in}C_{in})$. The nep is equal to $\langle i_n^2 \rangle^{1/2}/\mathcal{R}_0$, where $\mathcal{R}_0$ is the detector's responsivity in A/W. Combining the four relations above shows that nep is proportional to B_a in this case (in which the same resistive network controls both noise and bandwidth):

$$nep_{therm} = \frac{\sqrt{8\pi k_B T C_{in} B_n B_a}}{R_0} = \frac{\sqrt{8\pi k_B T C_{in} \varepsilon B_a^2}}{R_0} \propto B_a. \qquad \textbf{(Eq. 2•18)}$$

The nep of a shot noise-limited amplfier, on the other hand, is proportional to $\sqrt{B_a}$. In either case, barring improvement in transmitter output power, a higher dynamic range generally means decreased spatial resolution, or vice versa.

Since signal processing is to be done digitally, the analogue signal must be converted to digital form. Analogue-to-digital conversion imposes quantisation noise which comes from the calibration error of the analogue-to-digital converter (ADC). This error is a saw-tooth function, Figure 2·7. The quantisation

10. We are aware that noise figures/factors are functions of the reference source, n_0, as evident in Eq. 2·23. Amplifier data sheets general list NF's or F's with the optimum noise source matching. Comparisons between components were done with careful interpretation of the specifications on noise performance.

noise voltage, $\langle v_q^2 \rangle$, is found by integrating the product of the ADC's calibration error, V_{err}, and the error function (for Gaussian white noise). The integral spans the input voltage range of the ADC can handle, assuming negligible probability of saturation or cut-off.

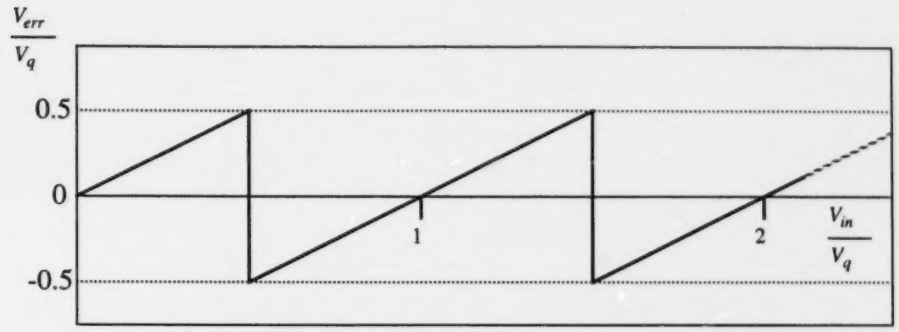

Fig. 2•7 Calibration error of A/D conversion, V_{err} is the error voltage, V_{in} is the input and V_q is the quantisation step.

When the noise voltage, $\langle v_n^2 \rangle$, is small compared to the quantisation step, V_q. The value of $\langle v_q^2 \rangle$ depends on the average input voltage, V_0. In general, $\langle v_q^2 \rangle$ resembles $V_{err}(V_0)$. If the rms input noise spreads over multiple quantisation steps, $\langle v_q^2 \rangle$ approaches the limit of $\langle v_n^2 \rangle / 12$ [25]. This method is limited by the dynamic range of the ADC. If the ADC has 2^m steps and if noise covers 2^n steps, the snr must be below 2^{m-n} to prevent saturation by the signal. This may be too extravagant, especially with high speed ADC's ($\geq 10^8$ samples per second) which are usually 6-bit or 8-bit converters (only 64 and 256 steps, respectively).

Analyses on the relation between noise-to-quantisation step ratio and calibration error (Figure 2·8, after Reference 26) show that there are compromises. If the quantisation step is matched to the input noise voltage, the average calibration error is quite close to zero. In which case, the ultimate noise performance depends on the input noise, which comes from the receiver. Since analogue-to-

digital converters have fixed input ranges, the receiver's gain should be determined by the quantisation step voltage of the ADC.

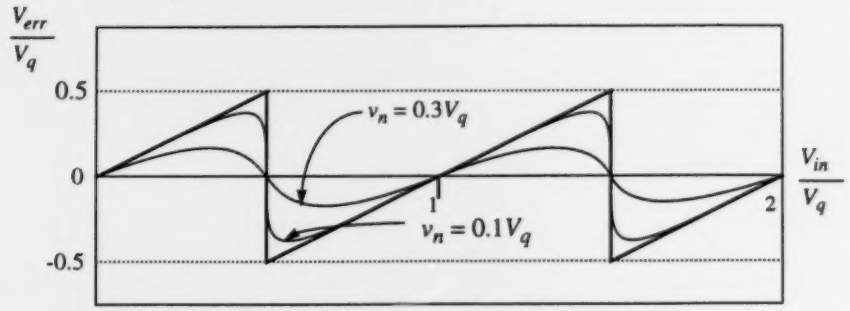

Fig. 2•8 Reduction of ADC error using input noise (v_n is rms input noise).

Quantisation noise presents another barrier between fine resolution and wide dynamic range. That a fast ADC would probably be saturated before the receive somewhat alleviates the dynamic range requirement on the receiver. But it becomes important for the receiver to guard against ADC saturation since it would take the ADC's complex circuit much time to recover. Also the gain of the receiver should be chosen such that the output noise voltage is matched to the ADC's quantisation step voltage to reduce quantisation noise.

2.2.3 Signal processing gains

Despite added complexity and risk of saturation (of the ADC), signal processing can reduce noise and extend the dynamic range. The most common form of signal processing is averaging. Recently, correlation techniques with coded sequences were developed. Sequences instead of single pulses are sent so the average power of the probing signal is increased. Correlation provides correct timing; one can "distinguish" one pulse from another.

A sequence of m_c bits, repeated m_a times for averaging, has $m_a m_c$ times the energy of a single pulse. The total mean square noise current is also $m_a m_c$

times. But the noise equivalent power is proportional to the *root* mean square noise current, and is therefore increased to a lesser extent, as follows:

$$nep_{eff} = (nep) / (\sqrt{m_a m_c}) . \qquad \textbf{(Eq. 2•19)}$$

This equation will be used to calculate the effect of signal processing on the final effective signal-to-noise ratio.

2.2.4 The range equation (OTDR maker's formula)

The factors discussed in this chapter can be combined to give the range equation, the well known **OTDR maker's formula**. We will present a summary of its derivation. The received backscattered power, p_r, from an infinitely long fibre, with a bend tap located at a distance L_t downstream from the source (Figure 2·3), probed with a pulse of p_{in} watts, of duration of τ_p second, is given by the convolution

$$p_r = p_{in} e^{-\alpha_i L_t} c_t [\, (u(t) - u(t-\tau_p)) \otimes h_{Ri}(t) \,] . \qquad \textbf{(Eq. 2•20)}$$

where $h_{Ri}(t)$ is the fibre impulse response (Eq. 2·9) and $u(t)$ is the unit step function. The convolution integral, in explicit form, is:

$$\begin{cases} \left(\dfrac{\alpha_R}{2\alpha_i} c_R\right)\left(1 - e^{-\alpha_i v_g t}\right), & (0 \le t \le \tau_p) \\ \dfrac{\alpha_R}{2\alpha_i} c_R \left(1 - e^{-\alpha_i v_g \tau_p}\right) e^{-\alpha_i v_g (t-\tau_p)}, & (\tau_p \le t < \infty) \end{cases} \qquad \textbf{(Eq. 2•21)}$$

Typical values of the product $\alpha_i v_g$ are 18000 sec^{-1} at λ = 1300 nm and 90,000 sec^{-1} at λ = 830 nm. For pulses shorter than 10 µs (spatial resolution finer than 1 km), $e^{\alpha_i v_g \tau_p} \approx 1 + \alpha_i v_g \tau_p$. For $t \ge \tau_p$, Eqs. 2·20 and 2·21 combine to give

$$p_r = \frac{1}{2} p_{in} e^{-\alpha_i L_t} c_t c_R \alpha_R v_g \tau_p e^{-\alpha_i v_g t}, \ (\tau_p \le t) . \qquad \textbf{(Eq. 2•22)}$$

The measurement range, L, of an OTDR is the distance between the receiver and the furthest point from which backscattered power is just discernible at the receiver (i.e. a certain minimum optical signal level is reached). This distance, L, is reached when $t = 2L / v_g$, at which time $p_r = nep_{eff} \cdot snr_{min}$. These relations are substituted into Eq. 2·22 to solve for the range, L. The resultant **range equation**, cast in decibels, is the **OTDR maker's formula**.

$$L = \frac{1}{2A_i}\left\{P_{in} + C_t + C_R + A_R - 10\log\left(\frac{1}{v_g \tau_p}\right) - NEP_{eff} - SNR_{min}\right\} - \frac{L_t}{2} \quad \textbf{(Eq. 2•23)}$$

where SNR_{min} is the required minimum signal-to-noise ratio at the detector. The ***one-way*** **dynamic range**, ${}^1DR$, is the term in braces in Eq. 2·23:

$${}^1DR = \left\{P_{in} + C_t + C_R + A_R - 10\log\left(\frac{1}{v_g \tau_p}\right) - NEP_{eff} - SNR_{min}\right\}. \quad \textbf{(Eq. 2•24)}$$

OTDR sets are usually specified by a *two-way* dynamic range (1/2 of one-way) for non-reflective breaks at unity *snr*. To obtain the measurement range of a conventional OTDR, a user divides the two-way dynamic range by the fibre's attenuation constant. The two-way dynamic range is practically synonymous with measurement range and is used as the primary figure of merit.

In mid-span OTDR, only the one-way dynamic range is a figure of merit. The two-way dynamic range and the corresponding two-way distance cause confusion (see Figure 2·9). If the "local" range (range 2) is used as a figure of merit, mid-span OTDR is worse than conventional OTDR. But if the "absolute range" (range 1) is used, then mid-span OTDR is an improvement over conventional OTDR. From this figure, one can also comprehend the potential of mid-span OTDR; the extension of the "absolute" range makes more of the fibre accessible.

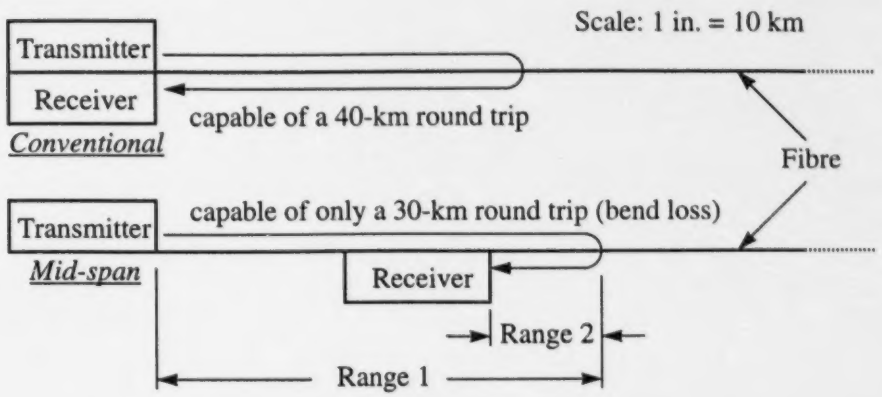

Fig. 2•9 Comparison between conventional and mid-span OTDR.

2.3 A Simulated OTDR

It became apparent in previous sections that many compromises must be made in defining a target system. We simulated an OTDR system according to the OTDR maker's formula in order to understand quantitatively the relationships between the many parameters and to help achieve the best compromises among conflicting performance demands.

2.3.1 From ideal fibre response to practical fibre response

Localised transmission losses and reflections can be included in the backscattering by adding two variables to Eq. 2·9. For m_d discontinuities, we define

$$\Im = \prod_{i=1}^{m_d} \left\{ u(t) - (1 - T_i^2)\, u(t - \tau_i) \right\}, \qquad \textbf{(Eq. 2•25)}$$

where T_i is transmittance of the i^{th} discontinuity, τ_i is the return time to the i^{th} discontinuity. It is also necessary to define

$$\Re = \sum_{i=1}^{m_d} \frac{R_i}{T_i^2} \delta(t - \tau_i), \qquad \text{(Eq. 2•26)}$$

where R_i is the reflectance of the i^{th} discontinuity. We have ignored multiple reflection since they are generally weak. The modified impulse response is

$$h_R(t) = \Im\left(\frac{1}{2} c_R \alpha_R v_g \tau_p + \Re\right) e^{-\alpha_i v_g t}, \ (\tau_p \le t). \qquad \text{(Eq. 2•27)}$$

Eq. 2·25 imposes power drops due to lossy discontinuities. It may be viewed as the normalised energy of a pulse which starts at unity with $t = 0$ and decreases by a factor of T_i^2 on reaching a discontinuity at $t = \tau_i$. Eq. 2·26, on convolving with the probe pulse, replicates the pulse at $t = \tau_i$ and alters its amplitude with the i^{th} reflectance. We have assumed that reflection occurs *before* transmission loss so T_i^2 is put in Eq. 2·26 to counter the same term supplied by $\Im$ in Eq. 2·27.

2.3.2 The simulation system

The Block Oriented Systems Simulator (BOSS) was used to simulated the mid-span OTDR. Figure 2·10 shows the overall system. The subsystems "Pulse Generator" and "Multi-segment Backscatter" will be explained in detail. See Appendix B for details of subsystems not shown in this subsection.

Time constraints prevent actual averaging over repeated runs; the effect of averaging is simulated according to Eq. 2·19. In practice, ADC non-linearity becomes apparent with deep averaging (>10^7 samples). Our simulator cannot account for non-linearity so we assumed modest averaging (10^4 to 10^5 samples).

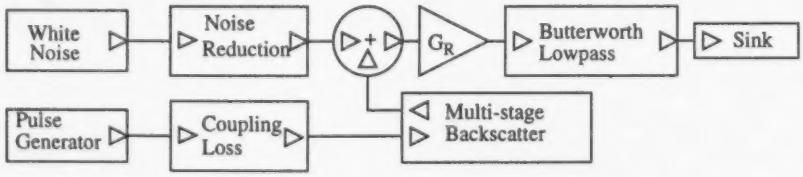

Fig. 2•10 Block diagram of simulated OTDR.

The block "Coupling Loss" accounts for the downlead loss between the source and the tap, laser-fibre coupling and fibre-detector coupling. The gain stage to the right of the adder acts as the optoelectronic conversion and the gain of the receiver. A second order Butterworth low-pass filter is used to set the bandwidth of the receiver. The choice of a Butterworth was motivated by its maximal gain flatness, a minimum attribute for which we aimed when designing the receiver.

2.3.2.1 Pulse generator

This block was used to study the effects of generator bandwidth and pulse shape on the returned signal.

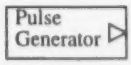

A perfect square pulse is generated by subtracting a delayed unit-step function from a unit-step. The delay is "exported" to the system level so that the pulse length could be altered before each simulation. This square pulse is then passed through a second order low-pass filter whose bandwidth is also exported. The shape of this electrical pulse is altered by the filter type. A Bessel filter, a Butterworth filter and a Chebychev filter were implemented in turn, giving varying degrees of overshoot and rise/fall times. The light-current curve of a semiconductor laser diode is approximated by a third-level subsystem called "Laser" (see appendix B).

2.3.2.2 Multi-stage Backscatter

This block simulates the backscattering response of a piece of fibre with a number of discontinuities.

The basic fibre response (Eq. 2·9) has the form of a first order low-pass filter and is implemented as such. Eq. 2·25 can be reformulated as a series of delayed unit-step functions, subtracted from a unit-step. Although less elegant, it is more intuitive and is simpler to implement in a simulator. Delay-and-subtract loops are added to simulate transmission losses. A series of impulses are added to represent discrete reflections described by Eq. 2·26. Figure 2·11 shows the

construction of a 3-fault fibre link. The section A-A' can be repeated to create more sections of fibre, each bound by two discontinuities. This simulator is used to determine the best compromises between spatial resolution, dynamic range and noise performance.

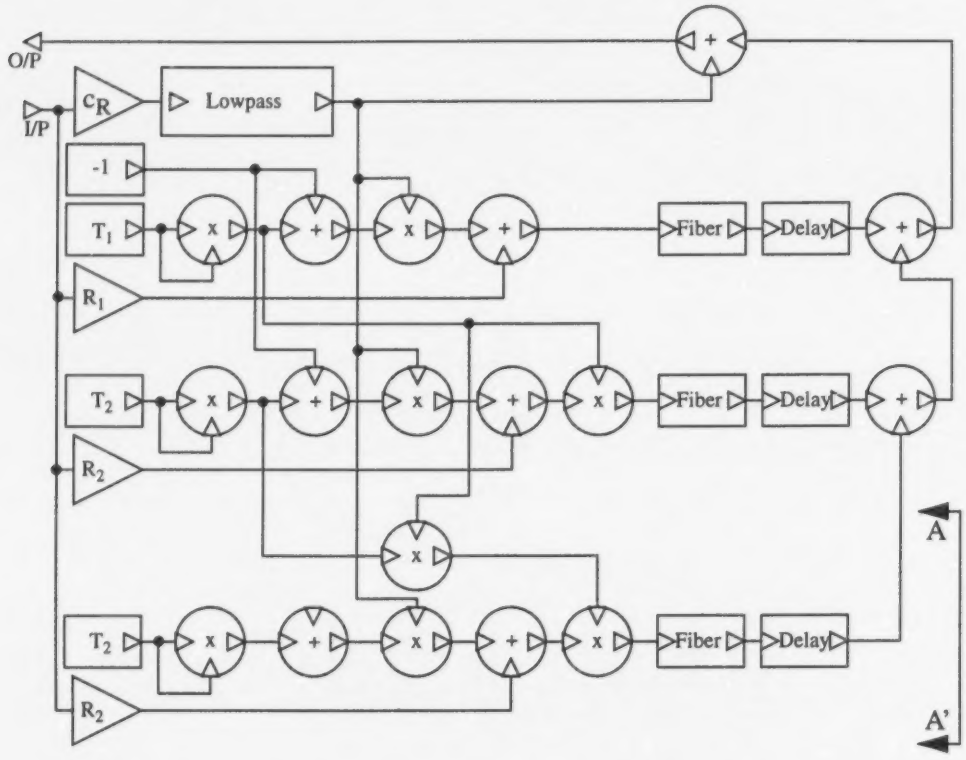

Fig. 2•11 Expanded view of the block "Multi-stage Backscatter."

2.3.2.3 Simulation results

Representative outputs from the simulator are shown in Figure 2·12, showing a half-kilometre span of fibre with one reflective discontinuity followed by a non-reflective one and then a clean break. Operations at $\lambda = 830$ nm with $\tau_p = 100$ ns was assumed. The 10-mW source was located 2 km upstream from the tap. Tapping ratio and coupling efficiency were set to 0.5 and 50% respectively.

The amplifier noise was set at 1 pA / $Hz^{1/2}$. Noise reduction was provided by 10^4-sample averaging.

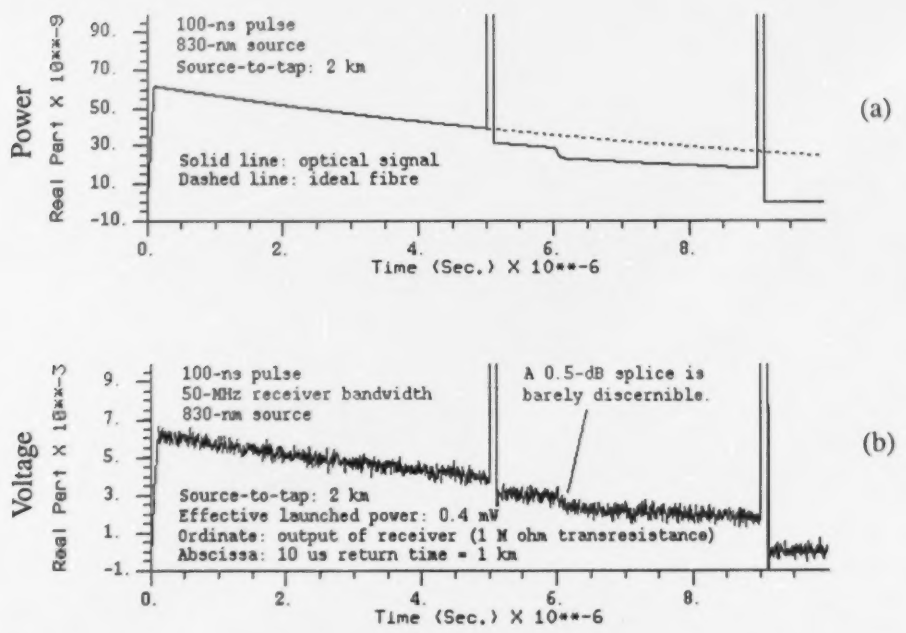

Fig. 2•12 Sample simulator outputs: (a) optical power, (b) amplified signal.

Figure 2·12(b) is the voltage output of the receiver which has a 1-MΩ transimpedance and a 50-MHz bandwidth. The first event (response to a discontinuity) results from a 0.01% reflectance. The slight drop at $t = 6$ μs is the result of a 90% transmittance (-0.5 dB). With $\lambda = 1300$nm, all else remained the same, the initial response was about a factor of 3 lower and the slope was much gentler.

The backscattering does not attain the new Rayleigh scattering level immediately after an event but takes a time equal to the pulse's duration plus time for roll-off (a rounded corner due to rise and fall times of the probe pulse). During this time, an event could be hidden in a stronger, close-by one. The spatial resolution is defined as the minimum distance between two *distinguishable* events. In theory, the maximum spatial resolution is $0.5 v_g \tau_p$. In practice the fall

time of the event is lengthened by the roll-off due to finite amplifier bandwidth, $B_a < \infty$. The generator's bandwidth contributes to the response's roll-off time. Over- and under-shoot of the probe pulse were found to be non-critical; they are often hidden in the noise or saturation. From simulations, we found that if $\tau_p B_a = 1$, the spatial resolution is about $0.75 v_g \tau_p$.

An effective launched power of 0.5 mW at $\lambda = 1300$ nm, a tap coupling factor of 0.1, 10^5-sample averaging, 10^{-23} W / Hz of noise (3 pA / $Hz^{1/2}$ of input noise current), a 50-MHz receiver bandwidth and 20-ns pulses produce 3-m spatial resolution at a 1-km range, with an snr > 1. These numerical figures will help define the target system, after a brief look at local launch.

2.4 The Merits (and Demerits) of Local Launch

In the system we have assumed so far, the signal is coupled into the fibre at the end, a distance upstream from the test point. The power of the probe pulse arriving at the bend tap could be attenuated by orders of magnitude, depending on its wavelength. Locally injecting the probe pulse helps eliminate this attenuation and the uncertainty in effective launched power, but it has some drawbacks.

Local launch techniques have very low efficiency. They are meant mainly for low-frequency operations such as fibre identification[11] or active alignment in fusion splicing. The large receiver bandwidth necessary for OTDR admits more noise, further degrading the snr. On the positive side, local launch offers a fixed measurement range and possible testing on live fibres, using light at a wavelength other than that of the traffic, provided that the link budget has enough margin for the injection unit and the tap. With the bends we used, losses are about 2 dB at 1310 nm and 4 dB at 1550 nm[12].

11. One such product is Northern Telecom's Identifiber. More recent ones include that described in Reference 28.

12. These two-way loss figures are based on information on the Identifiber's optical characteristics, disclosed by Shawn Morrison of Northern Telecom, Saskatoon, Saskatchewan.

Local-launch and head-launch OTDR schemes diverge in optimal source wavelength. Figure 2·13 compares the backscattering levels at 830 nm and 1310 nm. With equal launched power, 830 nm has higher initial return than 1310 nm. But 1310 nm travels further than 830 nm because of lower attenuation. For head-launching, long-wavelength sources are essential since the severe attenuation at short wavelengths limits the source-to-tap distance. For local-launch, short-wavelength sources should be used for higher initial response.

Although local launch permits possible testing on live fibres, proper filtering is required. The absence of filters in normal fibre links prevents tests on live fibres close to the receiver. Otherwise the probe pulses would interfere with the traffic. With 800-nm sources, a distance of several kilometres is needed for sufficient attenuation on the probe pulses.

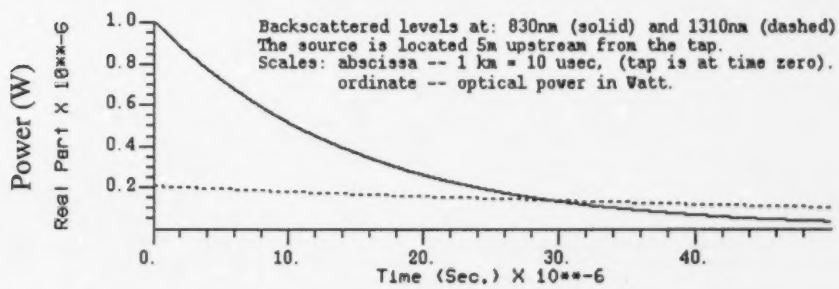

Fig. 2•13 Backscattering levels at 830 nm and 1310 nm, with equal launched power.

Another problem with local launch is that fibres which are single-mode at 1300 nm can carry at least two modes at 800 nm. Typical numerical apertures of single-mode fibres are about 0.11. At 800 nm, the normalised cut-off frequency is 3.63 and the LP-11 mode (the second lowest order mode) will propagate. The LP-02 mode (the third lowest order mode) might propagate but would be extremely sensitive to physical perturbation on the fibre. Modal dispersion is not expected to cause complications because of the short range. Also the LP-11 and the LP-02 modes are more lossy than the LP-01 (fundamental) mode. A mode

stripper, which can be made by winding a length of the fibre around a mandrel 3 - 5 cm in diameter, can be used to suppress the higher order modes.

2.5 Summary and Directions

The decision on operation wavelength is reduced to a choice between a longer range for longer measurement time or a shorter range for a shorter wait. Spatial resolution may be traded for range. Increased source power comes without an obvious compromise but entails a higher cost. Only the tap's coupling and receiver noise can be optimised and will deservedly receive the most attention.

In §2.2.2 we saw reason for giving first priority to noise reduction in the pre-amplifier. Analyses in the same section illustrated the difficulties involved in the analogue-to-digital conversion process and the barriers it places on the dynamic range, linearity and spatial resolution. We will not attempt to optimise the signal processing. Established performance figures (of signal processors in commercial OTDR sets) will be assumed.

Simulation results visually illustrated the practical effects of the various factors in the OTDR maker's formula and the source wavelength requirements in local launch. They also provided guidelines for establishing the target system.

The optical designs of an mid-span OTDR should be compatible with both long and short wavelength operations with, at the most, minor adjustments. The electronic designs will provide up to a 50-MHz bandwidth if needed, and will remain flexible for smaller bandwidths. The pre-amplifier will have equivalent input noise current at or below 3 pA / $Hz^{1/2}$ (~ 10^{-23} W / Hz, a common figure for good amplifiers). Also, designs are to incorporate as many existing components as possible to facilitate manufacture and improve consistency.

CHAPTER 3 Local Detection

The shape of a fibre bend controls the manner in which guided power leaks out of the fibre. A carefully controlled bend gives a well defined leakage (spatial) distribution. The optical system employed to couple the leakage to a photodetector should be simple, efficient and consistent. This chapter will describe bend tap designs we have investigated and present a survey on local launch techniques.

3.1 Leakage Through A Fibre Bend

The amount of bend leakage and its intensity distribution are related to the shape of the bend. Given that communication fibres have standardised layer thicknesses, the bend's radius and extent (angular distance) are the most important parameters. Many authors have dealt with the problem of bend loss in single-mode fibres [14, 17, 29, among many others]. For our purposes, only simple formulae are needed for estimating the amount of leakage. We will present only a qualitative review on the subject.

The bending of a fibre gives rise to a pseudo-potential and a resulting centrifugal force. The refractive index appears higher on the outside of the bend which is under tensile stress. The effective refractive index profile, $n_{eff}(x,y)$, is higher on the outside of the fibre bend although partially off-set by elasto-optic effect (the refractive index of silica decreases under tensile stress). Thus the effective bending radius, r_b, is larger than the actual bending radius. With the coordinate system in Figure 3·1, the effective refractive index is given [17] by,

$$n_{eff}^2 = n^2(x, y)\left(1 + 2\frac{x}{r_b}\right). \qquad \text{(Eq. 3•1)}$$

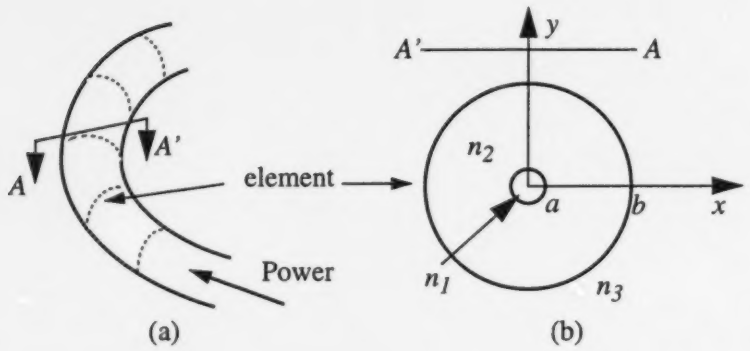

Fig. 3•1 Bent fibre: (a) 3-D view, (b) an elemental section. The fibre lies in the *xz*-plane.

The propagation constant of the fundamental mode in a bent fibre, β, differs from that in a straight fibre, β_0. The amount of leakage can be found from the difference between the imaginary parts of β and β_0. Since n^2_{eff} and the wave number, k, are real, the attenuation constant of a coated fibre, α_{bc} is given [17] by:

$$\alpha_{bc} = \alpha_b \frac{2(Z_3 Z_2)^{1/2}}{(Z_3 + Z_2) - (Z_3 - Z_2)\cos(2\Theta)}, \qquad \text{(Eq. 3•2)}$$

$$Z_j = k^2 n_j^2 \left(a + 2\frac{b}{r_b}\right) - \beta_0^2$$

$$\Theta = \frac{\gamma^3 r_b}{3k^2 n_2^2}\left(\frac{r_0}{r_b} - 1\right)^{3/2}, \qquad \text{(Eq. 3•3)}$$

$$k = \frac{2\pi}{\lambda}$$

where α_b is the bending attenuation if the cladding is of infinite extent, a is the radius of the core, b is the outer radius of the cladding, λ is the wavelength and r_0 is the critical radius,

$$r_0 = (2k^2 n_2^2 b) / (\beta^2 - k^2 n_1^2) . \qquad \text{(Eq. 3·4)}$$

If the refractive index of the coating, n_3, is the same as that of the cladding, n_2, then $Z_3 = Z_2$ which leads to $\cos(2\Theta) = 0$; α_{bc} is reduced to α_b.

Eq. 3·3 describes an attenuation characteristic that generally decreases exponentially with decreasing wavelength and increases with decreasing bend radius. When plotted against wavelength, α_{bc} exhibits periodic peaks due to $\cos(2\Theta)$. One can locate the peaks by setting $2\Theta = (2m - 1)\pi$, where m is an integer. The ratio between the height of a peak and that of the adjacent minimum can be shown to increase with bending radius and decrease (weakly) with wavelength. In other words, in a sharp bend, the amount of leakage is less wavelength-sensitive.

3.2 Power Distribution of Leakage

The leakage has been shown to have a Gaussian dependence in the direction normal to the fibre bend [29]. With reference to Figure 3·1, the electric field amplitude varies as $exp[-y^2/(w^2(x))]$, where the field width, $w(x)$ has an x-dependence: $2(x/\gamma)^{1/2}$, where $\gamma^2 = \beta^2 - k^2 n_{eff}^2(x, y)$. An infinite number of elemental sections such as that shown in Figure 3·1b make up a bend. Each radiates in a slightly different direction. An intensity pattern could be observed on a plane at $z = z_0$ and its spread increases with the angular extent of the bend. A small bending angle gives a tighter output "beam." There is a lack of data for leakage with small bending radii in published papers so we measured bending leakage with small bending radii (< 5 mm) before specifying our bend tap.

Two-metre long pieces of telecommunication fibre[13] were connected to a laser source emitting at 780 nm, one piece at a time. Approximately 1.5 m of fi-

13. The fibre used was made by Northern Telecom, has a 9-μm core, 125-μm cladding, 250-μm coating (all figures are outer diameters). The fibre is single-mode at λ = 1300 nm. At least two modes propagate in the 780 – 830 nm wavelength range.

bre was wound into loops ~ 5 cm in diameter to strip cladding modes as well as to suppress the higher order propagating modes. The power through-put before and after mode-stripping is about 120 μW and 70 μW. The remaining length downstream from the mode stripper was put into bending jigs with controlled bending radii and angles. The exit end was cleaved and coupled to a the detector of a power meter. Figure 3·2 illustrates the set-up.

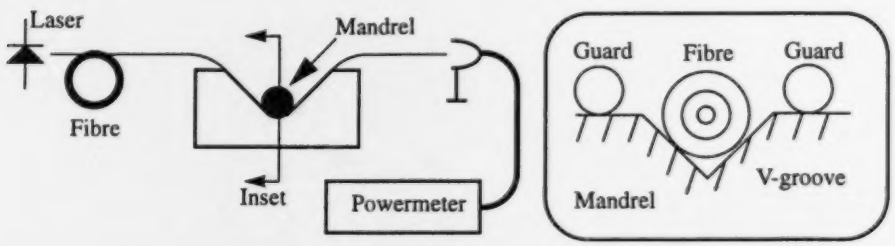

Fig. 3•2 Experimental set-up for leakage measurements. Inset: v-grooves on a mandrel's surface: the core is roughly flush with the surface.

The mandrels were machined out of drill rods with v-grooves cut into their surfaces to hold the fibre pieces in place. To avoid excessive squeezing of the fibre, rigid guards were attached to the jig on either side of the bent fibre. The mandrels were held down by elastics. A sample of the results is plotted in Figure 3·3. An exponential curve has been fitted to the data from the 30 degree bend for reference.

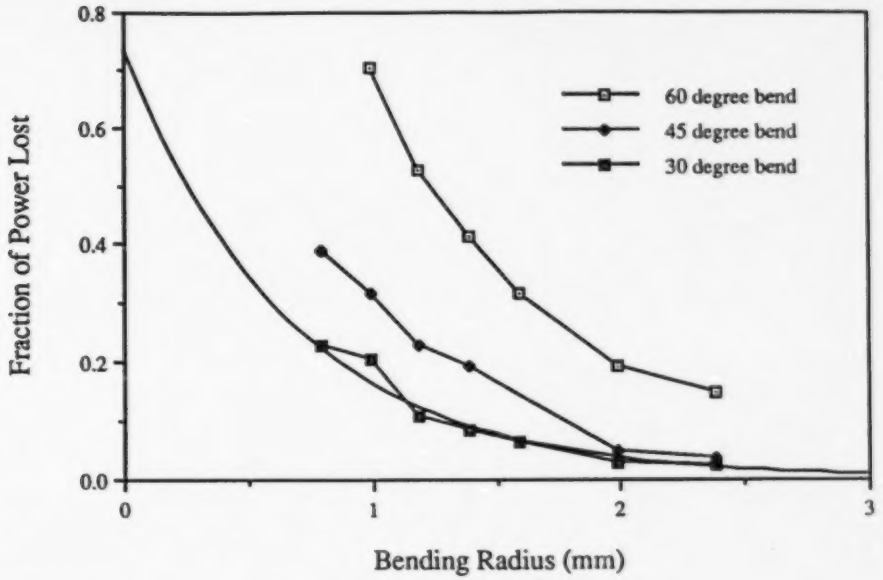

Fig. 3•3 Bend leakage versus bending radius for various bend angles.

The intensity distribution of the leakage was measured as shown below. A silicon detector (hp 5082-4203, measured responsivity = 0.44) was used. A typical distribution is shown in Figure 3·5.

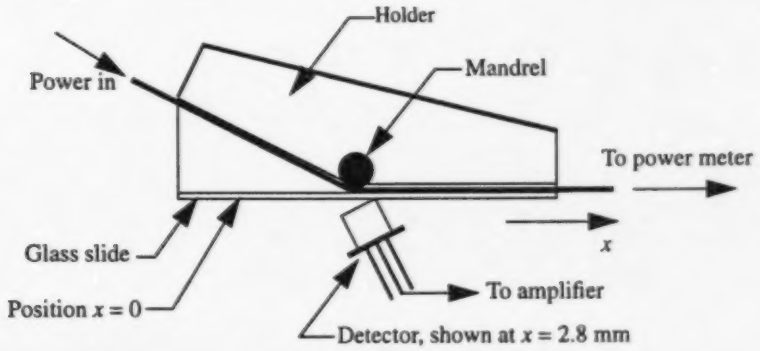

Fig. 3•4 Apparatus for measuring leakage intensity distribution.

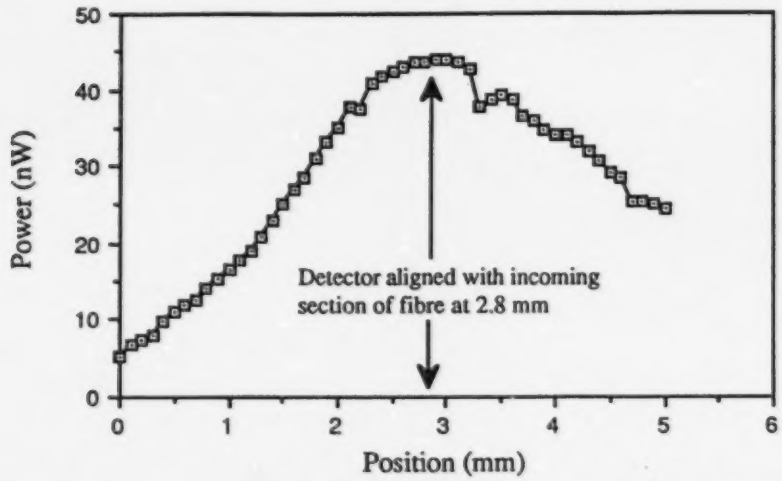

Fig. 3·5 Leakage pattern from a 30-degree bend with a radius of 1.5mm.

Measurements with larger bending angles gave wider distribution patterns as expected. The indistinct secondary lobes in Figure 3·5 are thought to be caused by the interference set up by multiple reflection between the core-cladding boundary and the cladding-jacket boundary. As the bending angle increased, more lobes appeared, but grew less distinct as the power drops. It is necessary to use smaller bending angles for more efficient leakage collection.

3.3 Bend Tap

Tapping ratio, f_t, and leakage coupling efficiency, η_C, are figures of merit of a bend tap (cf. Eq. 2·13). Discussions and data in sections 3·1 and 3·2 point to the advantage of small bending radii and small bending angles. Empirically obtained optima are: radius $\approx$ 1.5 mm and bending angle $\approx< 20°$.

Instead of making a new device, we based our bend tap on the optical window of Northern Telecom's Identifiber which has been optimised for the telecommunication wavelengths, 1310 nm and 1550 nm. We confirmed its useful-

ness at shorter wavelengths and experimented with different schemes for coupling the leakage to a detector. Each scheme called for modifications on the Identifiber window. The main objective was to maximise margins for misalignment between the bend, the detector and any optical components in between. We also sought to use a smaller detector than the one used in the Identifiber, without compromising the coupling efficiency. The reason for a smaller detector will be explained in Chapter 4.

3.3.1 The Identifiber window

The Identifiber window is injection moulded with polycarbonate which has a refractive index of 1.5. It is shown in Figure 3·6.

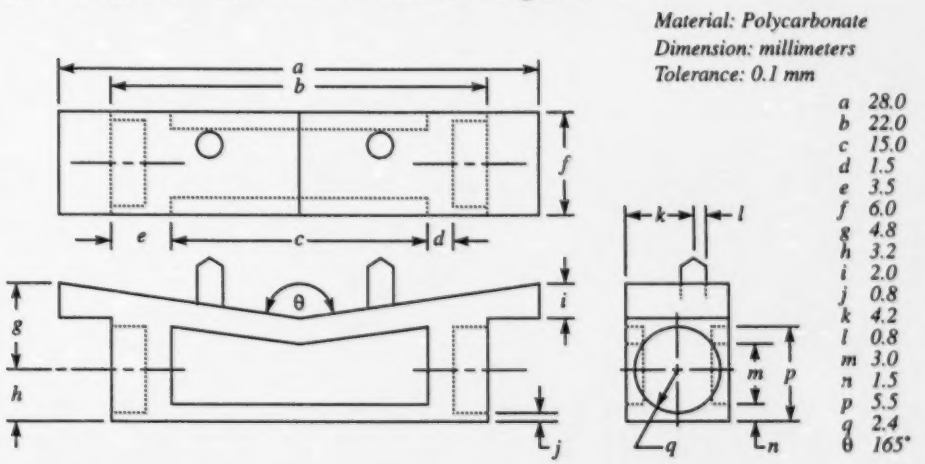

Fig. 3·6 Optical window of Northern Telecom's Identifiber.

In the Identifiber, a germanium detector (chip size: 1 mm dia., housing size: 5 mm dia.) sits in the receptacle at each end. A spring-loaded mandrel of 2 mm radius bends the fibre in the central depression. At 1310 nm, the leakage is 1 dB; and 2 dB at 1550 nm. The 1-mm detector collects roughly 25% of the leakage which has divergence angles roughly the same as the numerical aperture (NA) of the fibre[14]. To obtain figures at a shorter wavelength, we measured the 2-D distribution of the leakage at 780 nm, with a modified window, as shown in

Figure 3·7. A short piece of polymer fibre (1 mmϕ) was used as pick up. We measured the *coupling function*, f_c, which is the amount of power coupled to the detector as a function of position:

$$f_c = \iint_{x\,y} I_l(a,b)\, A(x-a, y-b)\, dbda, \qquad \text{(Eq. 3•5)}$$

where $A(x,y) = 1,\ (x^2+y^2 \le 0.5mm)\ ; = 0$ (elsewhere), is the admittance function of the pick-up fibre looking *out of* the end of the pick-up fibre and $I_l(x,y)$ is the intensity distribution.

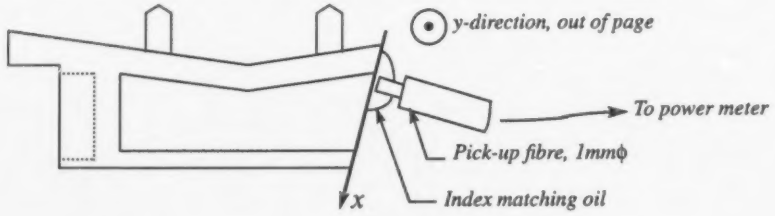

Fig. 3•7 Modified Identifiber window for measuring output distribution.

The coupling function is symmetric about the peak and has a spread of just over 1 mm in the *y*-direction (single-sided, 10% peak value). Near-symmetry is observed in the distribution along the *x*-direction. It has a spread of just under 1 mm; the peak leans toward the negative direction. Deconvolving the coupling function yields the power distribution which has a single-sided spread of ≈ 0.5 mm. Since the pick-up fibre is located about 9 mm away from the bend, the (single-sided) divergence of the output beam is 0.11 (≈ NA of the fibre).

3.3.2 Modifications to the identifiber window

The Identifiber window requires some alterations for our use. Large area detectors are required for collecting the distributed bend leakage. However de-

14. From private communication with members of the technical staff at Northern Telecom, Saskatoon, Saskatchewan.

tector size comes at the expense of bandwidth . The original, 1-mm wide detector mated to the window has a dynamic capacitance in the order of 50 pF (under bias). It also has a two-fold implication in receiver noise performance which will be discussed in the next chapter.

Positioning the detector close to the bend improves the collecting efficiency. The closest a detector could get to the bend is about 7 mm at which distance the detector housing starts interfering with the fibre, as shown in Figure 3·8(a). The scheme illustrated in Figure 3·8(b) places the detector about 5 mm from the bend without interfering with the fibre. Two methods were used to create the reflecting surface. First, the surface was polished to create total internal reflection (the angle of incidence is made to be larger than the critical angle). A four-step wet process ending with 0.3 μm grid gave a surface with minimal diffusion loss. Second, a tile of aluminised silicon substrate was attached to the surface with index-matched epoxy, giving better than 90% reflectance in the near infrared. In comparison, the first method is arduous.

Although more efficient than scheme (a), scheme (b) leaves little mechanical support for the mandrel since little is left under the trough in which the fibre is bent. Lenses were used in an attempt to combine the best of both schemes. Analyses and syntheses of the use of lenses were accomplished with geometric optics (ray tracing). We will present a summary of ray tracing before describing the details of our apparatus.

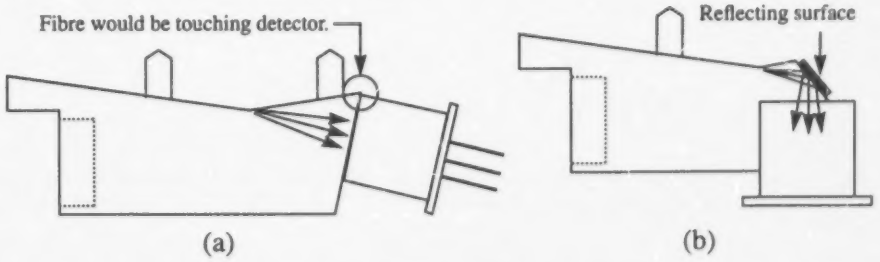

Fig. 3·8 Two schemes of modification on Identifiber window.

3.3.3 Summary of ray tracing matrices

Once guide light has leaked through a fibre bend, it can be treated with geometric optics. It is assumed to travel without confinement and interacts only with components too large for its wave properties to manifest themselves.

Each ray is a path which can be described by a tangential vector at every longitudinal position. General ray matrix theory deals with azimuthally symmetric optical components and rays co-planar with the optic axis. Figure 3-9 shows the coordinate system. A common reference position is replaced by a series of relative positions so that the z-positions are not needed. The direction of travel is specified by the angle, θ and the radial position of the path by r.

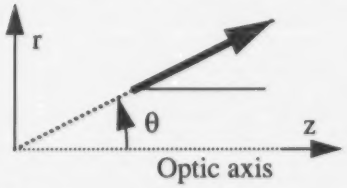

$$r = \begin{bmatrix} r \\ \theta \end{bmatrix}, \qquad \text{(Eq. 3•6)}$$

$$\theta = \operatorname{acos}\left[\frac{1}{|r|}(\hat{z}\cdot r)\right]. \qquad \text{(Eq. 3•7)}$$

Fig. 3•9 Coordinates for ray matrix.

Two points in a ray's path are related by a transformation representing the transitions and interactions with surfaces and media lying in between.

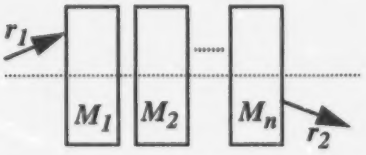

$$r_2 = M_n \ldots M_2 M_1 r_1$$
$$r_2 = M r_1 \qquad \text{(Eq. 3•8)}$$

Fig. 3•10 Cascade of optical components.

where the M's are 2 x 2 matrices. Appendix C contains a list of relevant basic ray matrices. All matrices were derived with the paraxial theorem. Consistency demands that the small angle condition be kept throughout the analyses and discussions to follow.

3.3.4 Bend tap with GRIN lenses

GRaded INdex lenses were mated to our modified identifiber windows either to permit the use of smaller detectors and/or to improve the coupling efficiency. These lenses are small glass rods whose refractive indices have quadratic radial variations (Figure 3·11). A general matrix for GRIN lenses is given in appendix C.

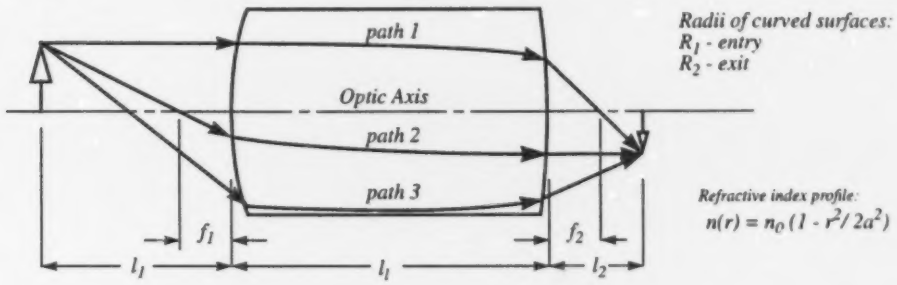

Fig. 3•11 Rays in a GRIN lens and nomenclature.

We experimented with plano-convex (one convex surface) lenses from the PCH and PCW families, by Selfoc[15] (specifications are listed in Appendix D). They are special cases of the general equations listed in appendix C. The design process and lens choice started with the constraint of minimal material reduction on the window and a minimum lens-to-detector distance of 0.5 mm, set by the detector housing.

Relations between object and image distances were derived by combining Eqs. C·8 and C·11. Referring to Figure 3·11, a ray reaching l_2 is described by

$$\begin{bmatrix} r_2 \\ \theta_2 \end{bmatrix} = \begin{bmatrix} r(A + Cl) + \theta_1 (Al_1 + B + Cl_1 l_2 + Dl_2) \\ Cr_1 + Cl_1\theta_1 + D\theta_1 \end{bmatrix}. \qquad \textbf{(Eq. 3•9)}$$

15. The major differences between the two types are the refractive index profile. PCH has a higher axial refractive index and a smaller quadratic variation constant, a (see specifications).

In an image-forming system such as a lens, r_2 is independent of θ_1; $(Al_1 + B + Cl_1l_2 + Dl_2)$ must be zero, which leads to

$$l_2 = -(Al_1 + B) / (Cl_1 + D)\text{, and} \qquad \textbf{(Eq. 3•10)}$$

$$r_2 = r_1 (A + Cl_2)\text{.} \qquad \textbf{(Eq. 3•11)}$$

Figure 3·13 (next page) illustrates Eq. 3·10 with two types of GRIN lenses available to us. The legends specify the type of lens and which surface is admitting. With fixed image locations, the object locations change by a few percents when the wavelength is changed from 800 nm to 1300 nm, and vice versa.

Two possible schemes are illustrated in Figure 3·12. Scheme (a) places a PCW lens at 1.5 mm (equivalent to 1 mm in air, the Identifiber window has a refractive index of 1.5) from the bend, its convex surface admitting. Scheme (b) places a PCH lens at an effective distance of 9 mm from the bend (6 mm in air), with its flat surface admitting.

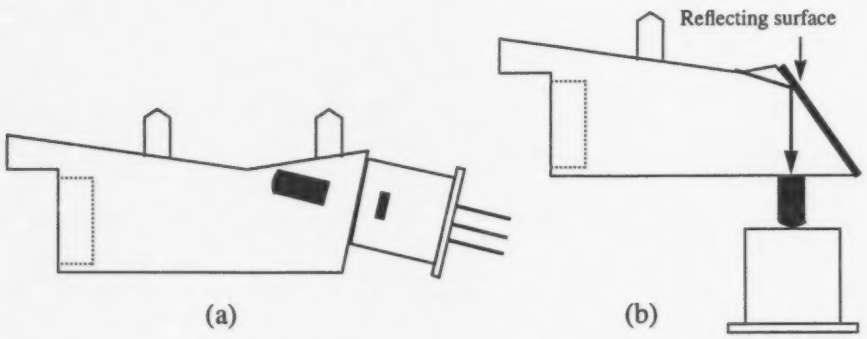

Fig. 3•12 Two schemes for using GRIN lenses with identifiber window.

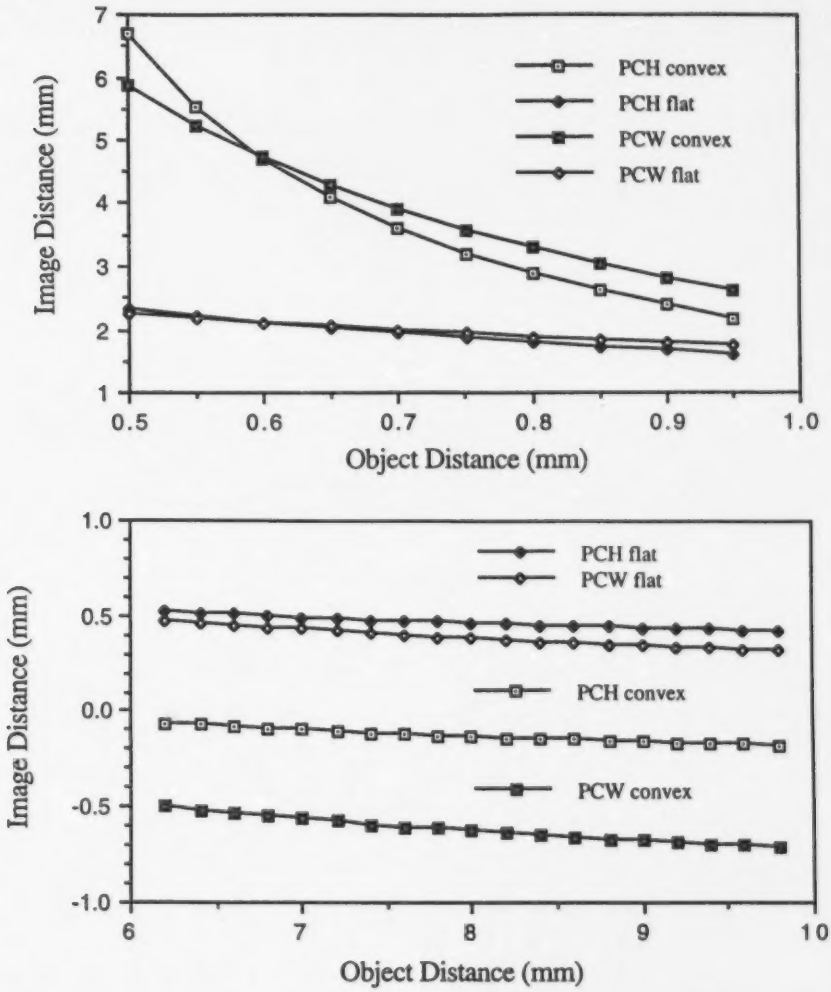

Fig. 3•13 Comparison of different GRIN lens configurations: object and image locations.

In scheme (a), the total distance from bend to detector is approximately 9 mm. The only modification on the original window is a hole to be drilled from the detector receptacle (see Figure 3·6). This fits the requirement of minimal reduction but does not save the scheme from manufacturing difficulties. Polycarbonate does not respond well to machining: it melts easily on being drilled. This scheme is sensitive to misalignment between the bend and the lens.

The slope of the image distance-versus-object distance curve (Figure 3·13) is a measure of the sensitivity to longitudinal object misalignment (i.e. error in object distance). Scheme (b) was adopted for its insensitivity to misalignment. This scheme also has superior lateral misalignment tolerance which can be measured by the ratio r_2 / r_1. According to Eq. 3·11, a shorter image distance, l_2, has an advantage in this regard.

A PCH lens was aligned to a 0.5-mm dia. detector. Detector and lens were set in a common jig mounted on a micro-positioner. A 9-μm fibre was bent lightly; approximately 25 μW of power leaked out[16]. Scanning the bottom of the window (refer to Figure 3·12b) we obtained the following typical coupling function (Figure 3·14) which shows a peak coupling of 30%. The best observed coupling efficiency exceeded 40%. (The original arrangement of the Identifiber collects about one quarter of the leakage with a 1-mm-diameter detector.)

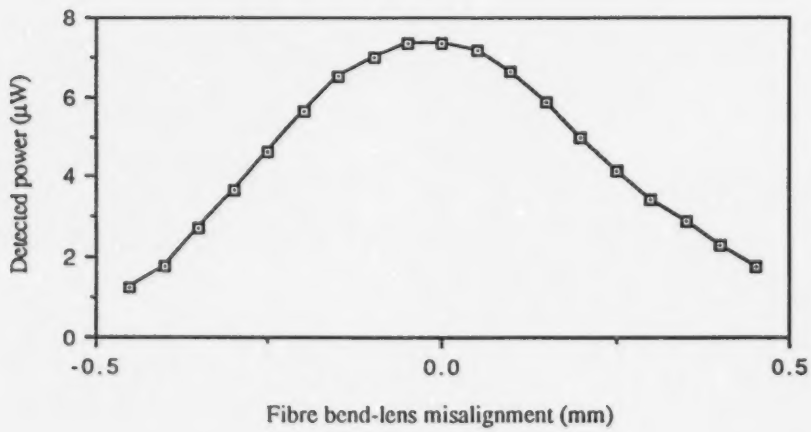

Fig. 3•14 Coupling function of modified identifiber window with mirror and GRIN lens.

16. The low power level was due to the inefficient coupling between our source's 50-μm-core pig-tail to the 9-μm-core fibre. Total launched power, after mode-stripping, was only about 70 – 80 μW.

In strict terms, the assumed azimuthal symmetry does not apply to the bent fibre as a source. Also the very small focal spot predicted by tay matrices cannot exist physically. Although the formalism of optics required to investigate the effects of these discrepancies is beyond our scope, it is still essential for us to understand the error(s) ray theories introduce and the necessary design margins.

The bent fibre can be considered as a series of sources located at slightly different positions relative to the lens. The superposition of all the waves emitted by these sources result in a beam with a very complicated constant-phase surface (if any such surface exists). The divergence of such a beam is much worse than a beam with a smooth constant-phase surface (one such as the lowest order Hermite-Gaussian beam). The Law of Brightness demands that the flux per unit solid angle of a beam cannot be increased. In other words, the divergence of a beam increases when the power is concentrated in a tighter spot. In our case, the focused beam's divergence is very large. The implication is that the lens-to-detector distance is more critical than is suggested by Figure 3·13. The effective aperture of the lens is slightly less than 1 mm in our configuration (see appendix C for formula). This represents a further degradation of the divergence. In our experiments, detectors with active diameters of 0.5 mm placed behind the lens could be misaligned laterally by up to 100μm before noticeable decrease in power coupling (10%) was observed. This effectively sets the minimum active diameter of the detector to 300 mm.When the detector was moved back from the lens by ~100 μm (a reasonable tolerance), a lateral misalignment of 50 μm was enough to decrease the coupled power by 50%.

3.4 Local Launch

As part of the study, local injection of probe pulses was considered as an alternative to launching at the head end. A literature search revealed a best-so-far efficiency of -18 dB, launching into a coated single-mode fibre, at $\lambda = 1310$ nm [30]. The apparatus induced microbends in the fibre to produce a "resonance" in

the cross coupling between the fundamental mode and (a few) cladding mode(s). A user "hunts" for these cladding modes by adjusting the laser's orientation. In the long run, there would be a net power transfer from the cladding mode(s) to the better confined fundamental mode. No details were provided by the authors on the theoretical basis or the geometric parameters of the microbends.

In the face of the rather satisfactory results in the previous section, it was tempting to adapt the identifiber window for local launching as well. We obtained from Bell Northern Research the local injection detection (LID) block, on which the identifiber's window was based. Experiments using the same basic lens-fibre bend arrangement (Figure 3·16) were conducted, with the pig-tailed laser replaced by a broad-area quantum-well laser diode which has a pulsed output power of 300 mW[17], at $\lambda = 861$ nm. Details of the laser driver are contained in appendix G. The laser and a GRIN lens were aligned to each other and moved in unison. The results are presented in Figure 3·17.

From our measurements, the original BNR LID block has a typical launching efficiency of approximately -40 dB (-37 dB, best), into a piece of 9μm-core fibre (laser output: 1 mW nominal, launched power: 100 nW). Misalignment was suspected to have caused inconsistency in launch efficiency. Our experiments with the quantum-well laser diode yielded efficiencies at -50 dB (typical) and -46 dB (best). This low efficiency was caused by the wide divergence of the broad-area laser. Also, the focal spot of the laser is rather large (the spot measured ~ 200 μm). This explains the width of the coupling function in Figure 3·17 which is much wider than the fibre core. It was not possible to obtain an even small focal spot because the disparate angles of divergence (parallel and

17. The broad area quantum well laser diodes were made by SSOC, Ottawa and packaged at TR-Labs by Dr. Barrie Keyworth and Rohit Sharma. The lasers' nominal outputs are rated at ~500 mW when driven by a 1.6-A current. 1.5-A current pulses drove our lasers. Large divergence of the output beam prevented us from collecting the full power, only about 300 mW was channelled into a GRIN lens and about 250 mW was focused onto an area 1 mm in diameter.

perpendicular to the diode junction). The focal "spot" is either a fine line or a blurred spot: half way between a horizontal line and a vertical line.

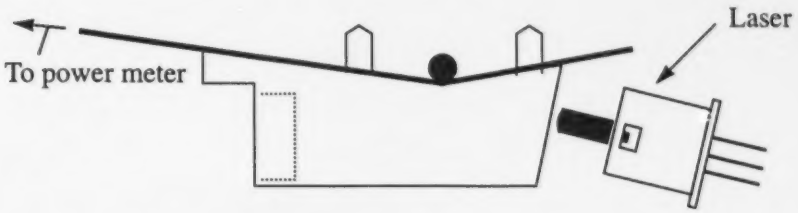

Fig. 3•15 Arrangement for local injection experiment.

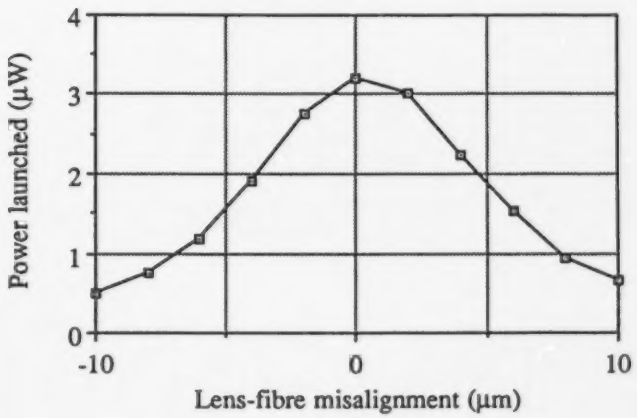

Fig. 3•16 Locally launched power and fibre bend-lens/laser misalignment.

3.5 Summary

We have considered relations between bending leakage, leakage pattern and bend shape. A bend tap was made, based on an existing component and guided by measurements of leakage patterns. Graded index lenses were introduced to maintain good coupling efficiency with reduced detector size, and to decrease sensitivity to misalignment. Realistic performance figures were measured: up to one-third of propagating light (λ = 780 nm) can be tapped (50% at λ = 1300 nm), Of this leakage, 30% can be coupled to a detector with a 0.5-mm (dia.) active surface.

Experiments with local injection gave clues to the cause of its low efficiency. Measurements indicated that alignment precision in the order of 1 μm is necessary to obtain consistent injected power. Once the alignment problems are solved, a laser with better beam quality should be used. Single-mode laser diodes with output in excess of 100 mW are already available commercially. Improvements in these areas will make local launch much more viable.

Knowing the limitations of the bend tap, we will turn our attention to the necessary electronics circuits.

CHAPTER 4 Electronics

The receiver to be used with our bend tap must be able to cope with the large capacitance associated with a large detector specified at the end of §3.3.4. This chapter will document the studies conducted in search of such receivers. Studies on the influences of detector capacitance on bandwidth and noise will lead to a choice of detector. A receiver built entirely with commercially available amplifiers will be described. A (mostly theoretical) study on a custom pre-amplifier will follow. Most formulae in this chapter are well known. Most equations will be stated without derivations.

4.1 Detector Choice and Receiver Design Target

4.1.1 Influences of detector capacitance

Optical receivers are designed and evaluated as amplifiers with transimpedance gains. Other applicable figures of merit are gain-bandwidth product, equivalent input noise and sensitivity to loading. All these figures are influenced by the input capacitive loading. In our case this loading comes from the photodetector.

A large detector capacitance reduces a receiver's gain-bandwidth product (GBP). The manufacturing tolerance on the detector's capacitance challenges the amplifier's sensitivity to input capacitive loading. Large-area detectors' dynamic capacitance have values that could be order(s) of magnitude larger than those of

detectors normally used for communications. The manufacturing tolerances of a large area detector could exceed the capacitance of a normal detector (< 1 pF).

A large capacitance has implications in the amplifier's noise performance. A receiver with a low gain-bandwidth product must use low resistance to achieve the same bandwidth as a receiver with a higher GBP. Alternatively, the GBP could be raised by high-current bias on the amplifiers. However, both methods increase noise. As will be presented explicitly later, the total noise depends on the square of total input capacitance (i.e. amplifier input capacitance plus detector capacitance). The equivalent noise takes the form sketched in Figure 4·1. The numerical figures are from preliminary studies. The bandwidth is 50 MHz. Noise sources are lumped into a shunt source and a series source. The exact noise current depends on the specific circuit configuration. In general, a 3-dB penalty results from increasing detector capacitance, C_D, from 0 to 15 pF.

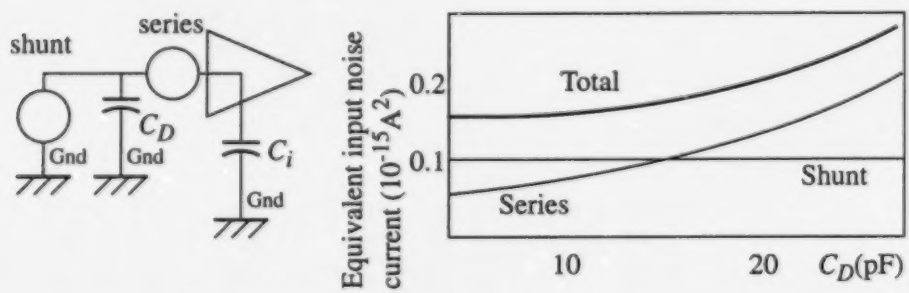

Fig. 4·1 Noise's dependence on detector capacitance, C_D.

4.1.2 Detector choice

The general guidelines for our search for detectors were, in descending priorities, a 0.5 mm diameter or larger, < 15 pF of dynamic capacitance under bias, good responsivity and package type (short distances between detector an front glass are preferable). An InGaAs p-i-n diode from EG&G (C30619) and another from Epitaxx (ETX 500) were selected for long wavelength operations. The former was chosen for its extremely low capacitance (8 pF nominal, under

5V reverse bias) and the latter for its very high responsivity (0.95 A/W at 1310 nm). For short wavelength operations, we chose a silicon p-i-n diode from NEC (NDL2208) for its 0.88 mm diameter and low capacitance (1.5 pF nominal, under 10 V reverse bias). Manufacturers' specifications for these detectors are listed in appendix E. These detectors are all housed in TO-18 packages. The distance from the front glass surface to the chip surface is 0.5 mm nominal.

4.1.3 Receiver Design Targets

A 50-MHz bandwidth for the receiver has been specified in §2.5. Now a low sensitivity to capacitive loading by the detector is also required, so that the large manufacturing tolerance of the large detector would have minimal effect on the amplifier's bandwidth. The amplifier bandwidth's sensitivity to detector capacitance is defined conventionally as the ratio between the fractional changes:

$$S_{C_D}^{BW} = \frac{\Delta BW}{BW} \Big/ \frac{\Delta C_D}{C_D}. \qquad \text{(Eq. 4•1)}$$

The measured capacitance of our "first-choice" detector for long wavelength (EG&G C30619) is ~ 6 pF under 15V of reverse bias and the manufacturer-supplied tolerance is 2 pF (possible change: $\delta = 33\%$). If we require the bandwidth to change by less than 10%, the sensitivity, $S_{C_D}^{BW}$, is 0.3 or less.

4.2 Pre-amplifier Topology

Eqs. 2·16 and 2·17 (page 16) asserted the importance of pre-amplifier noise; the pre-amplifier will receive the most attention. We will decide on a topology first. High-impedance (or integrating), matched and transimpedance (or feedback) are the three most popular (and studied) pre-amplifier topologies. Each one is particularly suitable for receiving certain types of signals.

High impedance pre-amplifiers achieve very high input impedance with FET's as first stages. A shunt resistance at the gate converts the photocurrent to a voltage. High impedance amplifiers trade bandwidth for low noise by increasing this shunt resistance, necessitating equalisation. Wide-band equalisation is very difficult; a reasonable equaliser cannot span more than three octaves of frequency. However, high impedance amplifiers (such as the commercially available PIN-FET packages) are still popular for VHF and UHF regimes for their relative simplicity and stability.

Each stage in a matched receiver is reactively matched to its adjacent stages (detector included). Reactive elements do not produce noise so this topology generally offers the best noise performance. Since each matching network is a band-pass filter, very wide-band performance is difficult to achieve. It is best suited for narrow band signals at very high frequency.

A transimpedance amplifier uses large resistance for low thermal noise and introduces negative feedback to reduce its apparent input resistance. It has the noise performance of a high impedance amplifier and circumvents the bandwidth limit. Since feedback systems are prone to instability, transimpedance amplifiers are difficult to design. Nevertheless, they remain the best compromise for HF and VHF operations. Furthermore they are commercially available and cost less than PIN-FET's.

4.3 A Simple Receiver Design

We searched for suitable, commercially available amplifiers to attain design simplicity. Applying the criteria outlined in §4.1.3, we chose Signetics's NE5212. It has a transimpedance gain of 14-kΩ, a 150-MHz bandwidth and an input noise current less than 2.5 pA / $Hz^{1/2}$ ($C_D = 0$). Manufacturer's specifications are listed in appendix F. A simplified schematic diagram of the pre-amplifier and the linear (gain) channel is shown in Figure 4-2.

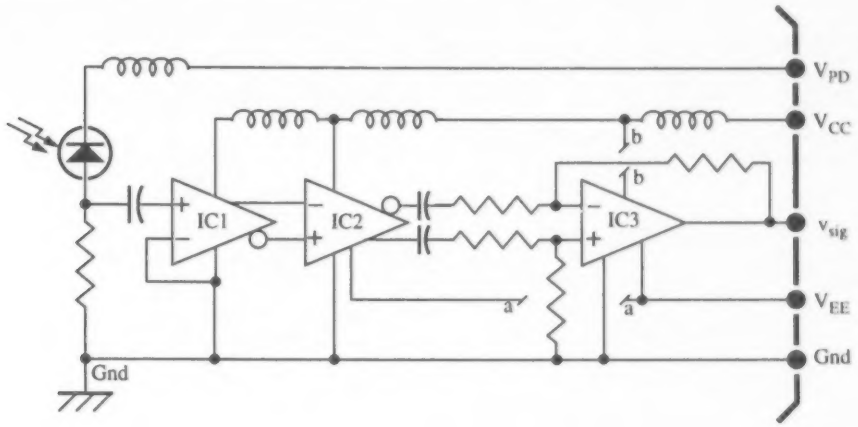

Fig. 4•2 Schematic diagram (simplified) of the receiver. IC1: NE5212 (Signetics), IC2: MC1733 (Motorola), IC3: LM6365 (National)

The NE5212's (IC1) differential outputs are coupled to a differential video amplifier for 30 dBV of gain. A high speed op-amp acts as a dual end-to-single end converter and provides some gain (6 dBV).

The nominal input capacitance of the NE5212 is about 11 pF. With the 6 pF dynamic capacitance of our detector attached to the front-end, the bandwidth of the amplifier drops to around 90 MHz, which is still more than ample. The bandwidth's sensitivity to detector capacitance variations is given by

$$S_{C_D}^{BW} = \frac{C_D}{BW} \cdot \frac{d(BW)}{dC_D} = -\frac{C_D}{C_i + C_D}, \qquad \text{(Eq. 4•2)}$$

where C_D is the detector's dynamic capacitance and C_i is the amplifier's input capacitance. With $C_D = 6$ pF, the sensitivity is about 0.35, falling just short of our goal. Nevertheless, it remains an eminent choice for short wavelength operations. With our short wavelength detector (NEC NDL2208, <3 pF), the worst-case sensitivity is about 0.21. However, the sensitivity must be lowered for use with the InGaAs detectors. This could be accomplished by shunting the input with a 15-pF capacitor, which would decrease the sensitivity to 0.19 and the bandwidth to 50 MHz. It is estimated that the input noise current would increase to 3 pA / $Hz^{1/2}$.

To our knowledge, there are no other wide-band, low-noise amplifiers optimised for large detector capacitance. We attempted to build a similar pre-amplifier and optimise it for our purpose.

4.4 Desensitised Pre-amplifier

According to Eq. 4·2, increasing the amplifier's input capacitance and/or decreasing the detector capacitance would desensitise the amplifier to front-end capacitive loading. Although a *real* capacitance, which is intrinsic to the device, can be decreased to a limited extent only (through bias), its *apparent* capacitance can be changed dramatically ($10^{\pm 2}$) by introducing feedback into the circuit. The effect of feedback can be summarised by Miller's Theorem (Figure 4·3). The apparent detector capacitance can be lowered by *positive* feedback, or bootstrapping (Figure 4·4). To get low bias voltage on the amplifier (for noise reasons) and high bias voltage on the detector (for reducing capacitance), decoupling capacitors must be used. This method is not suited for an OTDR receiver since Rayleigh scattered power concentrates around dc. However, in the case of an OTDR that uses correlation techniques (c.f. §2.2.3), in which the dc component is not important, bootstrapping should be used.

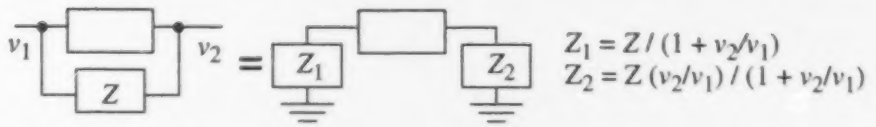

Fig. 4•3 Miller's Theorem.

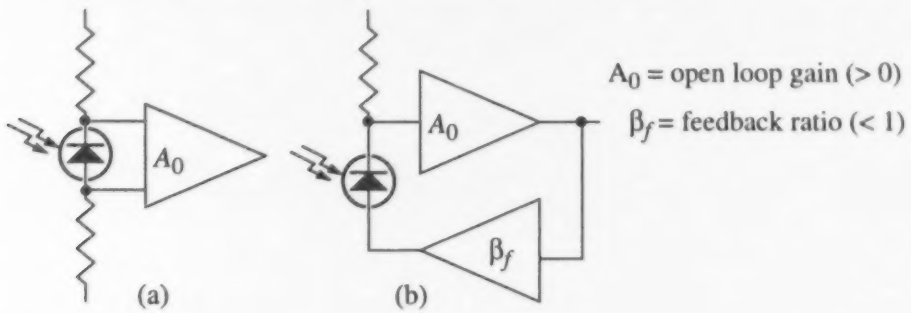

Fig. 4•4 Bootstrapping: (a) passive, (b) active.

Desensitising an amplifier with increased input capacitance may be done by an increase in the actual shunt capacitance which reduces the gain-bandwidth product and increases noise, or by increasing the Miller (apparent) capacitance in the front stage by increasing the gain [31] which preserves the gain-bandwidth product.

4.4.1 General feedback amplifiers

Specific design details were guided by the analyses summarised below. For the feedback system shown in Figure 4·5, we assume that the open-loop transfer function of the amplifier, $A(\omega)$, has two real poles located at ω_1 and ω_2 (angular frequencies) and the feedback is frequency-independent (β_f = constant). A_0 denotes dc gain. The overall system response is given by $A_f(\omega)$.

$$A(\omega) = -\frac{A_0}{(1 + s/\omega_1)(1 + s/\omega_2)} \qquad \text{(Eq. 4•3)}$$

$$A_f(\omega) = \frac{A(\omega)}{1 - \beta_f A(\omega)}, \qquad \text{(Eq. 4•4)}$$

$$A_f(\omega) = \frac{-A_0}{1 + A_0\beta_f} \cdot \frac{1}{1 + \frac{s}{1 + A_0\beta_f}\left(\frac{1}{\omega_1} + \frac{1}{\omega_2}\right) + \frac{s^2}{\omega_1\omega_2(1 + A_0\beta_f)}}. \qquad \text{(Eq. 4•5)}$$

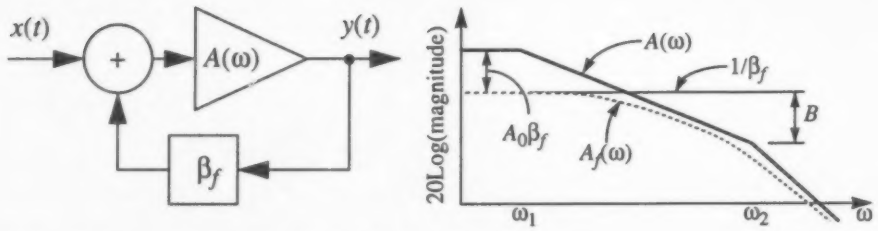

Fig. 4•5 General feedback schematic and frequency response.

An OTDR receiver should reproduce the probe pulse as faithfully as possible. It should have a pulse response with minimal rise/fall times and minimal over-/under-shoot. Short rise/fall times require a large bandwidth, obtainable by increasing feedback – a large $A_0\beta_f$ or a small B (referring to Figure 4·5). Over- and under-shoot are related to pole locations in $A_f(\omega)$. The relation between B and gain flatness can be calculated from Eq. 4·5. If ω_1 and ω_2 are separated by more than one decade, at B = 6 dB, $A_f(\omega)$ approximates a Butterworth filter (maximally-flat gain). At B = 10 dB, $A_f(\omega)$ approximates a Bessel filter (maximally-flat group delay).

These cases pose a lower limit on the second pole of the amplifier to be designed. For the Butterworth case $1/\beta_f$ should intersect $A(\omega)$ at $0.5\omega_2$, placing the upper -3-dB point at $\omega_0 = \sqrt{0.5\omega_2 + \omega_1}$. In the Bessel case, $1/\beta_f$ intersects $A(\omega)$ at $0.3\omega_2$, placing ω_0 at about 0.45 ω_2. In arriving at these results, we have ignored the third poles in $A(\omega)$, load capacitance, additional phase shifts from physical path lengths, finite input impedance and non-zero output impedance.

Ample phase and gain margins must be built into the open-loop response. The design must incorporate a high input impedance and a low output impedances.

4.4.2 Transimpedance pre-amplifier

Figure 4·6 below shows a common transimpedance amplifier.

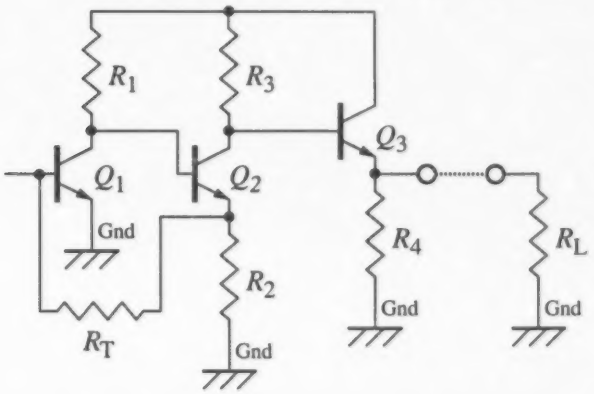

Nomenclature used in this thesis:
Q_1 – Front stage
Q_2 – Feedback stage
Q_3 – Buffer

Fig. 4•6 A common realisation of a transimpedance amplifier.

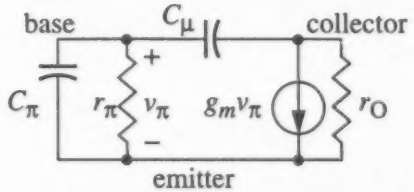

Fig. 4•7 High frequency BJT model.

Using the high frequency model for bipolar junction transistors (BJT) shown at left [32], one can obtain the frequency response of the front stage.

The feedback stage presents a parallel R-C load to the front stage. The feedback resistance, R_T, appears as an input shunt resistance. The open-loop gain (collector voltage / base current) is of the form [31]

$$A(\omega) = \frac{(g_{m1} r_{\pi 1} R_T R_1) / (r_{\pi 1} + R_T)}{(1 + s/\omega_1)(1 + s/\omega_2)}, \qquad \text{(Eq. 4•6)}$$

where the two poles, ω_1 and ω_2 are given by:

$$\omega_1 \approx \frac{(r_{\pi 1} + R_T)}{g_{m1} r_{\pi 1} R_T R_1 C_{\mu 1}}, \text{ and} \qquad \text{(Eq. 4•7)}$$

$$\omega_2 \approx \frac{g_{m1} C_{\mu 1}}{(C_{\pi 1} + C_D) C_{i2} + C_{\mu 1} (C_D + C_{\pi 1} + C_{i2})}. \qquad \text{(Eq. 4•8)}$$

The input capacitance of the feedback stage, C_{i2}, can be found by applying Miller's theorem.

$$C_{i2} = \frac{C_{\pi 2}}{(1 + g_{m2} R_2)} + C_{\mu 2} (1 + g_{m2} R_3). \qquad \text{(Eq. 4•9)}$$

Note that $C_{\pi 2}$ is reduced because of the positive shunt-series feedback from the emitter resistance, R_2.

After feedback, the upper -3 dB point can be estimated by

$$\omega_0 = \frac{(g_{m1} R_1 r_{\pi 1} + R_T)}{r_{\pi 1} R_T (g_{m1} R_1 C_{\mu 1} + C_{\pi 1} + C_D)}. \qquad \text{(Eq. 4•10)}$$

Eq. 4·10 actually represents the first order input R-C network of Q_1 in parallel with the Miller capacitance from $C_{\mu 1}$ and the Miller resistance from R_T.

In keeping with the gain flatness criterion (the Butterworth/Bessel cases), we need to push ω_2 beyond $2\pi \cdot 100$ Mrad/s. The most effective way to satisfy the condition $\omega_1 \ll \omega_2$ is to increase g_{m1} or R_1 (by increasing supply voltage which increases collector current and hence the gain). Changing any other variables in Eqs. 4·7 and 4·8 is ineffectual.

4.4.3 Noise Considerations

The largest contributors to shot noise are base and collector currents of the front stage and the detector currents (photocurrent and dark current). The dominant thermal noise sources are from the feedback resistor, R_T, and the collector resistor, R_1. In calculating the equivalent input noise current from the front stage collector, it is necessary to take into account g_m's frequency dependence.

Attaching the R-C pole of the input network of the front stage to its transconductance, we have [34]:

$$\frac{i_C}{i_{in}} = \frac{i_C}{v_{in}} \cdot \frac{v_{in}}{i_{in}} = \frac{g_{m1}}{1 + sR_{in}C_{in}} \cdot R_{in} \sim \frac{g_{m1}}{\omega (C_D + C_{\pi 1} + C_\mu)}. \qquad \text{(Eq. 4•11)}$$

The noise sources add up to:

$$\frac{d}{df}\langle i_n^2 \rangle = \begin{array}{l} 2q (I_{ph} + I_{dark} + I_{B1}) + \dfrac{4k_B T}{R_T} \\ + \left(2qI_C + \dfrac{4k_B T}{R_1}\right) \dfrac{\omega^2 (C_D + C_{\pi 1} + C_\mu)^2}{g_{m1}^2}. \end{array} \qquad \text{(Eq. 4•12)}$$

The first term sums up base shot noises which come from photo-current, I_{ph}, detector dark current, I_{dark}, and the transistor's base current, I_{B1}. The second term is the thermal noise from the feedback resistor, R_T. The third term sums up collector noises (often called series noise) which include shot noise from collector current, I_C, and thermal noise from the collector bias resistor, R_1. Noise increases with increasing detector capacitance because of the last term (see also Figure 4·1). Usually base noise dominates, as is our case. For very low thermal noise, R_T could be increased at the expense of bandwidth; equalisation would be necessary. This method reduces noise only if the equalisation stage does not introduce more noise than is reduced. The transfer function, $H_E(\omega)$, and equivalent input noise, $\langle i_E^2 \rangle$, from passive equalisation, as shown in Figure 4·8, are

$$H_E(\omega) = \frac{1 + s\zeta RC}{1 + (sRC\zeta)/(\zeta + 1)}, \qquad \text{(Eq. 4•13)}$$

$$\frac{d\langle i_E^2 \rangle}{df} = \frac{4k_B TR}{|A_f(\omega)|^2} \left(\frac{\zeta}{|1 + j\omega RC\zeta|^2} + 1 \right). \qquad \text{(Eq. 4•14)}$$

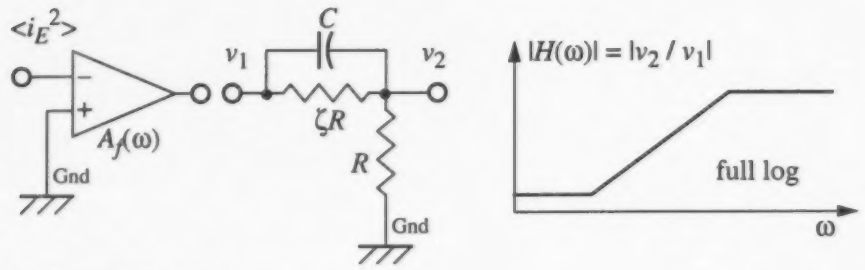

Fig. 4·8 Passive equalisation.

Further, the gain of an integrating pre-amplifier plus equalisation is less than that of the same pre-amplifier with more feedback and no equalisation. As feedback is reduced (larger R_T) to obtain higher gain and lower thermal noise, ζ must be increased accordingly. In theory, $R_T\zeta$ is constant and the gain-bandwidth product is invariant. In practice, the overall gain decreases with the introduction of equalisation. The optimal overall snr occurs when thermal noise from R_T is barely dominant. The exact value of the optimal R_T, however, is also influenced by other noise sources.

4.4.4 The final design

The design challenge lies in obtaining the most viable compromises between gain and bandwidth while maintaining the required noise performance. SPICE was used to evaluate gain and bandwidth performances, as well as sensitivity to component tolerances (by means of monte carlo simulation). According to Eqs. 4·6 – 4·12, the transistor must have a large unity current-gain frequency, f_T, and a small collector-base capacitance, C_μ. Motorola's MRF9331L was chosen for its 5-GHz f_T and 0.21-pF C_μ (< 0.3 pF guaranteed). The AC network also establishes the DC bias so no decoupling element is needed; the gain can be flat to dc. The transimpedance (before frequency compensation) may be adjusted to obtain bandwidths from ~5 to ~40 MHz without affecting the bias. An equalisation stage is provided. The final design is shown in Figure 4·9.

4.4.4.1 Circuit description

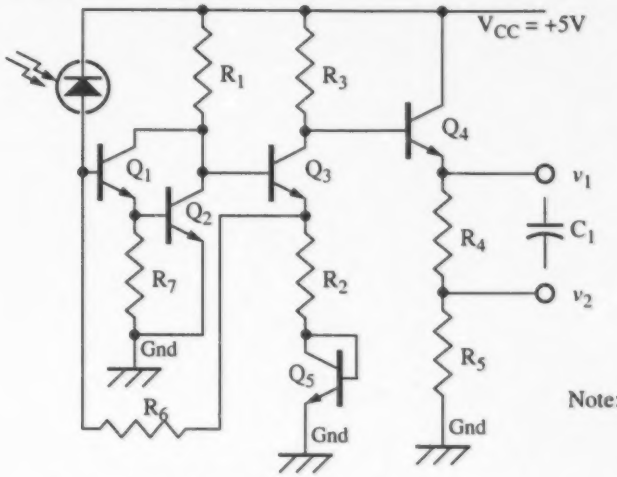

Q_1 - MRF9331L
Q_2 - MRF9331L
Q_3 - MRF9331L
Q_4 - MRF9331L
Q_5 - MMBR931L
R_1 - 1k20
R_2 - 511R
R_3 - 511R
R_4 - 1k80
R_5 - 220R
R_6 - 68k0
R_7 - 10k0
C_1 - 15p

Note: R_4+R_5 > 1k80 to protect Q_4. Listed R_4, R_5 and C_1 are for 50-MHz overall bandwidth.

Fig. 4•9 Final design of the mid-span OTDR receiver.

A Darlington pair replaced Q_1 of Figure 4·6 to accommodate the large value of R_6. MRF9331L is designed to operate at collector current levels down to 0.1 mA. The very low current in Q_1 still gave a 1-GHz f_T. $C_{\mu 1}$ is unaffected. The increased transit time ($1 / 2\pi f_T$) appeared as an increase in $C_{\pi 1}$ which is reduced by shunt-series feedback from R_1. Analytic results summarised earlier still hold, with minor adjustments. The transconductance, g_{m1} in Eqs. 4·6 - 4·12, is replaced by $g_m = g_{m1} + g_{m2}$ (the numbers in the subscript still reference the transistors). $C_{\mu 1}$ in Eqs. 4·7 and 4·8 is still $C_{\mu 1}$. Replacing $C_{\pi 1}$ in Eqs. 4·6 - 4·12 by $C_{\pi 2}$ gives good approximations.

The collector current of the front stage is set by R_1 and the supply voltage. Q_1 is biased to obtain the highest f_T of MRF9331L, 6 GHz. Q_3 splits the voltage two ways, with a near-unity gain. The combination of R_1 and R_3 gives a worst case (lowest) second pole at 95 MHz, according to Eq. 4·8. The gain of the front stage as calculated with nominal parameter values is about 96 V/V. Its nominal bandwidth is approximately 9.5 MHz (worst case 7 MHz) without detector or parasitic capacitance. Actual circuits were built and tested for realistic band-

width figures, i.e. including parasitic reactance. The circuit layout is included in appendix G.

4.4.4.2 Bandwidth and gain

In the absence of a calibrated long-wavelength light source, the circuit was tested with a network analyser while the circuit was embedded in a resistive network to provide isolation and prevent excessive front-end loading (Figure 4·10). Source power was kept below -10 dBm (at which about 6.4 μA enters the amplifier) so that no saturation occurred in any stage (maximum voltage is found at the collector of Q_3 – 0.43V). The equalisation stage was used for matching instead of equalisation. Table 1 summarises the bandwidth's dependence on front-end capacitance.

The very high dynamic input resistance of a photodetector would not load the input of a pre-amplifier. The 10-kΩ series resistor, however, presented a load to the input of the amplifier such that the overall input resistance was lowered. The input resistance of our pre-amplifier before embedding is given by

$$R_i \cong \frac{R_T}{1+g_m R_1}\Bigg\| \left(r_{\pi 1} + \beta_1 \left(R_7 \| r_{\pi 2}\right)\right), \qquad \text{(Eq. 4·15)}$$

where g_m is the combined transconductance of the Darlington pair. β_1 and β_2 are the current gains of Q_1 and Q_2 (~50). Low bias currents in Q_1 and Q_2 result in large $r_{\pi 1}$ and $r_{\pi 2}$ (>~10^3 Ω) so that $R_i \approx R_T / (1 + g_m R_1) \approx 600\Omega$, given that $g_m R_1 = 96$. Therefore the input embedding network presented a ~6% loading factor $(600/(10k + 600))$. Subsequently the expected bandwidth discrepancy was about 6%. Added parasitic capacitance at the input node decreased the measured bandwidth. Since the soldering pads were made to be small (~0.1 cm^2 in total), the total capacitance was kept under 1 pF, much less than the detector capacitance and amplifier input capacitance combined. Parasitic capacitance distributed within the 10-kΩ series resistor turned the embedding network into a high-pass filter. Nevertheless, the corner frequency was very high (a corner fre-

quency of 100 MHz with a 10-kΩ resistor would require a total capacitance of 160 fF which is very unlikely to be found in the 1206-size chip resistor we used). On the output side, the emitter of Q_4 drove a 1.5-kΩ load instead of the 1.8-kΩ as shown in Figure 4·9. This stage, an emitter follower, has flat response to $>10^9$ Hz (from SPICE simulations). The output load reduction was not expected to affect the in HF and lower VHF.

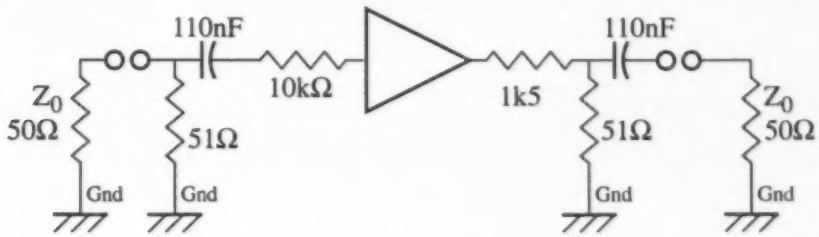

Fig. 4•10 Method for measuring transimpedance with a network analyser.

Table 1 Measured pre-amplifier bandwidths

Front-end capacitance	*Bandwidth*
$C_D = 0$ pF	7.15 MHz
$C_D = 5$ pF	5.76 MHz
$C_D = 6$ pF	5.50 MHz
$C_D = 7$ pF	5.25 MHz

From the data in table 1, the bandwidth's sensitivity to front-end capacitive loading, $S_{C_D}^{BW}$, is about 0.28 at 6 pF. Attempts to directly measure the voltage gain of the front stage were frustrated by the oscilloscope probes' insensitivity to the base voltage of Q_1 (~< 1 mV). We could only estimate the total input capacitance by $S_{C_D}^{BW}$. Using Eq. 4·2 (page 53) the input capacitance is calculated to be 16 pF, lower than the expected 19 - 21 pF ($A_V C_{\mu 1} + C_{\pi 2}$). This points to a gain that is lower than expected or that Q_1 has a lower than average C_μ. It is suspected that the 6-μA signal might have caused slight gain compression in the front stage.

To show the pre-amplfier's bandwidth possibility, one circuit was compensated to give a 50-MHz bandwidth (as shown in Figure 4·10). The upper trace in Figure 4·11 shows the magnitude response and the lower trace shows the phase. After accounting for the losses in the embedding network the gain is about 2.2kV/A.

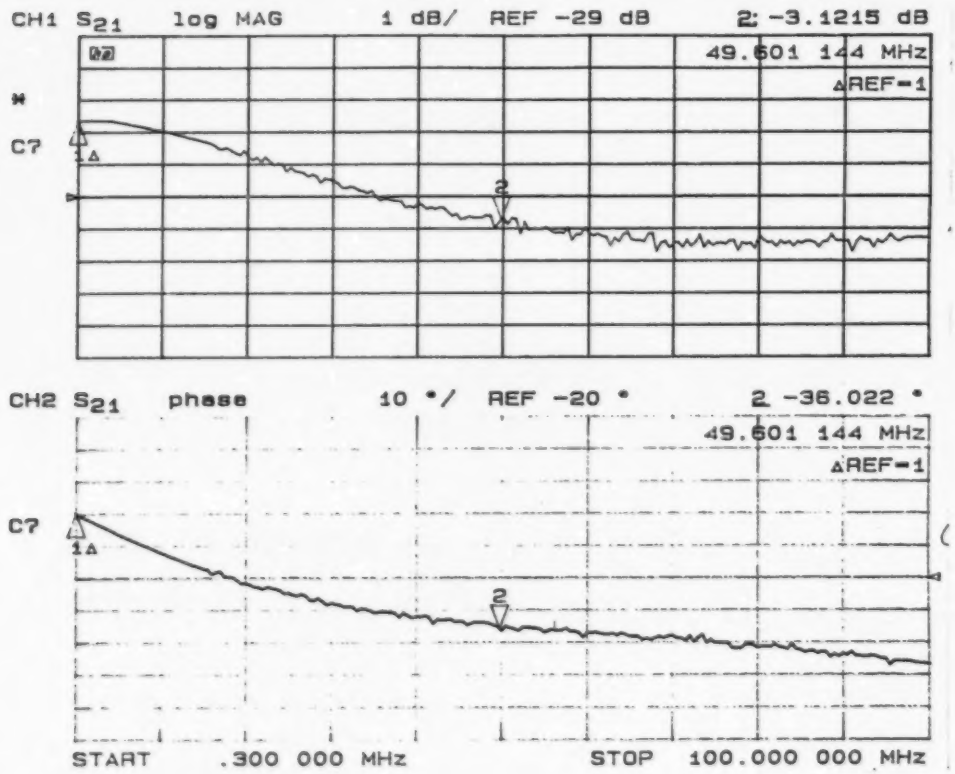

Fig. 4•11 Frequency response of pre-amplifier in the 50-MHz configuration.

4.4.4.3 Noise

With some typical values for the following parameters:

1. $C_D = 6$ pF,
2. $I_{ph} = 1$ μA,
3. $I_B = 2$ μA,
4. $I_C = 2$ mA,
5. $R_T = 68\text{k}\Omega$,
6. $R_1 = 1.2\text{k}\Omega$,
7. $C_\pi = 0.5$ pF and
8. $C_\mu = 0.3$ pF,

the worst case noise according to Eq. 4·12 is:

$$\frac{d}{df}\langle i_n^2 \rangle = \begin{matrix} 1.12 \times 10^{-24} + 0.254 \times 10^{-24} \\ + 0.460 \times 10^{-24} \end{matrix} \approx 1.8 \times 10^{-24} \left[\frac{A^2}{Hz}\right]. \qquad \textbf{(Eq. 4•16)}$$

In a 50-MHz bandwidth (noise bandwidth ≈ 75 MHz) the equivalent input noise current is about 13 nA. Combine this with our detector's responsivity of 0.85, the noise equivalent power is 15 nW, or -48 dBm.

4.4.4.4 Additional gain

The circuit was completed with the same arrangement shown in Figure 4·2, with the custom receiver replacing the Signetics NE5212. The decoupling capacitors prevented flat gain to dc. The bandwidth of the gain block, MC1733, is barely over 100 MHz and its roll-off characteristic suggests the presence of at least two poles in the vicinity. After compensation, the op-amp's (LM6365's) first pole is at 90 MHz; its second pole is at about 120 MHz. Coupling this to the MC1733, the overall receiver bandwidth of 50 MHz is difficult to maintain. Using formulae in Reference 35, we calculated that the pre-amplifier bandwidth would need to be 80 MHz to produce a 50-MHz overall bandwidth.

The next iteration of the receiver will replace the MC1733 by a pair of very wide-band differential amplifiers. A tentative circuit is shown below.

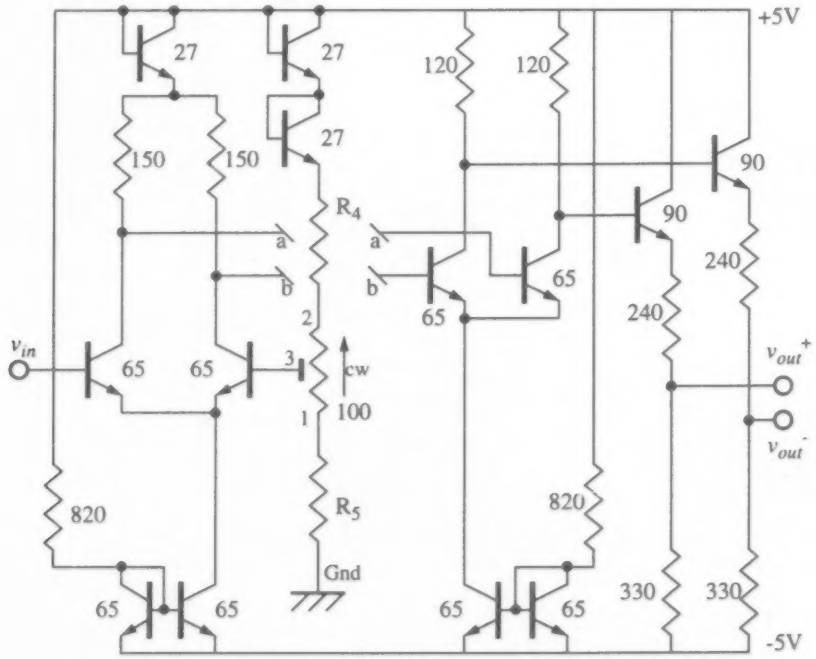

Fig. 4•12 Replacement gain channel for MC1733. R_4 and R_5 are to match R_4 and R_5 in pre-amplifier (Figure 4·8). '65' marks transistors in Plessey SL2365 (dual long-tailed pairs). '27' marks transistors in Plessey SL3227 (matched array). '90' marks BFR-90 (medium power RF amplifier).

4.5 Summary

We have arrived at two receiver designs, one built entirely with commercially available components, the other a custom pre-amplifier. The former is a 90-MHz amplifier well suited to receiving short-wavelength signals and is adequate for receiving long wavelength signals. It has 2.5 pA/Hz$^{1/2}$ of noise, or ~ 20 nA in 50 MHz and a sensitivity to front-end capacitive loading of 0.35 when attached to a detector with a 6-pF capacitance. Studies showed that the receiver specifications set forth in §2.5 can be better achieved with a custom pre-amplfier than with the commercial amplifier. The custom pre-amplifier has a sensitivity to front-end capacitive loading of less than 0.3 (6-pF detector capacitance), a noise current of 1.5 pA/Hz$^{1/2}$ (or 13 nA in 50 MHz) and a bandwidth that can be tuned without sacrificing the gain-bandwidth product. Further optimization will yield lower noise and lower sensitivity to front-end capacitance.

CHAPTER 5 Summary and Prospects

After considering the optical and electronic aspects of local detection in VHF and a survey on local launch techniques, we will summarise the work done up to this point, return to the system level and speculate on profitable future endeavours.

5.1 Summary

We reviewed the basic equations of optical time-domain reflectometry in Chapter 2. A modified OTDR maker's formula was developed for a mid-span, non-intrusive adaptation. An impulse response of fibre backscattering was derived to account for discontinuities, in addition to the uniform fibre of infinite extent. A simulator based on this impulse response was implemented to study the effects of local detection on the dynamic range and spatial resolution of an OTDR system. It was also used to arrive at a viable set of compromises between conflicting demands imposed by dynamic range, maximum spatial resolution and measurement time. In arriving at the mid-span OTDR maker's formula we found that the interpretations of dynamic range and measurement range are more complicated in mid-span OTDR than in conventional OTDR. Local injection was considered as a means to circumvent the range limit on mid-span OTDR and the complication of the interpretation of dynamic range. OTDR with local-launching was found to differ from OTDR with head-launching in optimal wavelength of operation. Simulation results and practical knowledge helped define a

set of targets. A course was then set to adapt local detection techniques for HF/VHF operations.

After an overview of bend loss in Chapter 3, it was determined that smaller bending radii and smaller bending angles give better defined leakage patterns which are also less wavelength dependent. Previous experimental results on bend leakage were extended to single-mode fibres with shorter wavelengths and smaller bending radii. A bend tap suitable for both long and short wavelength was specified, guided by empirical results. A bend tap based on an existing component, the optical window of Northern Telecom's Identifiber, was made. The window was modified to use smaller detectors. A lens was used to safeguard coupling efficiency against degradation due to reduced detector size. A minimum detector size was specified to provide margins for discrepancy between the synthesise (theories) and realisation (practice) of the optical arrangement. Tests conducted on the bend tap revealed a coupling efficiency that approaches figures assumed in early simulation. Local launch experiments were also performed. Component tolerances necessary for a consistent launching efficiency were found to exceed those offered by normal manufacturing techniques.

The large detector size specified in Chapter 3 necessitated a special purpose receiver circuit design, a topic tackled in Chapter 4. Two receiver circuits were designed. The first one was designed with commercially available components. It is well suited for short wavelength operations but is barely adequate should long wavelength and InGaAs photodetectors be used. We have custom-designed a photoreceiver which is tolerant to the large capacitance associated with large-area InGaAs photodetectors. The receiver has a bandwidth tunable over a reasonable range, has good noise performance and is insensitive to capacitive loading by the large photo-detector. In other words, we have shown that it is possible to construct a receiver suitable for use with a bend tap at high frequency.

5.2 Current Standing

Outputs from the simulator described in §2.3, incorporating realistic, reported figures and our empirical results help comprehending our current standing on mid-span OTDR. In Chapter 2 we considered the head-launched system operating at long wavelengths and the local-launched system with shorter wavelengths to be more viable to others. We will now return to them.

5.2.1 Head-launched OTDR

The simulation parameters are listed below.

1. Wavelength of operation: 1300 nm
2. Pulse length: 50 ns
3. Peak pulse power: 10 mW
4. Normalised fibre cut-off frequency: 2.4
5. Fibre numerical aperture: 0.11
6. Total fibre attenuation at 1300 nm: 0.4 dB/km
7. Source-to-tap distance: (a) 10 km, (b) 20 km
8. Bend-tap tapping ratio: 0.3
9. Detector coupling efficiency: 30%
10. Detector responsivity: 0.85
11. Receiver gain: 10 MΩ (overall)
12. Receiver bandwidth: 20 MHz
13. Noise equivalent power: 2.5 pW / Hz
14. Fibre termination: 0.9 km from tap

The spatial resolution is in the 5 m range. The following diagrams represent the output that would be displayed by a mid-span OTDR set with the bend tap and receiver we have described.

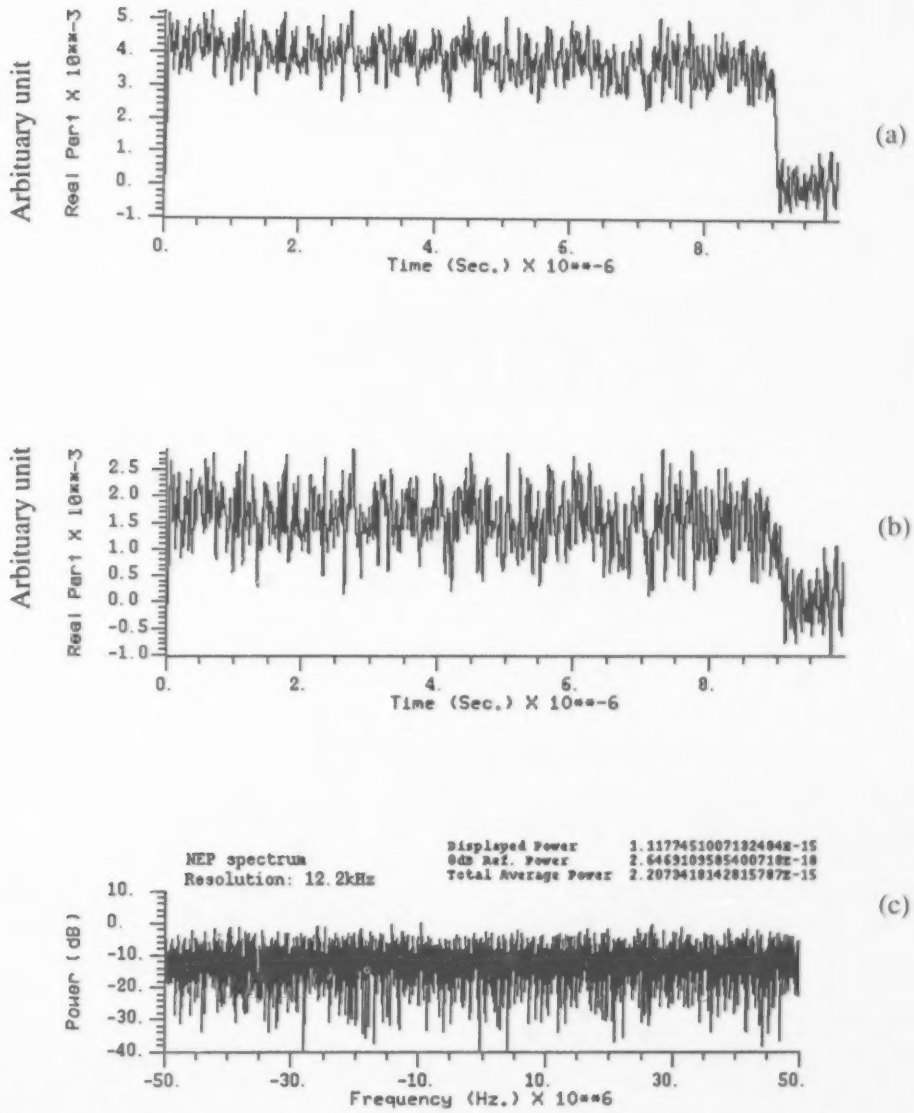

Fig. 5•1 Predicted mid-span OTDR output with currently achievable bend tap and receiver performance figures. (a) bend tap at 10 km from source. (b) bend tap at 20 km from source. (c) equivalent input noise current at the photo-detector.

5.2.2 Local-launched OTDR

Although local launch did not prove to be successful, it is not to be dismissed. If the highly efficient local injection method described in Reference 30 can be adapted for shorter wavelengths and if a high power laser diode[18] is used, a local launch mid-span OTDR would give an output such as that shown in Figure 5·2. The same simulation parameters were used except the follwing.

1. Wavelength of operation: 830 nm
2. Peak pulse power: 100 mW
3. Total fibre attenuation at 1300 nm: 2.0 dB/km
4. Noise equivalent power: 3.0 pW / Hz
5. Fibre termination: 0.5 km from tap

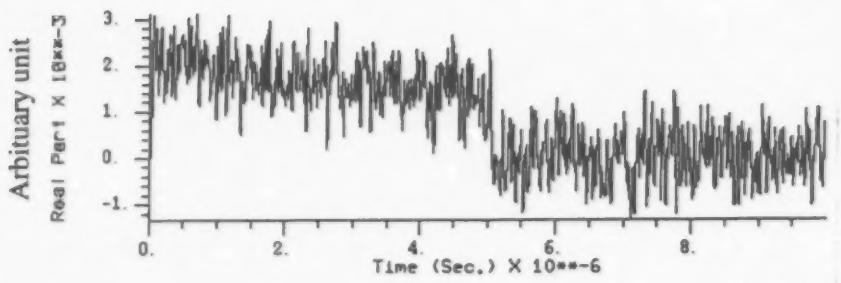

Fig. 5·2 Predicted local launch mid-span OTDR performance.

Comparison between Figures 5·1(b) and 5·2 reveals that local launch OTDR could give better performance than head launch OTDR if the test point is located more than 20 km away from the source. This distance shrinks with increasing spatial resolution.

18. For instance, among others, Spectra Diode Labs offers 150-mW single-mode laser diodes in 810 nm - 860 nm range (the SLD 5400 series).

5.3 Prospects

An existing, complete OTDR design could be fitted with a local receiver described in Chapters 3 and 4. The resultant equipment could be used in local loops which span approximately 10 km with fibres running through trenches underground or conduits in buildings, environs which limit access but offer many closely-spaced "landmarks" (splices, branch splitters, etc.) for meaningful high-spatial resolution measurements.

Further improvements are possible in many areas. One such area is signal processing. We have not assumed the benefits of having a dedicated processor, like that of a commercial OTDR set, which performs correlation, functions as a box-car averager and streamlines the measurement procedure. They were excluded because even the best processor would have difficulties salvaging a situation in which local detection/launch techniques are too inefficient for OTDR; we must first prove their viability. We have shown the viability of local launch which led to a limited form of mid-span OTDR. The immediate direction for further endeavour in mid-span OTDR lies in improving the efficiency and consistency of local injection. Many ideas are left unexplored. Among them, techniques borrowed from integrated optics could solve the alignment problems. Some of the experiments described in this thesis had at times used v-grooves etched in silicon to provide consistent precision in positioning. Taking this one step further, a waveguide grown on silicon might be used to guide and couple leakage from the bend to the detector or to guide power from a laser to a fibre bend.

At present, we have confirmed that head-launched mid-span optical time-domain reflectometry is possible for testing short to medium length fibre links with good spatial resolution.

References

1. Li, T., "Advances In Optical Fiber Communications: A Historical Perspective," IEEE J. Select. Areas Commun. vol. SAC-1, pp. 356 - 372, April, 1983.

2. Henry, Paul S., "Lightwave Primer," IEEE J. Quantum Electronics, vol. QE-21, no. 12, pp. 1862 - 1879, December, 1985.

3. MacDonald, R. I., "Frequency-domain Optical Reflectometer," Applied Optics, vol. 20, no. 10, pp. 1840 - 1344, 1981.

4. Barnoski, M. K., and Jensen, S. M., "Fiber Waveguides: A Novel Technique for Investigating Attenuation Characteristics," Applied Optics, vol. 15, no. 9, pp. 2112 - 2115, 1976.

5. Personick, S. D., "Photon Probe – An Optical-Fiber Time-Domain Reflectometer," Bell Syst. Tech. J., vol. 56, no. 3, pp. 355 - 366, 1977.

6. Healy, Peter, "Review of Long Wavelength Single-Mode Optical Fiber Reflectometry Techniques," IEEE J. Lightwave Technology, vol. LT-3, no. 4, pp. 876 - 886, August, 1985.

7. Okada, K., Hashimoto, K., Shibata, T. and Nagaki, Y., "Optical Cable Fault Location Using Correlation Technique," Electronics Letters, vol. 16, pp. 629 - 630, July, 1980.

8. Carratt, Michel, Le Blevennec, Gilles, Bernard, Jean-Jacques and Biet, Michel, "Réflectomètre à correlation pour fibre monomode à 1,3 micron," Opto 84, Fourth Optoelectronic Meeting, Paris, France, pp. 124 - 125, May, 1984.

9. Bernard, Jean-Jacques and Depresles, Emmanuel, "High-Resolution Correlation OTDR for Distributed Fiber-Optic Sensors and Mobile Cabling," Fiber and Integrated Optic, vol. 7, pp. 79 - 84, 1988.

10. Everard, J. K. A., "Novel Signal Processing Techniques for Enhanced OTDR Sensors," Proceedings of the SPIE, vol. 798, pp. 24 - 26, 1987.

11. Nazarathy, M., Newton, S. A., Fiffard, R. P., Moberly, D. S., Sischka, F. Trutna, W. R., Jr. and Foster, S., "Real-Time Long Range Complementary Correlation Optical Time Domain Reflectometer," IEEE J. Lightwave Technology, vol. 7, no. 1, pp. 24 - 37, January, 1989.

12. Jones, Jr., William B., **Introduction to Optical Fiber Communication Systems** (New York: Holt, Rinehart and Winston, Inc., 1988) p. 111 - 112.

13. Ripamonti, G., Ghioni, M. and Lacaita, A., "No Dead-Space Optical Time-Domain Reflectometer," IEEE J. Lightwave Technology, vol. 8, no. 9, pp. 1278 - 1283, 1990.

14. Marcuse, D., "Curvature Loss Formula for Optical Fibres," J. Opt. Soc. Am., vol. 66, no. 3, pp. 216 - 220, March 1976.

15. Loke, M. Y. and McMullin, J. N., "Development of a Multimode Fibre-Optic Tapping Device," Canadian Conference on Electrical and Computer Engineering, Montreal, vol. I, pp. 564 - 567, September, 1989.

16. Loke, M. Y. and McMullin, J. N., "Simulation and Measurement of Radiation Loss at Multimode Fiber Macrobends," J. Lightwave Technology, vol. 8, no. 8, pp. 1250 - 1256, August, 1990.

17. Renner, H., "Bending Losses of Coated Single-Mode Fibers: A Simple Approach," J. Lightwave Technology, vol. 10, no. 5, pp. 544 - 551, May, 1992.

18. Shimizu, M., Takashima, S. and Kobayashi, H., "Identification System for Optical Fiber Transmission Operation Lines with Local-Light Injection and Detection Coupling System," J. Lightwave Technology, vol. 10, no. 5, pp. 686 - 692, May, 1992.

19. James, S. M., "Non-Intrusive Optical Fibre Identification Using a High-Efficiency Macrobending 'Clip-On' Optical Component," Electronics Letters, vol. 24, no. 19, 15 September, 1988.

20. Jackson, J. D., **Classical Electrodynamics**, 2nd ed., (New York: John Wiley & Sons, 1975) pp. 411 - 427.

21. Brinkmeyer, E., "Analysis of the Backscattering Method for Single-Mode Optical Fibers," J. Opt. Soc. Am., vol. 70, pp. 1010 - 1012, 1980.

22. Philen, D. L., White, I. A., Kuhl, J. F. and Mettle, S. C., "Single-Mode Fiber OTDR: Experiment and Theory," IEEE Trans. Microwave Theory and Techniques, vol. MTT-30, no. 10, October, 1982.

23. Verdeyen, J. T., **Laser Electronics, 2nd ed.** (Englewood Cliffs, NJ: Prentice Hall, 1989) Chapter 4.

24. Brinkmeyer, E. and E.-G. Neumeann, "comments on 'Single-Mode Fiber OTDR: Experiment and Theory,' IEEE J. Quantum Elect., vol. QE-20, no. 11, November, 1984.

25. Jackson, L. B., **Digital Filters and Signal Processing, 2nd ed.** (Boston: Kluwer Academic Publishers, 1989) Chapter 11, pp. 297 - 342.

26. Sischka, F., Newton, S. A. and Nazarathy, M., "Complementary Correlation Optical Time-Domain Reflectometry," Hewlett-Packard Journal, December, 1988, pp. 14 - 21.

27. Freund, J. E. and Walpole, R. E., **Mathematical Statistics, 4th ed.** (Englewood Cliffs, NJ: Prentice-Hall, 1987.

28. Shimizu, M., Takashima, S. and Kobayashi, H., "Identification System for Optical Fiber Transmission Operation Lines with Local-light Injection and Detection Coupling System," J. Lightwave Technology, vol. 10, no. 5, May, 1992, pp. 686-692.

29. Vassallo, C., "Scalar-Field Theory and 2-D Ray Theory for Bent Single-Mode Weakly Guiding Optical Fibers," J. Lightwave Technology, vol. LT-3, no. 2, April, 1985, pp. 416 - 423.

30. J. A. Aberson and I. A. White, "Low-Stress high-Efficiency Local-Power Injection into Single-Mode Fibers," Internation Wire & Cable Symposium Proceedings, 1986.

31. Meyer, R. G. and Blauschild, R. A., A Wide-Band Low-Noise Monolithic Transimpedance Amplifier, IEEE J. Solid-State Circuits, vol. SC-21, no. 4, August, 1986, pp. 530 - 533.

32. Sedra, S. and Smith, K. C., **Microelectronic Circuits**, 2nd ed. (Philadelphia: Saunders College Publishing, 1991), sections 7.5 & 7.6, pp. 520 – 530.

33. Gray, P. R. and Meyer, R. G., **Analyses and Design of Analog Integrated Circuits**, 2nd ed. (New York: John Wiley & Sons, 1984) Chapter 1.

34. Greer, M., "Multi-Stage Amplifier Bandwidth," RF Design, March, 1991, pp. 34 - 40.

Appendices

Contents

A. Derivation of the correction factor for Rayleigh scattering capture ratio in a large-core fibre

B. Expanded block diagrams of simulation subsystems

C. Ray matrices used as building blocks in this thesis

D. GRIN lens data

E. Photo-detector specifications

F. Amplifier specifications

G. Circuit design documentation

A Derivation of the correction factor for Rayleigh scattering capture ratio in a large-core fibre

A scattering site may be viewed as a region having a different dielectric constant and/or magnetic permeability. To make matters simple, we will assume spherical regions of non-uniformity. With our earlier assumption of uniform incident power distribution, the problem can be treated as the scattering of a wave by a non-conductive sphere. Approximating with a dipole, the differential scattering cross-section, integrated over polarisation, is proportional to $(1 + \cos^2\theta)$, where θ is the polar angle measured from the direction of propagation. The power radiated into a region $\theta \in [\theta_1, \theta_2]$ is then proportional to the integral

$$P \propto \int_{\theta_1}^{\theta_2} (1 - (\cos\theta)^2) \sin\theta d\theta = -\left(\cos\theta + \frac{1}{3}(\cos\theta)^3\right)\Big|_{\theta_1}^{\theta_2} \qquad \text{(Eq. A•1)}$$

Applying this to the geometry shown in Figure 2·5 on page 13, we have

$$c_R = \frac{\left(\cos\theta + \frac{1}{3}(\cos\theta)^3\right)\Big|_{0.5\pi+\theta_c}^{\pi}}{\left(\cos\theta + \frac{1}{3}(\cos\theta)^3\right)\Big|_{0.5\pi-\theta_c}^{\pi}} = \frac{\frac{4}{3} - \left(\sin\theta_c + \frac{1}{3}(\sin\theta_c)^3\right)}{\frac{4}{3} + \left(\sin\theta_c + \frac{1}{3}(\sin\theta_c)^3\right)} \qquad \text{(Eq. A•2)}$$

Substitute $\sin\theta_c = n_2/n_1$, then manipulate, we have

$$c_R = \frac{4n_1^3 - 3n_1^2 n_2 - n_2^3}{4n_1^3 + 3n_1^2 n_2 + n_2^3} = \frac{3n_1^3 + 3n_1^2 n_2 + (n_1^3 - n_2^3)}{4n_1^3 + 3n_1^2 n_2 + n_2^3}. \qquad \text{(Eq. A•3)}$$

We now use a physical argument: that (n_2/n_1) is close to unity. In communication fibres, this ratio is typically about 0.995 or larger.

$$c_R \cong \frac{3n_1^2(n_1 - n_2) + (n_1 - n_2)(n_1^2 + n_2^2 + n_1 n_2)}{8n_2^3}, \qquad \text{(Eq. A•4)}$$

$$c_R \approx \frac{3(n_1 - n_2)}{8n_2} + \frac{(n_1 - n_2) \cdot 3n_2^2}{8n_2^3}, \qquad \text{(Eq. A•5)}$$

$$c_R \approx \frac{3}{4} \cdot \frac{n_1 - n_2}{n_2} = \frac{3}{4}\Delta. \qquad \text{(Eq. A•6)}$$

The treatment presented above is a hybrid, similar to that presented by [21] but simplified. We arrived at the angular distribution of the scattered power by wave theories and then used geometric optics to calculate the captured power. We have also assumed that the probability of a photon's being captured is constant across the fibre core, a limiting case in which the core is very wide. The only justification is practicality. (See the main text for further explanation.)

B Expanded block diagrams of simulation subsystems

All subsystems except "Multi-stage Backscatter" are contained in this appendix. Blocks not expanded are basic building blocks performing basic functions that should be obvious from the names.

B.1 Pulse generator

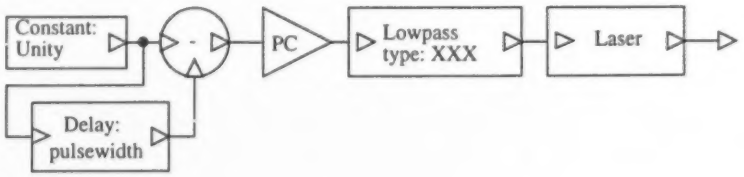

Variables:

1. pulsewidth, specified in numbers of simulation time-steps (DT's)
2. pulse bandwidth, the bandwidth of the lowpass filter
3. PC, peak current of the electrical pulse
4. XXX, Butterworth, Bessel or Chebychev
5. ripple height (Chebychev only)

B.2 Laser

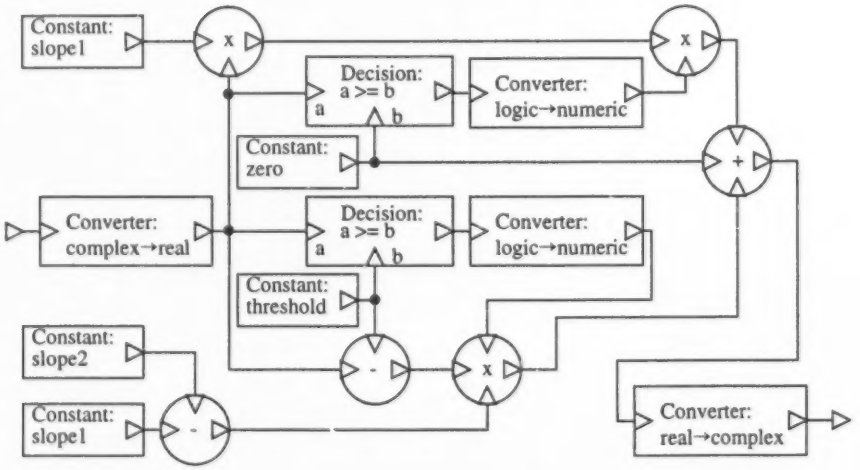

Variables:

1. threshold, threshold current of the laser diode
2. slope1, slope of the L-I curve in the spontaneous emission region
3. slope2, slope of the L-I curve in the stimulated emission region

This block imitates a laser diode's light-current curve by two straight lines meeting at the threshold current, I_{th}.

$$Power = \begin{cases} slope1 \times I, & (0 \le I \le I_{th}) \\ (slope2 - slope1) \times (I - I_{th}) + slope1 \times I_{th}, & (I \ge I_{th}) \end{cases} \quad \text{(Eq. B•1)}$$

B.3 White Noise

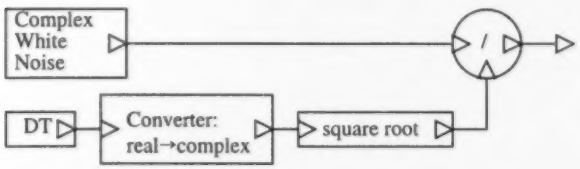

Variables:

1. variance, mean-square value of the random output from "Complex White Noise," equals the power within the simulation bandwidth
2. DT, simulation time step, a system variable, specified at the initiation of a simulation
3. real seed, real part of the seed for the random number generator
4. imaginary seed, imaginary part of the seed for random number generation

Other that DT, all variables are associated with the building block "Complex White Nose." The variance is the square of the noise equivalent power, since we wanted the block output to be the optical equivalent of the noise current. When exported, the variance is called noise equivalent power of the amplifier.

B.4 Fiber

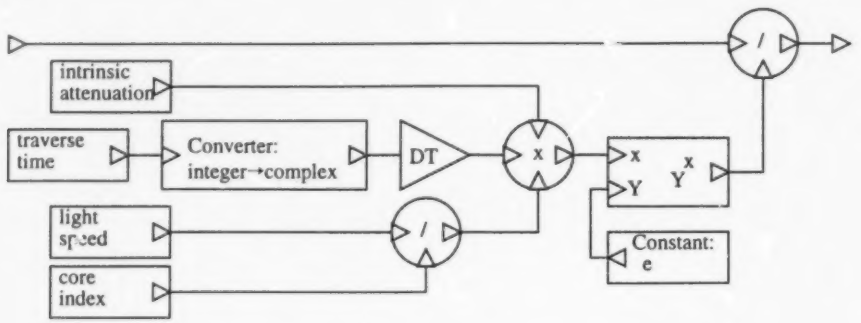

Variables:

1. intrinsic attenuation, the constant, α_i, in Eq. 2·3, i.e. *not* in decibels
2. traverse time, total time the light spent in the piece of fibre, specified in number of simulation time steps (DT's)
3. light speed, 2.99×10^8 metres per second
4. core index, group refractive index of the core material

This block implements the basic attenuation of a piece of fibre according to

$$p_{out} = p_{in} / e^{(\alpha_i c \tau) / n_{core}}, \qquad \text{(Eq. B•2)}$$

where c is the speed of light and τ is the traverse time.

C Ray matrices used as building blocks in this thesis

Ray matrices are derived with the assumptions that

1. all rays are co-planar with the optic axis,
2. the angle made by the rays w.r.t. the optic axis is small and
3. all components are azimuthally symmetric.

The first and third conditions lead to the elimination of azimuthal dependence.

The second condition leads to the small angle approximation:

$$\begin{aligned} \tan\theta &\approx \theta \\ \sin\theta &\approx \theta \end{aligned} \quad \text{(Eq. C•1)}$$

Example:

At an interface between two media with refractive indexes of n_1 and n_2,

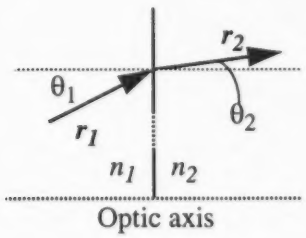

$$r_2 = r_1, \text{ and} \quad \text{(Eq. C•2)}$$

$$\sin\theta_2 = \frac{n_1}{n_2}\sin\theta_1, \quad \text{(Eq. C•3)}$$

$$\theta_2 \approx \frac{n_1}{n_2}\theta_1. \quad \text{(Eq. C•4)}$$

$$\begin{bmatrix} r_2 \\ \theta_2 \end{bmatrix} = \begin{bmatrix} 1 & 0 \\ 0 & \frac{n_1}{n_2} \end{bmatrix} \begin{bmatrix} r_1 \\ \theta_1 \end{bmatrix} \quad \text{(Eq. C•5)}$$

$$\boldsymbol{r}_2 = \boldsymbol{M}_i \boldsymbol{r}_1. \quad \text{(Eq. C•6)}$$

C.1 Basic Ray Matrices

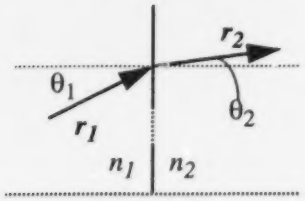

At an interface:

$$M_i = \begin{bmatrix} 1 & 0 \\ 0 & \frac{n_1}{n_2} \end{bmatrix}. \qquad \text{(Eq. C•7)}$$

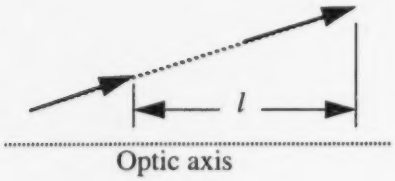

Translation through isotropic space:

$$M_t = \begin{bmatrix} 1 & l \\ 0 & 1 \end{bmatrix} \qquad \text{(Eq. C•8)}$$

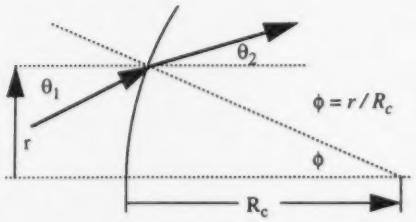

At a spherical interface:

$$M_{si} = \begin{bmatrix} 1 & 0 \\ \frac{1}{R_c}\left(\frac{n_1}{n_2} - 1\right) & \frac{n_1}{n_2} \end{bmatrix} \qquad \text{(Eq. C•9)}$$

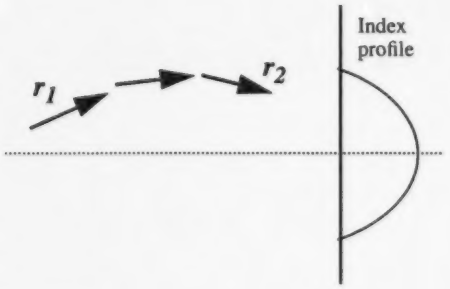

Translation through quadratic graded-index media: $n = n_0(1 - r^2/(2a^2))$.

$$M_{gi} = \begin{bmatrix} \cos\left(\frac{z}{a}\right) & a\sin\left(\frac{z}{a}\right) \\ -\frac{1}{a}\sin\left(\frac{z}{a}\right) & \cos\left(\frac{z}{a}\right) \end{bmatrix} \qquad \text{(Eq. C•10)}$$

C.2 Graded-index lens with curved entry and exit surfaces.

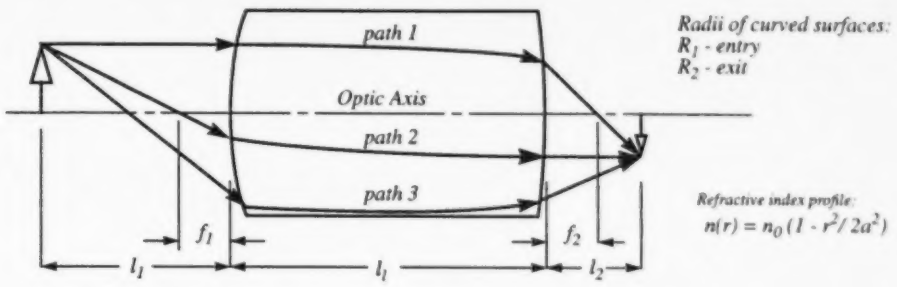

(Fig. 3•12) Rays in a GRIN lens and nomenclature.

The matrix:

$$M_{gl} = M_{si}(R_2)\, M_{gi} M_{si}(R_1) = \begin{bmatrix} A_{gl} & B_{gl} \\ C_{gl} & D_{gl} \end{bmatrix}, \qquad \textbf{(Eq. C•11)}$$

where

$$A_{gl} = \cos\left(\frac{l_l}{a}\right) - \frac{aQ_1}{n_0}\sin\left(\frac{l_l}{a}\right), \qquad \textbf{(Eq. C•12)}$$

$$B_{gl} = \frac{a}{n_0}\sin\left(\frac{l_l}{a}\right), \qquad \textbf{(Eq. C•13)}$$

$$C_{gl} = \left(-\frac{n_0}{a}\right)\sin\left(\frac{l_l}{a}\right) - (Q_1 - Q_2)\cos\left(\frac{l_l}{a}\right) + \frac{Q_1 Q_2 a}{n_0}\sin\left(\frac{l_l}{a}\right) \qquad \textbf{(Eq. C•14)}$$

$$D_{gl} = \cos\left(\frac{l_l}{a}\right) - aQ_2\sin\left(\frac{l_l}{a}\right), \qquad \textbf{(Eq. C•15)}$$

where the Q's are shape factors of the corresponding surfaces:

$$Q_j = \frac{n_0 - 1}{R_j}, \quad j = 1, 2. \qquad \textbf{(Eq. C•16)}$$

Acceptance angle:

The acceptance angle is found by forcing a ray to follow path 3, grazing the skin of the lens at some z-position. Let a ray originate at a distance of l_1, enter at a position r_i with an angle θ_a. Suppose one can monitor a ray's progress through the lens and create a flat exit surface at the z-position where the ray is grazing the skin of the lens. At this arbitrary z-position, the ray is described by:

$$\begin{bmatrix} r(z) \\ \theta(z) \end{bmatrix} = \boldsymbol{M}_{gl}(z) \begin{bmatrix} r_i \\ \theta_a \end{bmatrix} = \begin{bmatrix} r_l \\ 0 \end{bmatrix}, \qquad \textbf{(Eq. C•17)}$$

where r_l is the radius of the lens. With R_2 at infinity (flat exit surface) and knowing that the determinant of any ray matrix is unity (for systems starting and terminating in media with the same refractive index), one can solve for r_i and θ_i:

$$r_i = \frac{r_l D_{gl}}{|M_{gl}|} = r_l \cos\left(\frac{z}{a}\right), \qquad \textbf{(Eq. C•18)}$$

$$\theta_a = \frac{r_l C_{gl}}{|M_{gl}|} = r_l \left[\left(-\frac{n_0}{a}\right)\sin\left(\frac{z}{a}\right) - Q_1 \cos\left(\frac{z}{a}\right)\right]. \qquad \textbf{(Eq. C•19)}$$

Substituting Eq. C·18 into Eq. C·19 with $\cos^2 x + \sin^2 x = 1$,

$$\theta_a = Q_1 r_i + \frac{r_l n_0}{a}\sqrt{1 - \left(\frac{r_i}{r_l}\right)^2}. \qquad \textbf{(Eq. C•20)}$$

This is the (single-sided) acceptance angle of the lens. Substituting $r_i \approx l_1 \theta_a$ into Eq. C·20, one obtains a quadratic equation from which the acceptance angle is deduced as a function of the object location, l_1:

$$\theta_a = \left[1 + Q_1 {l_1}^2 \frac{a}{n_0}^2 + l_1^2\right]^{-1/2}. \qquad \textbf{(Eq. C•21)}$$

D GRIN lens data

The following are specifications on Selfoc graded-index lenses supplied by the manufacturer.

Table 2 Specifications on GRIN lenses

Attributes	*PCW*[19]	*PCH*[20]
Diameter	1.8 mm	1.8 mm
Radius of surface curvature	2 mm	2 mm
Tolerance of above radius	0.1 mm	0.1 mm
Numerical aperture	0.46	0.60
Length	4.73 mm	3.71 mm

Wavelength-dependent parameters (wavelengths in microns):

PCH-1.8 family

$$n_0 = 1.6294 + \frac{1.12 \times 10^{-2}}{\lambda^2}, \qquad \textbf{(Eq. D•1)}$$

$$\frac{1}{a} = 0.4151 + \frac{4.137 \times 10^{-3}}{\lambda^2} + \frac{7.652 \times 10^{-4}}{\lambda^4}, [\mathrm{mm}^{-1}]. \qquad \textbf{(Eq. D•2)}$$

PCW-1.8 family

$$n_0 = 1.5868 + \frac{8.14 \times 10^{-3}}{\lambda^2}, \qquad \textbf{(Eq. D•3)}$$

$$\frac{1}{a} = 0.3238 + \frac{5.364 \times 10^{-3}}{\lambda^2} + \frac{2.626 \times 10^{-4}}{\lambda^4}, [\mathrm{mm}^{-1}]. \qquad \textbf{(Eq. D•4)}$$

19. The full part number is PCW-1.8-0.25-B2-0.83.
20. The full part number is PCH-1.8-0.22-B2-0.83.

E Photo-detector specifications

E.1 NEC NDL2208

Source: NEC data book: Optical Semiconductor Devices, 1991.

Table 3 Specifications of NDL2208 silicon p-i-n photo-diode under 10V reverse bias.

Attributes	*Conditions*	*min.*	*typical*	*max.*	*units*
Dark current				1.0	nA
Detector size	diameter		880		µm
Terminal capacitance	$f = 1$ MHz		1.5	3.0	pF
Quantum efficiency	$\lambda = 850$ nm	70	85		%
Responsivity	$\lambda = 850$ nm	0.48	0.58		A/W

The following graphs show its quantum efficiency as a function of wavelength and its terminal capactiance as a function of bias voltage.

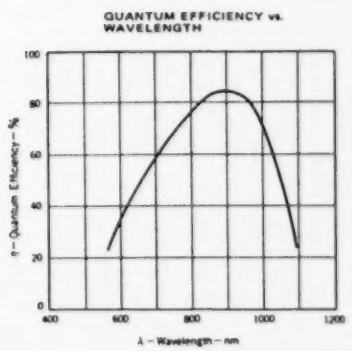

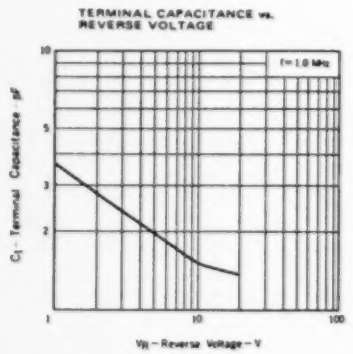

E.2 Epitaxx ETX 500T

Source: Epitaxx data book, 1991

Table 4 Specifications of C30619E p-i-n InGaAs photo-diode under 5V reverse bias

Attributes	*conditions*	*min.*	*typical*	*max.*	*units*
Detector size	active diameter		0.5		mm
Dark current			12	100	nA
Dynamic impedance	V_R = 10 mV	5.0	100		MΩ
Capacitance	no bias		40	50	pF
Responsivity	λ = 850 nm	0.10	0.20		A/W
	λ = 1300 nm	0.80	0.90		A/W
	λ = 1550 nm		0.95		A/W

The following graphs show the detectors' responsivity as a function of wavelength and capacitance as a function of reverse bias voltage.

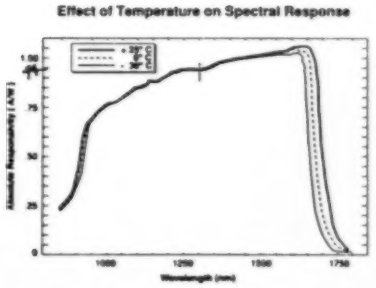

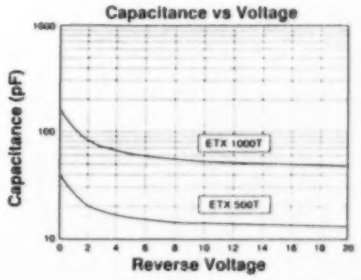

E.3 EG&G C30619

Source: data supplied by EG&G Canada Ltd.

Table 5 Specifications of C30619E p-i-n InGaAs photo-diode under 5V reverse bias

Attributes	*conditions*	*min.*	*typical*	*max.*	*units*
Detector size	active diameter		0.5		mm
Dark current			5	20	nA
Noise current	f = 10 kHz		0.1	0.5	pA/Hz$^{1/2}$
Dynamic impedance		5.0			MΩ
Capacitance			8	10	pF
	no bias		20	25	pF
Responsivity	λ = 1300 nm	0.78	0.84		A/W
	λ = 1550 nm	0.70	0.80		A/W

E.4 Detector packages

TO-18

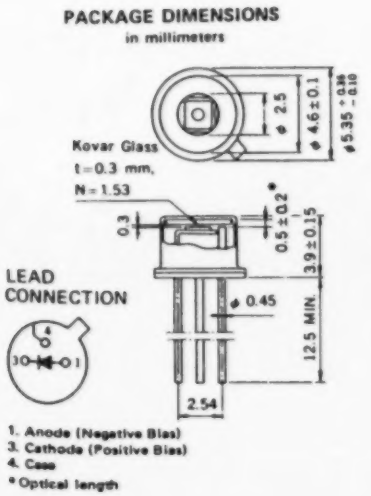

ETX500T

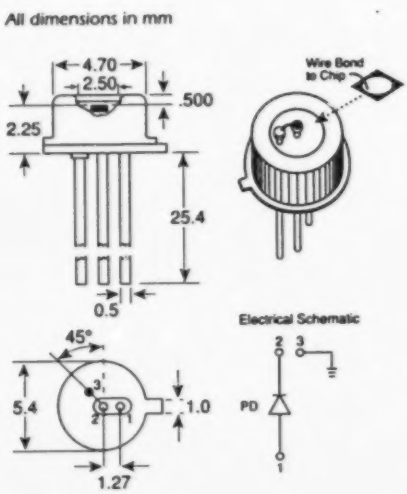

F Amplifiers specifications

F.1 Transistors

F.1.1 Motorola MMBR931L

MAXIMUM RATINGS

Rating	Symbol	Value	Unit
Collector-Emitter Voltage	V_{CEO}	5.0	Vdc
Collector-Base Voltage	V_{CBO}	10	Vdc
Emitter-Base Voltage	V_{EBO}	2.0	Vdc
Collector Current — Continuous	I_C	5.0	mAdc
Operating and Storage Junction Temperature Range	T_J, T_{stg}	−55 to +150	°C

THERMAL CHARACTERISTICS

Characteristic	Symbol	Max	Unit
*Total Device Dissipation, T_A = 25°C Derate above 25°C	P_D	50 0.4	mW mW/°C
Storage Temperature	T_{stg}	150	°C
*Thermal Resistance Junction to Ambient	$R_{\theta JA}$	2500	°C/W

*Package mounted on 99.5% alumina 10 x 8 x 0.6 mm.

CASE 318-07, STYLE 6
SOT-23
LOW PROFILE
(TO-236AA/AB)

DEVICE MARKING

MMBR931L = 7D

ELECTRICAL CHARACTERISTICS (T_A = 25°C unless otherwise noted.)

Characteristic	Symbol	Min	Typ	Max	Unit
OFF CHARACTERISTICS					
Collector-Emitter Breakdown Voltage (I_C = 0.1 mAdc, I_B = 0)	$V_{(BR)CEO}$	5.0	—	—	Vdc
Collector-Base Breakdown Voltage (I_C = 0.01 mAdc, I_E = 0)	$V_{(BR)CBO}$	10	—	—	Vdc
Emitter-Base Breakdown Voltage (I_E = 0.1 mAdc, I_C = 0)	$V_{(BR)EBO}$	2.0	—	—	Vdc
Collector Cutoff Current (V_{CB} = 5.0 Vdc, I_E = 0)	I_{CBO}	—	—	50	nAdc
ON CHARACTERISTICS					
DC Current Gain (I_C = 0.25 mAdc, V_{CE} = 1.0 Vdc)	h_{FE}	30	—	150	—
SMALL-SIGNAL CHARACTERISTICS					
Collector-Base Capacitance (V_{CB} = 1.0 Vdc, I_E = 0, f = 1.0 MHz)	C_{cb}	—	—	0.5	pF
Noise Figure (I_E = 0.25 mAdc, V_{CE} = 1.0 Vdc, f = 1.0 GHz)	NF	—	4.3	—	dB
Power Gain at Optimum Noise Figure (I_E = 0.25 mAdc, V_{CE} = 1.0 Vdc, f = 1.0 GHz)	G_{NF}	—	10	—	—

F.1.2 Motorola MRF9331L

MAXIMUM RATINGS

Rating	Symbol	Value	Unit
Collector-Emitter Voltage	V_{CEO}	8	Vdc
Collector-Base Voltage	V_{CBO}	15	Vdc
Emitter-Base Voltage	V_{EBO}	2	Vdc
Collector-Current — Continuous	I_C	2	mAdc
Total Device Dissipation @ T_C = 100°C Derate above 100°C	P_D	50 1	mW mW/°C
Storage Temperature Range	T_{stg}	−65 to +150	°C

THERMAL CHARACTERISTICS

Characteristic	Symbol	Max	Unit
Thermal Resistance, Junction to Ambient	$R_{\theta JA}$	500	°C/W

DEVICE MARKING

MRF9331,L = 05

ELECTRICAL CHARACTERISTICS (T_C = 25°C unless otherwise noted)

Characteristic	Symbol	Min	Typ	Max	Unit
OFF CHARACTERISTICS					
Collector-Emitter Breakdown Voltagr (I_C = 0.1 mAdc, I_B = 0)	$V_{(BR)CEO}$	8	—	—	Vdc
Collector-Base Breakdown Voltage (I_C = 0.01 mAdc, I_E = 0)	$V_{(BR)CBO}$	15	—	—	Vdc
Emitter-Base Leakage Current (V_{EB} = 2 Vdc, I_C = 0)	I_{EBO}	—	—	0.1	mAdc
Collector Cutoff Current (V_{CB} = 5 Vdc, I_E = 0)	I_{CBO}	—	—	50	nAdc
ON CHARACTERISTICS					
DC Current Gain (I_C = 0.5 mAdc, V_{CE} = 1 Vdc)	h_{FE}	30	80	200	—

Characteristic		Symbol	Min	Typ	Max	Unit
DYNAMIC CHARACTERISTICS						
Current-Gain-Bandwidth Product (I_C = 1 mAdc, V_{CE} = 1 Vdc, f = 1 GHz)	Figure 2	f_T	3.5	5	—	GHz
Collector-Base Capacitance (V_{CB} = 1 Vdc, I_E = 0, f = 1 MHz)	Figure 1	C_{cb}	—	0.21	0.3	pF
FUNCTIONAL TESTS						
Power Gain at Minimum Noise Figure (V_{CE} = 1 Vdc, I_C = 0.5 mA, f = 1 GHz)	Figure 5, 3	G_{NFmin}	—	12.5	—	dB
Noise Figure (V_{CE} = 1 Vdc, I_C = 0.5 mA, f = 1 GHz)	Figure 5, 3	NF_{min}	—	2.5	—	dB

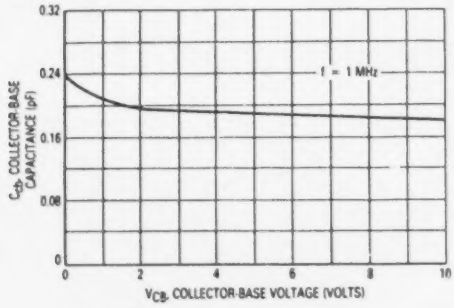

Figure 1. Collector-Base Capacitance versus Collector-Base Voltage

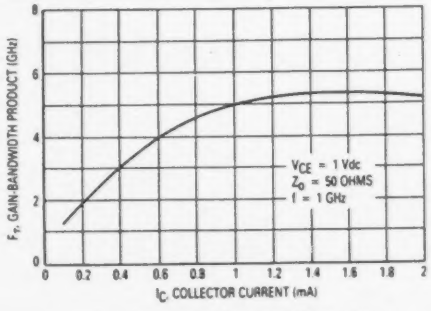

Figure 2. Current Gain-Bandwidth Product versus Collector Current

F.1.3 Motorola BFR90

The RF Line

NPN SILICON HIGH FREQUENCY TRANSISTOR

. . . designed primarily for use in high-gain, low-noise, small-signal amplifiers. Also used in applications requiring fast switching times.

- High Current-Gain – Bandwidth Product –
  f_T = 5.0 GHz (Typ) @ I_C = 14 mA
- Low Noise Figure –
  NF = 2.4 dB (Typ) @ f = 0.5 GHz
  = 3.0 dB (Typ) @ f = 1.0 GHz
- High Power Gain –
  G_{max} = 18 dB (Typ) @ f = 0.5 GHz
  = 12 dB (Typ) @ f = 1.0 GHz

f_T = 5.0 GHz @ 14 mA

HIGH FREQUENCY TRANSISTOR

NPN SILICON

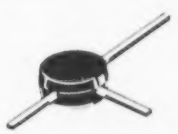

MAXIMUM RATINGS

Rating	Symbol	Value	Unit
Collector-Emitter Voltage	V_{CEO}	15	Vdc
Collector-Base Voltage	V_{CBO}	20	Vdc
Emitter-Base Voltage	V_{EBO}	3.0	Vdc
Collector Current – Continuous	I_C	30	mAdc
Total Device Dissipation @ T_A = 60°C	P_D	180	mW
Derate Above 60°C		2.0	mW/°C
Storage Temperature Range	T_{stg}	-65 to +150	°C

THERMAL CHARACTERISTICS

Characteristic	Symbol	Max	Unit
Thermal Resistance Junction to Ambient	$R_{\theta JA}$	500	°C/W

FIGURE 1 – POWER DERATING

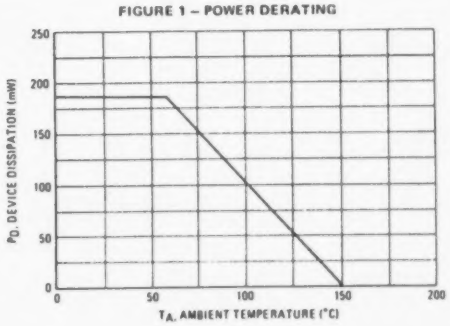

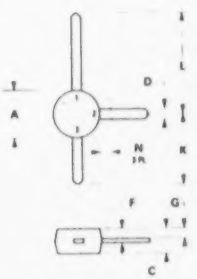

STYLE 2
PIN 1 COLLECTOR
2 EMITTER
3 BASE

NOTE
DIMENSION D NOT APPLICABLE IN ZONE N

DIM	MILLIMETERS MIN	MILLIMETERS MAX	INCHES MIN	INCHES MAX
A	4.44	5.21	0.175	0.205
C	1.90	2.54	0.075	0.100
D	0.84	0.99	0.033	0.039
F	0.20	0.30	0.008	0.012
G	0.76	1.14	0.030	0.045
K	7.24	8.13	0.285	0.320
L	10.54	11.43	0.415	0.450
N	–	1.65	–	0.065

CASE 317A-01

BFR90 (cont'd)

ELECTRICAL CHARACTERISTICS (T_C = 25°C unless otherwise noted)

Characteristic	Symbol	Min	Typ	Max	Unit
OFF CHARACTERISTICS					
Collector-Emitter Breakdown Voltage (I_C = 1.0 mAdc, I_B = 0)	$V_{(BR)CEO}$	15	–	–	Vdc
Collector-Base Breakdown Voltage (I_C = 0.1 mAdc, I_E = 0)	$V_{(BR)CBO}$	20	–	–	Vdc
Emitter-Base Breakdown Voltage (I_E = 0.1 mAdc, I_C = 0)	$V_{(BR)EBO}$	3.0	–	–	Vdc
Collector Cutoff Current (V_{CB} = 10 Vdc, I_E = 0)	I_{CBO}	–	–	50	nAdc
ON CHARACTERISTICS					
DC Current Gain (I_C = 14 mAdc, V_{CE} = 10 Vdc)	h_{FE}	25	–	250	–
DYNAMIC CHARACTERTISTICS					
Current-Gain Bandwidth Product (I_C = 14 mAdc, V_{CE} = 10 Vdc, f = 0.5 GHz)	f_T	–	5.0	–	GHz
Collector-Base Capacitance (V_{CB} = 10 Vdc, I_E = 0, f = 1.0 MHz)	C_{cb}	–	0.5	1.0	pF
FUNCTIONAL TESTS					
Noise Figure	NF				dB
(I_C = 2.0 mAdc, V_{CE} = 10 Vdc, f = 0.5 GHz)		–	2.4	–	
(I_C = 2.0 mAdc, V_{CE} = 10 Vdc, f = 1.0 GHz)		–	3.0	–	
Power Gain at Optimum Noise Figure	G_{NF}				dB
(I_C = 2.0 mAdc, V_{CE} = 10 Vdc, f = 0.5 GHz)		–	15	–	
(I_C = 2.0 mAdc, V_{CE} = 10 Vdc, f = 1.0 GHz)		–	10	–	
Maximum Available Power Gain (1)	G_{max}				dB
(I_C = 14 mAdc, V_{CE} = 10 Vdc, f = 0.5 GHz)		–	18	–	
(I_C = 14 mAdc, V_{CE} = 10 Vdc, f = 1.0 GHz)		–	12	–	

(1) $G_{max} = \frac{|S_{21}|^2}{(1-|S_{11}|^2)(1-|S_{22}|^2)}$

FIGURE 2 – POWER GAIN AND NOISE FIGURE versus FREQUENCY

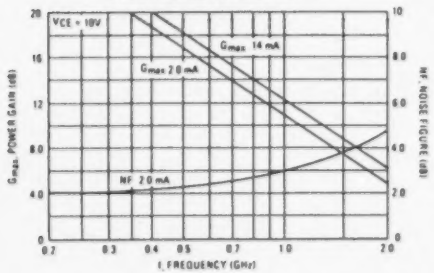

FIGURE 3 – POWER GAIN AND NOISE FIGURE versus COLLECTOR CURRENT

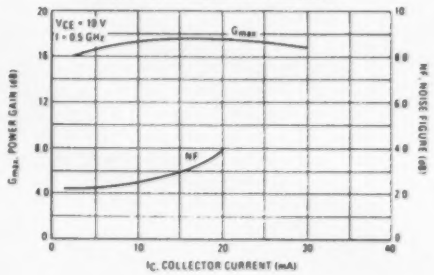

F.1.4 Motorola 2N3866 / 2N3866A

The RF Line

NPN SILICON HIGH FREQUENCY TRANSISTOR

. . . designed for amplifier and oscillator applications in military and industrial equipment. Suitable for use as output, driver or pre-driver stages in VHF and UHF equipment.

- Specified 400 MHz, 28 Vdc Characteristics –
  Output Power = 1.0 Watt
  Minimum Gain = 10 dB
  Efficiency = 45%
- Large Signal Series Equivalent Impedances
- S-Parameter Characterization

1.0 W – 400 MHz
HIGH FREQUENCY TRANSISTOR
NPN SILICON

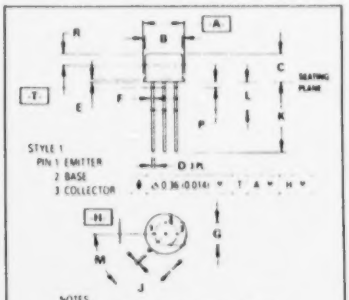

NOTES
1. DIMENSIONING AND TOLERANCING PER ANSI Y14.5M, 1982.
2. CONTROLLING DIMENSION: INCH.
3. DIMENSION J MEASURED FROM DIMENSION A MAXIMUM.
4. DIMENSION B SHALL NOT VARY MORE THAN 0.25 (0.010) IN ZONE R. THIS ZONE CONTROLLED FOR AUTOMATIC HANDLING.
5. DIMENSION F APPLIES BETWEEN DIMENSION P AND L. DIMENSION D APPLIES BETWEEN DIMENSION L AND K. MINIMUM LEAD DIAMETER IS UNCONTROLLED IN DIMENSION P AND BEYOND DIMENSION K MINIMUM.

DIM	MILLIMETERS MIN	MILLIMETERS MAX	INCHES MIN	INCHES MAX
A	8.51	9.39	0.335	0.370
B	7.75	8.50	0.305	0.335
C	6.10	6.60	0.240	0.260
D	0.41	0.53	0.016	0.021
E	0.23	1.04	0.009	0.041
F	0.41	0.48	0.016	0.019
G	5.08 BSC		0.200 BSC	
H	0.72	0.86	0.028	0.034
J	0.74	1.14	0.029	0.045
K	12.70	19.05	0.500	0.750
L	6.35	—	0.250	—
M	45° BSC		45° BSC	
P	—	1.27	—	0.050
R	2.54	—	0.100	—

CASE 79-04
TO-205AD
(TO-39)

***MAXIMUM RATINGS**

Rating	Symbol	Value	Unit
Collector-Emitter Voltage	V_{CEO}	30	Vdc
Collector-Base Voltage	V_{CBO}	55	Vdc
Emitter-Base Voltage	V_{EBO}	3.5	Vdc
Collector Current – Continuous	I_C	0.4	Adc
Total Device Dissipation @ T_C = 25°C Derate Above 25°C	P_D	5.0 28.6	Watts mW/°C
Storage Temperature Range	T_{stg}	-65 to +200	°C

*Indicates JEDEC Registered Data

2N3866 / 2N3866A (cont'd)

***ELECTRICAL CHARACTERISTICS** (T_C = 25°C unless otherwise noted).

Characteristic		Symbol	Min	Max	Unit
OFF CHARACTERISTICS					
Collector-Emitter Sustaining Voltage (I_C = 5.0 mAdc, I_B = 0)		$V_{CEO(sus)}$	30	—	Vdc
Collector-Base Sustaining Voltage (I_C = 5.0 mAdc, R_{BE} = 10 Ω)		$V_{CER(sus)}$	55	—	Vdc
Emitter-Base Breakdown Voltage (I_E = 100 μAdc, I_C = 0)		$V_{(BR)EBO}$	3.5	—	Vdc
Collector Cutoff Current (V_{CE} = 28 Vdc, I_B = 0)		I_{CEO}	—	0.02	mAdc
Emitter Cutoff Current (V_{BE} = 3.5 Vdc, I_C = 0)		I_{EBO}	—	0.1	mAdc
Collector Cutoff Current (V_{CE} = 30 Vdc, V_{BE} = −1.5 Vdc (Rev.), T_C = 200°C)		I_{CEX}	—	5.0	mAdc
(V_{CE} = 55 Vdc, V_{BE} = −1.5 Vdc (Rev.)			—	0.1	
ON CHARACTERISTICS					
DC Current Gain	Both	h_{FE}	5.0	—	—
(I_C = 360 mAdc, V_{CE} = 5.0 Vdc)	2N3866		10	200	
(I_C = 50 mAdc, V_{CE} = 5.0 Vdc)	2N3866A		25	200	
Collector-Emitter Saturation Voltage (I_C = 100 mAdc, I_B = 20 mAdc)		$V_{CE(sat)}$	—	1.0	Vdc
DYNAMIC CHARACTERISTICS					
Current-Gain — Bandwidth Product (I_C = 50 mAdc, V_{CE} = 15 Vdc, f = 200 MHz)	2N3866	f_T	500	—	MHz
	2N3866A		800	—	
Output Capacitance (V_{CB} = 28 Vdc, I_E = 0, f = 1.0 MHz)		C_{ob}	—	3.0	pF
FUNCTIONAL TESTS					
Common-Emitter Amplifier Power Gain (V_{CC} = 28 Vdc, P_{out} = 1.0 W, f = 400 MHz)		G_{PE}	10	—	dB
Collector Efficiency (V_{CC} = 28 Vdc, P_{out} = 1.0 W, f = 400 MHz)		η	45	—	%

*Indicates JEDEC Registered Data.

FIGURE 1 – 400 MHz TEST CIRCUIT SCHEMATIC

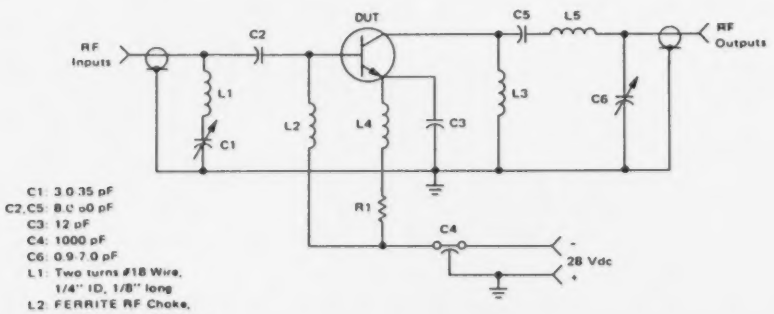

C1: 3.0-35 pF
C2,C5: 8.0-60 pF
C3: 12 pF
C4: 1000 pF
C6: 0.9-7.0 pF
L1: Two turns #18 Wire, 1/4" ID, 1/8" long
L2: FERRITE RF Choke, One Turn, z = 450 Ohms
L3,L4: RF Choke, 0.1 μH
L5: 2 3/4 Turns, #18 Wire, 1/4" ID, 3/16" long
R1: 5.6 Ohms

F.1.5 Plessey SL2365

The SL2365 is an array of transistors internally connected to form a dual long-tail pair with current mirrors whose bases and collectors are connected internally. The ICs are manufactured on a very high speed bipolar process, which has a minimum usable f_T of 2.5GHz (typically 5GHz). The current mirror enables a well defined gain at low current levels to be achieved.

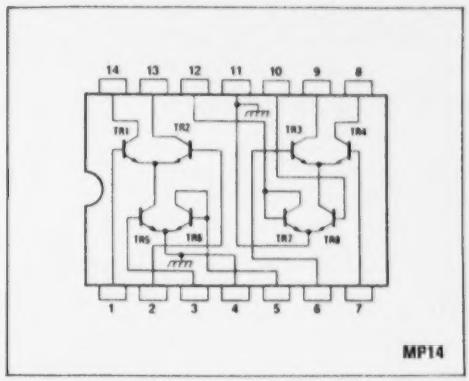

Fig.1 Pin connections - top view

FEATURES

- Complete Dual Long Tailed Pair in One Package
- Very High f_T - Typically 5GHz
- Well Defined Gain at Low Current Levels
- Available in Small Outline Package

ELECTRICAL CHARACTERISTICS

Characteristic	Value			Units	Conditions
	Min.	Typ.	Max.		
BV_{cbo}	10	20		V	I_C = 10μA
LV_{ceo}	6	9		V	I_C = 5mA
BV_{ebo}	2.5	5		V	I_E = 10μA
BV_{cio}	16	40		V	I_C = 10μA
H_{fe}	50	80			I_C = 8mA, V_{ce} = 2V
f_T	2.5	5		GHz	I_C (tail) = 8mA, V_{ce} = 2V
ΔV_{be}		2	5	mV	I_C (tail) = 8mA, V_{ce} = 2V
$\Delta V_{be}/T_{amb}$		-7		mV/°C	I_C (tail) = 8mA, V_{ce} = 2V
C_{CB}		0.5	0.8	pF	V_{CB} = 0V
C_{CI}		1.0	1.5	pF	V_{CI} = 0V

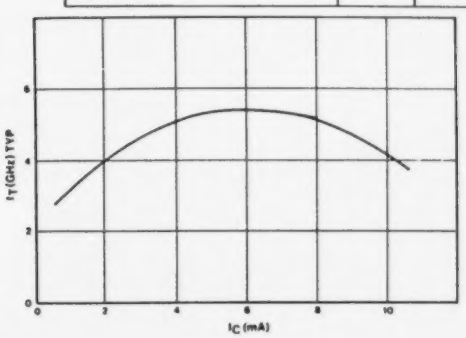

Fig. 2 Collector current

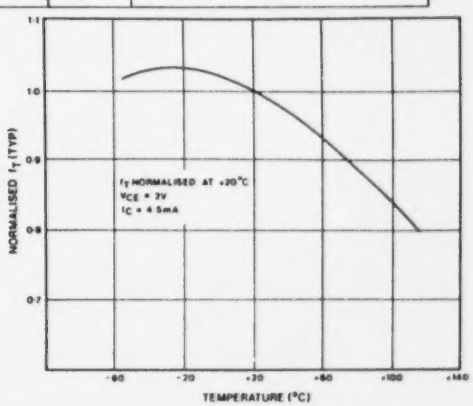

Fig. 3 Chip temperature

ABSOLUTE MAXIMUM RATINGS

Maximum individual transistor dissipation 200mW

Storage temperature −55°C to +150°C
Maximum junction temperature +150°C
Package thermal resistance (°C/W):
Chip to case 65 (CM10)
Chip to ambient 225 (CM10) 175 (DP14)
V_{CBO} = 10V, V_{EBO} = 2.5V, V_{CEO} = 6V, V_{CIO} = 15V. IC (any one transistor) = 20mA

The substrate should be connected to the most negative point of the circuit to maintain electrical isolation between the transistors.

F.1.6 Plessey SL3227

The SL3227 is a monolithic array of the five high frequency low current NPN transistors in a 16 lead DIL package. The transistors exhibit typical f_T of 3GHz and wideband noise figures of 2dB. The SL3227 is pin compatible with the CA3127 and SL3127.

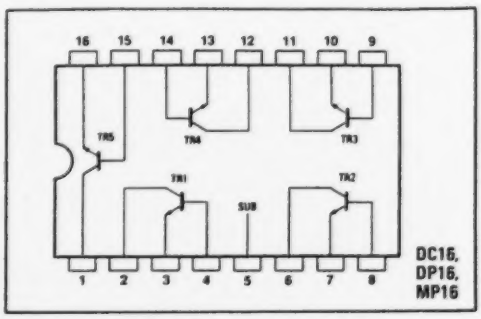

Fig.1 Pin connections - SL3227

FEATURES

- f_T Typically 3GHz
- Wideband Noise Figure 2.0dB
- V_{BE} Matching better than 5mV

APPLICATIONS

- Wide Band Amplifiers
- PCM Regenerators
- High Speed Interface Circuits
- High Performance Instrumentation Amplifiers
- High Speed Modems

ABSOLUTE MAXIMUM RATINGS

The absolute maximum ratings are limiting values above which operating life may be shortened or specified parameters may be degraded.

All Electrical ratings apply to individual transistors. Thermal ratings apply to the total package.

The isolation pin (substrate) must be connected to the most negative voltage applied to the package to maintain electrical isolation.

V_{CB} = 10V
V_{EB} = 2.5V
V_{CE} = 6V
V_{CI} = 15V
I_C = 20mA
Maximum individual transistor dissipation 200mW
Storage temperature -55°C to +150°C
Max. junction temperature +150°C

Package thermal resistance (°C/watt)

Package Type	DC16	DP16	MP16
Chip to Case	40		
Chip to Ambient	120	180	200

NOTE: If all the power is being dissipated in one transistor these thermal resistance figures should be increased by 100° C/watt.

ORDERING INFORMATION

SL3227 DC Ceramic/Metal
SL3227 DP Plastic
SL3227 MP Miniature Plastic

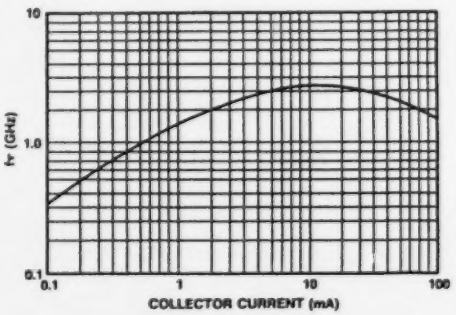

Fig.2 Transition frequency (f_T) v. collector current (V_{CB} = 2V, f = 200MHz)

SL3227 (cont'd)

ELECTRICAL CHARACTERISTICS

Test conditions (unless otherwise stated):
T_{amb} = 22°C ± 2°C

Static Characteristics

Characteristic	Symbol	Value			Units	Conditions
		Min.	Typ.	Max.		
Collector base breakdown	BV_{CBO}	10	20		V	I_C = 10µA
Collector isolation breakdown	BV_{CIO}	16	40		V	I_C = 10µA
Base emitter breakdown	BV_{EBO}	2.5	5.0		V	I_E = 10µA
Collector emitter breakdown	LV_{CEO}	6	9		V	I_C = 5mA
Collector emitter saturation voltage	$V_{CE(SAT)}$		0.22	0.5	V	I_C = 10mA, I_B = 1mA
Base emitter voltage	V_{BE}	0.73	0.78	0.81	V	V_{CE} = 2V, I_C = 1mA
Base emitter voltage difference all transistors	ΔV_{BE}		0.45	5.0	mV	V_{CE} = 2V, I_C = 1mA
Input offset current	ΔI_B		0.2	3	µA	V_{CE} = 2V, I_C = 1mA
Temperature coefficient of V_{BE}	$\frac{\Delta V_{BE}}{T}$		-1.69		mV/°C	V_{CE} = 2V, I_C = 1mA
Static forward current ratio	H_{FE}	35	80			V_{CE} = 2V, I_C = 5mA
		35	95			V_{CE} = 2V, I_C = 0.1mA
		40	85			V_{CE} = 2V, I_C = 1mA
Emitter base leakage	I_{EBO}		15		nA	V_{EB} = 2V
Collector base leakage	I_{CBO}		5		pA	V_{CB} = 10V
Collector isolation leakage	I_{CIO}		5		pA	V_{CI} = 16V
Emitter base capacitance	C_{EB}		0.7		pF	V_{EB} = 0V
Collector base capacitance	C_{CB}		0.4		pF	V_{CI} = 0V
Collector isolation capacitance	C_{CI}		1.5	2.0	pF	V_{CI} = 0V

Dynamic Characteristics

Characteristic	Symbol	Value			Units	Conditions
		Min.	Typ.	Max.		
Transition frequency	f_T		3		GHz	V_{CE} = 2V, I_C = 5mA
Wideband noise figure	NF		2.0		dB	f = 60MHz V_{CC} = 6V
Knee of NF noise curve			1		kHz	I_C = 1mA
						R_S = 1kΩ

F.2 Packaged amplifiers

F.2.1 Motorola MC1733C

DIFFERENTIAL VIDEO AMPLIFIER

. . . a wideband amplifier with differential input and differential output. Gain is fixed at 10, 100, or 400 without external components or, with the addition of one external resistor, gain becomes adjustable from 10 to 400.

- Bandwidth – 120 MHz typical @ A_{vd} = 10
- Rise Time – 2.5 ns typical @ A_{vd} = 10
- Propagation Delay Time – 3.6 ns typical @ A_{vd} = 10

DIFFERENTIAL VIDEO WIDEBAND AMPLIFIER

SILICON MONOLITHIC INTEGRATED CIRCUIT

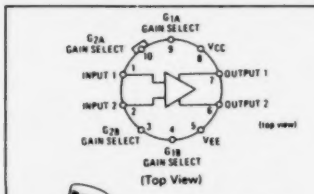

(Top View)

G SUFFIX
METAL PACKAGE
CASE 603

D SUFFIX
PLASTIC PACKAGE
CASE 751A
(SO-14)

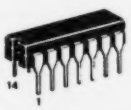

L SUFFIX
CERAMIC PACKAGE
CASE 632

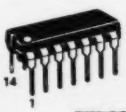

P SUFFIX
PLASTIC PACKAGE
CASE 646

PIN CONNECTIONS

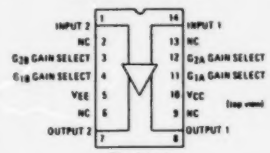

(Top View)

FIGURE 1 – BASIC CIRCUIT

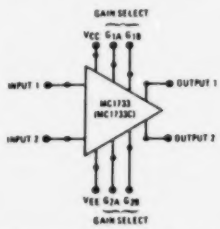

FIGURE 2 – VOLTAGE GAIN ADJUST CIRCUIT

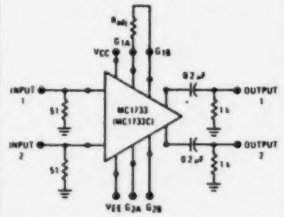

FIGURE 3 – EQUIVALENT CIRCUIT SCHEMATIC

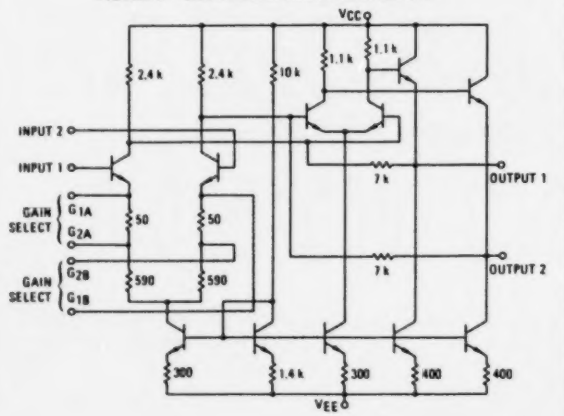

ORDERING INFORMATION

Device	Temperature Range	Package
MC1733G MC1733L	−55°C to +125°C	Metal Can Ceramic DIP
MC1733CD MC1733CG MC1733CL MC1733CP	0°C to +70°C	SO-14 Metal Can Ceramic DIP Plastic DIP

MC1733C (cont'd)

MAXIMUM RATINGS (T_A = +25°C unless otherwise noted)

Rating	Symbol	Value	Unit
Power Supply Voltage	V_{CC} V_{EE}	+8.0 -8.0	Volts
Differential Input Voltage	V_{in}	±5.0	Volts
Common-Mode Input Voltage	V_{ICM}	±6.0	Volts
Output Current	I_O	10	mA
Internal Power Dissipation (Note 1) Metal Can Package Ceramic Dual In-Line Package	P_D	 500 500	mW
Operating Temperature Range MC1733C MC1733	T_A	0 to +70 -55 to +125	°C
Storage Temperature Range	T_{stg}	-65 to +150	°C

ELECTRICAL CHARACTERISTICS (V_{CC} = +6.0 Vdc, V_{EE} = -6.0 Vdc, at T_A = +25°C unless otherwise noted.)

		MC1733			MC1733C			
Characteristic	Symbol	Min	Typ	Max	Min	Typ	Max	Units
Differential Voltage Gain								V/V
Gain 1 (Note 2)	A_{vd}	300	400	500	250	400	600	
Gain 2 (Note 3)		90	100	110	80	100	120	
Gain 3 (Note 4)		9.0	10	11	8.0	10	12	
Bandwidth (R_s = 50 Ω)	BW							MHz
Gain 1		–	40	–	–	40	–	
Gain 2		–	90	–	–	90	–	
Gain 3		–	120	–	–	120	–	
Rise Time (R_s = 50 Ω, V_O = 1 Vp-p)	t_{TLH}							ns
Gain 1	t_{THL}	–	10.5	–	–	10.5	–	
Gain 2		–	4.5	10	–	4.5	12	
Gain 3		–	2.5	–	–	2.5	–	
Propagation Delay (R_s = 50 Ω, V_O = 1 Vp-p)	t_{PLH}							ns
Gain 1	t_{PHL}	–	7.5	–	–	7.5	–	
Gain 2		–	6.0	10	–	6.0	10	
Gain 3		–	3.6	–	–	3.6	–	
Input Resistance	R_{in}							kΩ
Gain 1		–	4.0	–	–	4.0	–	
Gain 2		20	30	–	10	30	–	
Gain 3		–	250	–	–	250	–	
Input Capacitance (Gain 2)	C_{in}	–	2.0	–	–	2.0	–	pF
Input Offset Current (Gain 3)	$\|I_{IO}\|$	–	0.4	3.0	–	0.4	5.0	μA
Input Bias Current (Gain 3)	I_{IB}	–	9.0	20	–	9.0	30	μA
Input Noise Voltage (R_s = 50 Ω, BW = 1 kHz to 10 MHz)	V_n	–	12	–	–	12	–	μV(rms)
Input Voltage Range (Gain 2)	V_{in}	±1.0	–	–	±1.0	–	–	V
Common-Mode Rejection Ratio	CMRR							dB
Gain 2 (V_{CM} = ±1 V, f ≤ 100 kHz)		60	86	–	60	86	–	
Gain 2 (V_{CM} = ±1 V, f = 5 MHz)		–	60	–	–	60	–	
Supply Voltage Rejection Ratio	PSRR							dB
Gain 2 (ΔV_s = ±0.5 V)		50	70	–	50	70	–	
Output Offset Voltage	V_{OO}							V
Gain 1		–	0.6	1.5	–	0.6	1.5	
Gain 2 and Gain 3		–	0.35	1.0	–	0.35	1.5	
Output Common-Mode Voltage (Gain3)	V_{CMO}	2.4	2.9	3.4	2.4	2.9	3.4	V
Output Voltage Swing (Gain 2)	V_O	3.0	4.0	–	3.0	4.0	–	Vp-p
Output Sink Current (Gain 2)	I_O	2.5	3.6	–	2.5	3.6	–	mA
Output Resistance	R_{out}	–	20	–	–	20	–	Ω
Power Supply Current (Gain 2)	I_D	–	18	24	–	18	24	mA

MC1733C (cont'd)

ELECTRICAL CHARACTERISTICS (V_{CC} = +6.0 Vdc, V_{EE} = -6.0 Vdc, at T_A = T_{high} to T_{low} unless otherwise noted.)*

Characteristic	Symbol	MC1733 Min	MC1733 Typ	MC1733 Max	MC1733C Min	MC1733C Typ	MC1733C Max	Units
Differential Voltage Gain	A_{vd}							V/V
Gain 1 (Note 2)		200	–	600	250	–	600	
Gain 2 (Note 3)		80	–	120	80	–	120	
Gain 3 (Note 4)		8.0	–	12	8.0	–	12	
Input Resistance Gain 2	R_{in}	8.0	–	–	8.0	–	–	kΩ
Input Offset Current (Gain 3)	$\|I_{IO}\|$	–	–	5.0	–	–	6.0	μA
Input Bias Current (Gain 3)	I_{IB}	–	–	40	–	–	40	μA
Input Voltage Range (Gain 2)	V_{in}	±1.0	–	–	±1.0	–	–	V
Common-Mode Rejection Ratio Gain 2 (V_{CM} = ±1 V, f ≤ 100 kHz)	CMRR	50	–	–	50	–	–	dB
Supply Voltage Rejection Ratio Gain 2 (ΔV_s = ±0.5 V)	PSRR	50	–	–	50	–	–	dB
Output Offset Voltage	V_{OO}							V
Gain 1		–	–	1.5	–	–	1.5	
Gain 2 and Gain 3		–	–	1.2	–	–	1.5	
Output Voltage Swing (Gain 2)	V_O	2.5	–	–	2.5	–	–	Vp-p
Output Sink Current (Gain 2)	I_O	2.2	–	–	2.5	–	–	mA
Power Supply Current (Gain 2)	I_D	–	–	27	–	–	27	mA

*T_{low} = 0°C for MC1733C, -55°C for MC1733
T_{high} = +70°C for MC1733C, +125°C for MC1733.

NOTES

Note 1: Derate metal package at 6.5 mW/°C for operation at ambient temperatures above 75°C and dual in-line package at 9 mW/°C for operation at ambient temperatures above 100°C (see Figure 4). If operation at high ambient temperatures is required (MC1733) a heatsink may be necessary to limit maximum junction temperature to 150°C. Thermal resistance, junction-to-case, for the metal package is 69.4°C per Watt.
Note 2: Gain Select pins G_{1A} and G_{1B} connected together.
Note 3: Gain Select pins G_{2A} and G_{2B} connected together.
Note 4: All Gain Select pins open.

FIGURE 4 – MAXIMUM ALLOWABLE POWER DISSIPATION

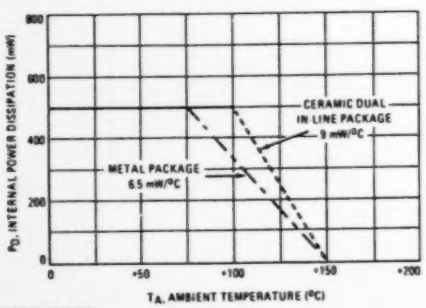

TYPICAL CHARACTERISTICS

(V_{CC} = +6.0 Vdc, V_{EE} = -6.0 Vdc, T_A = +25°C unless otherwise noted.)

FIGURE 5 – SUPPLY CURRENT versus TEMPERATURE

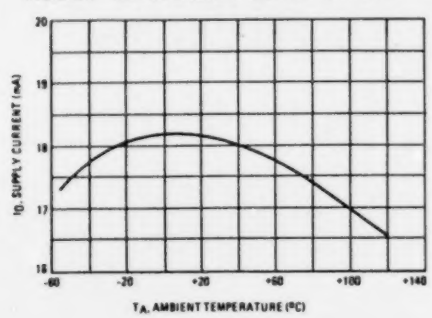

FIGURE 6 – SUPPLY CURRENT versus SUPPLY VOLTAGE

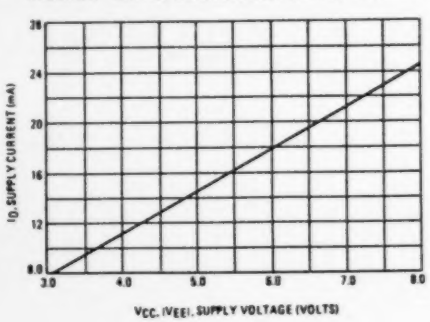

MC1733C (cont'd)

TYPICAL CHARACTERISTICS (continued)
(V_{CC} = +6.0 Vdc, V_{EE} = –6.0 Vdc, T_A = +25°C unless otherwise noted.)

FIGURE 7 – GAIN versus TEMPERATURE

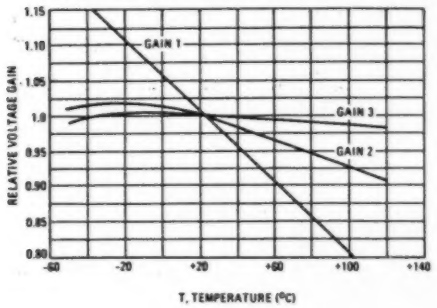

FIGURE 8 – GAIN versus FREQUENCY

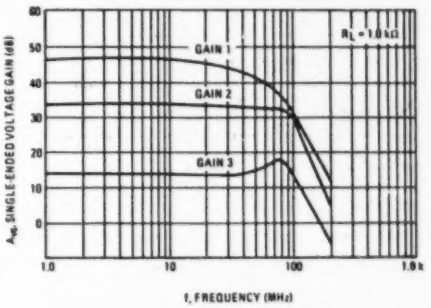

FIGURE 9 – GAIN versus SUPPLY VOLTAGE

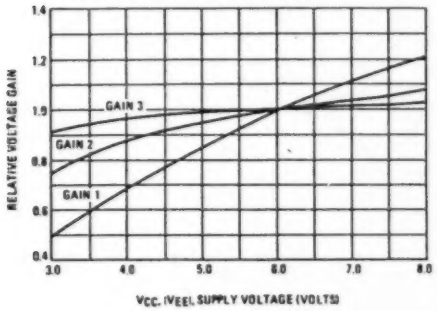

FIGURE 10 – GAIN versus R_{ADJUST}

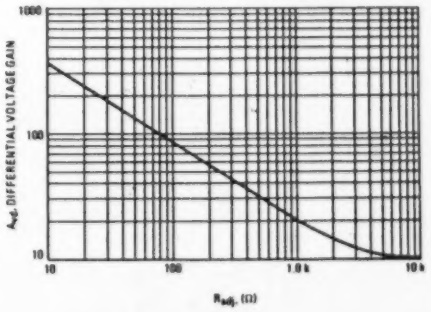

FIGURE 11 – GAIN versus FREQUENCY and SUPPLY VOLTAGE

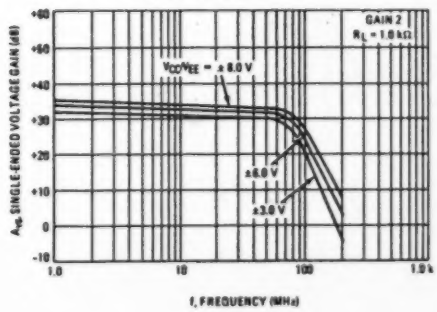

FIGURE 12 – GAIN versus FREQUENCY and TEMPERATURE

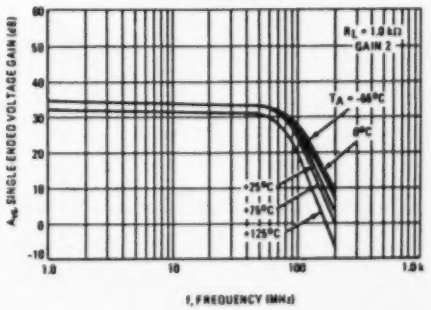

F.2.2 National Semiconductor LM6365

Absolute Maximum Rating

If Military/Aerospace specified devices are required, contact the National Semiconductor Sales Office/ Distributors for availability and specifications.

Supply Voltage ($V^+ - V^-$)	36V
Differential Input Voltage (Note 8)	±8V
CM Input Voltage	($V^+ - 0.7V$) To ($V^- - 7V$)
Output Short Circuit to Gnd (Note 1)	Continuous
Lead Temp (Soldering, 10 sec.)	260°C
Storage Temp Range	−65°C to 150°C
Operating Temperature Range (Note 2)	
LM6165	−55°C to +125°C
LM6265	−25°C to +85°C
LM6365	0°C to 70°C
Max Junction Temperature (Note 2)	150°C
ESD Tolerance (Notes 8 & 9)	±700V

DC Electrical Characteristics (Note 3)

Parameter	Conditions	Typ	LM6165		LM6265		LM6365		Units
			Tested Limit (Note 4)	Design Limit (Note 5)	Tested Limit (Note 4)	Design Limit (Note 5)	Tested Limit (Note 4)	Design Limit (Note 5)	
Input Offset Voltage		1	3 **4**		3	**4**	6	**7**	mV max
Input Offset Voltage Average Drift		3							µV/°C
Input Bias Current		2.5	3 **6**		3	**5**	5	**6**	µA max
Input Offset Current		150	350 **800**		350	**600**	1500	**1900**	na max
Input Offset Current Average Drift		0.3							nA/°C
Input Resistance	Differential	20							kΩ
Input Capacitance		6.0							pF
Large Signal Voltage Gain	V_{OUT} = ±10V, R_L = 2 kΩ (Note 11)	10.5	7.5 **5.0**		7.5	**6.0**	5.5	**5.0**	V/mV min
	R_L = 10 kΩ	38							
Input Common-Mode Voltage Range	Supply = ±15V	+14.0	+13.9 **+13.8**		+13.9	**+13.8**	+13.8	**+13.7**	V min
		−13.6	−13.4 **−13.2**		−13.4	**−13.2**	−13.3	**−13.2**	V min
	Supply = +5V (Note 6)	4.0	3.9 **3.8**		3.9	**3.8**	3.8	**3.7**	V min
		1.4	1.6 **1.8**		1.6	**1.8**	1.7	**1.8**	V max
Common-Mode Rejection Ratio	−10V ≤ V_{CM} ≤ +10V	102	88 **82**		88	**84**	80	**78**	dB min
Power Supply Rejection Ratio	±10V ≤ V± ≤ ±16V	104	88 **82**		88	**84**	80	**78**	dB min
Output Voltage Swing	Supply = ±15V and R_L = 2 kΩ	+14.2	+13.5 **+13.3**		+13.5	**+13.3**	+13.4	**+13.3**	V min
		−13.4	−13.0 **−12.7**		−13.0	**−12.8**	−12.9	**−12.8**	V min
	Supply = +5V and R_L = 2 kΩ (Note 6)	4.2	3.5 **3.3**		3.5	**3.3**	3.4	**3.3**	V min
		1.3	1.7 **2.0**		1.7	**1.9**	1.8	**1.9**	V max

LM6365 (cont'd)

DC Electrical Characteristics (Note 3) (Continued)

Parameter	Conditions	Typ	LM6165		LM6265		LM6365		Units
			Tested Limit	Design Limit	Tested Limit	Design Limit	Tested Limit	Design Limit	
			(Note 4)	(Note 5)	(Note 4)	(Note 5)	(Note 4)	(Note 5)	
Output Short Circuit Current	Source	65	30 **20**		30	**25**	30	**25**	mA min
	Sink	65	30 **20**		30	**25**	30	**25**	mA min
Supply Current		5.0	6.5 **6.8**		6.5	**6.7**	6.8	**6.9**	mA max

AC Electrical Characteristics (Notes 3 & 7)

Parameter	Conditions	Typ	LM6165		LM6265		LM6365		Units
			Tested Limit	Design Limit	Tested Limit	Design Limit	Tested Limit	Design Limit	
			(Note 4)	(Note 5)	(Note 4)	(Note 5)	(Note 4)	(Note 5)	
Gain-Bandwidth Product	@ F = 20 MHz	725	575 **400**		575	**475**	500	**400**	MHz min
	V+ = ±5V	500							
Slew Rate	A_V = +25 (Note 10)	300	225 **200**		225	**210**	200	**180**	V/μs min
	V+ = ±5V	200							
Power Bandwidth	V_{OUT} = 20 V_{PP}	4.5							MHz
Setting Time	10V Step to 0.1% A_V = −25, R_L = 2 kΩ	80							ns
Phase Margin	A_V = +25	45							Deg
Differential Gain	NTSC, A_V = +25	<0.1							%
Differential Phase	NTSC, A_V = +25	<0.1							Deg
Input Noise Voltage	F = 10 kHz	5							nV/√Hz
Input Noise Current	F = 10 kHz	1.5							pA/√Hz

Note 1: Continuous short-circuit operation at elevated ambient temperature can result in exceeding the maximum allowed junction temperature of 150°C.

Note 2: The typical junction-to-ambient thermal resistance of the molded plastic DIP (N) is 105°C/Watt, the molded plastic SO (M) package is 155°C/Watt, the cerdip (J) package is 125°C/Watt, and the TO-5 (H) package is 155°C/Watt. All numbers apply for packages soldered directly into a printed circuit board.

Note 3: Unless otherwise specified, all limits guaranteed for $T_a = T_j = 25°C$ with supply voltage = ±15V, V_{CM} = 0V, and $R_L \geq 100$ kΩ. **Boldface** limits apply over the range listed under "Operating Temperature Range".

Note 4: Guaranteed and 100% production tested. These limits are used to calculate outgoing AQL levels.

Note 5: Guaranteed but not 100% production tested. These limits are not used to calculate outgoing AQL levels.

Note 6: For single supply operation, the following conditions apply: V+ = 5V, V− = 0V, V_{CM} = 2.5C, V_{OUT} = 2.5V. Pin 1 & Pin 8 (V_{OS} Adjust) are each connected to Pin 4 (V−) to realize maximum output swing. This connection will degrade V_{OS}.

Note 7: $C_L \leq 5$ pF.

Note 8: In order to achieve optimum AC performance, the input stage was designed without protective clamps. Exceeding the maximum differential input voltage results in reverse breakdown of the base-emitter junction of one of the input transistors and probable degradation of the input parameters (especially V_{OS}, I_{OS}, and Noise).

Note 9: The average voltage that the weakest pin combinations (those involving Pin 2 or Pin 3) can withstand and still conform to the datasheet limits. The test circuit used consists of the human body model of 100 pF in series with 1500Ω.

Note 10: V_{IN} = 0.7V step. For V+ = ±5V, V_{IN} = 0.2V step.

Note 11: Voltage Gain is the total output swing (20V) divided by the input signal required to produce that swing.

G Circuit design documentation

G.1 Driver for quantum-well laser diodes

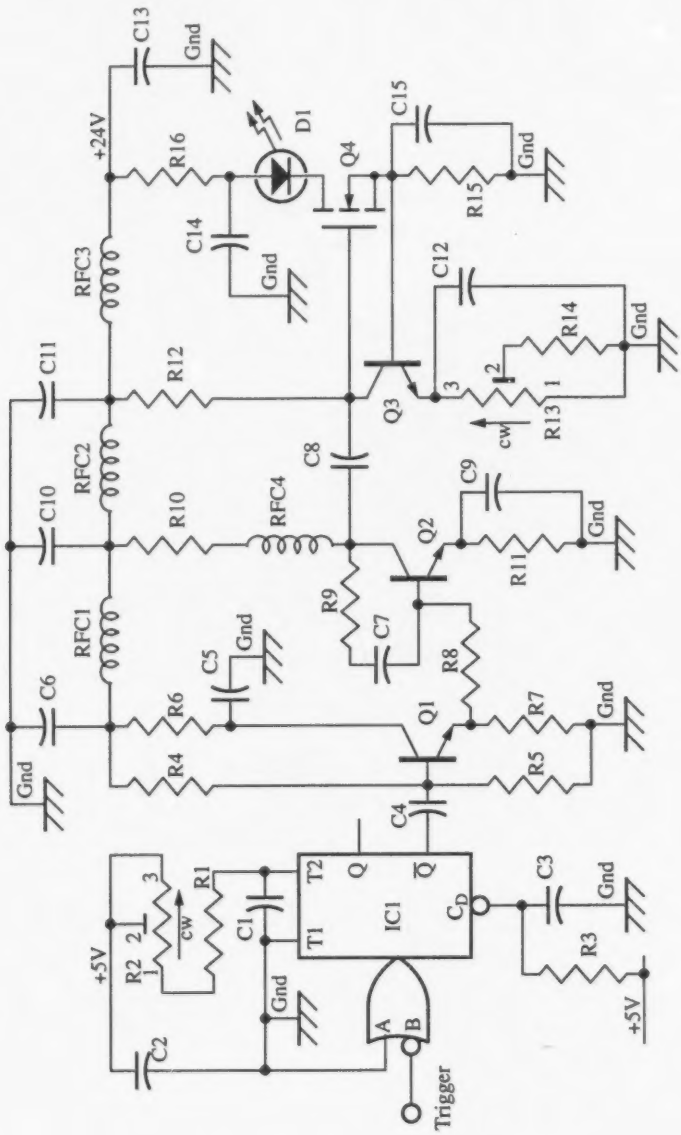

Circuit component layout (1.5 ×)

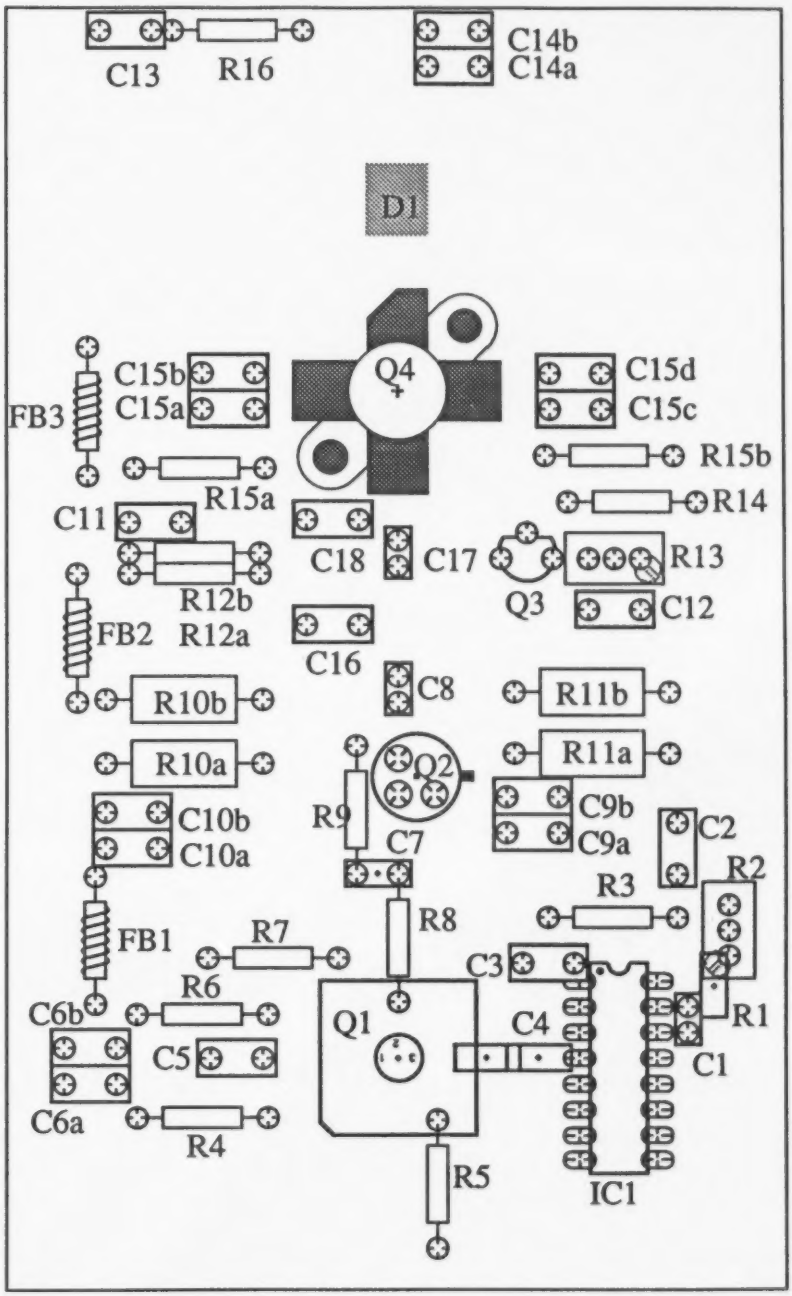

Photomasks (a) component side (b) wiring side

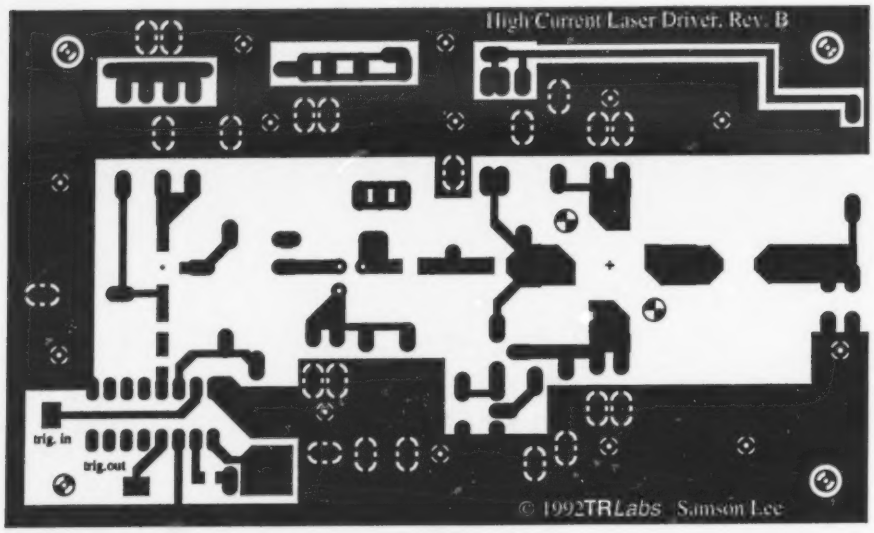

(a)

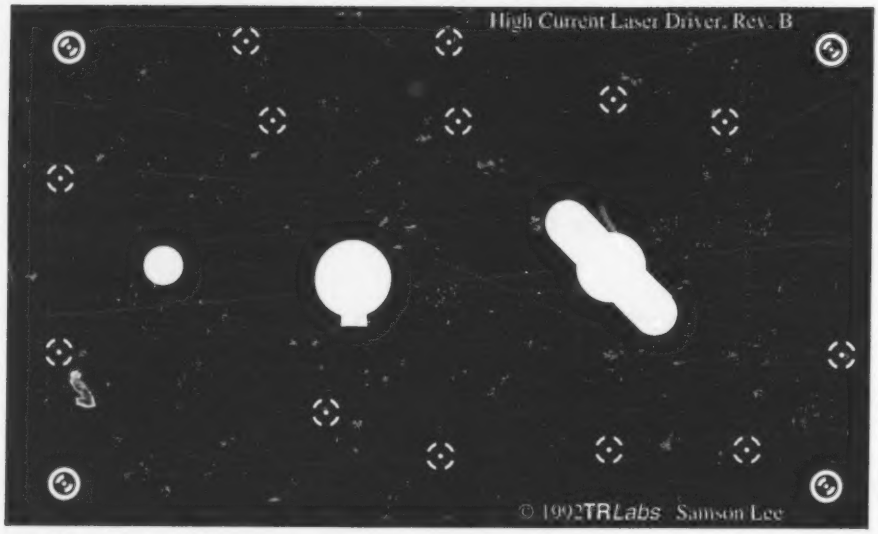

(b)

Part Lists

Table 6 Part List for High Current Laser Driver, Revision B

Resistor	*Value*	*Tol. (%)*	*Power (W)*	*Type*	*Manufacturer*
R1	100R	1	1/8	surface mount	Mallory
R2	100R	10	1/2	single-turn pot	VRN Int'l
R3	1k0	1	1/4	metal film	various
R4	10k	1	1/4	metal film	various
R5	3k3	1	1/4	metal film	various
R6	680R	1	1/4	metal film	various
R7	200R	1	1/4	metal film	various
R8	100R	1	1/4	metal film	various
R9	270	1	1/4	metal film	various
R10a	47R	5	2	wire wound	various
R10b	47R	5	2	wire wound	various
R11a	33R	5	2	wire wound	various
R11b	33R	5	2	wire wound	various
R12	2k0	1	1/4	metal film	various
R13	100R	10	1/2	multi-turn pot	VRN Int'l
R14	100R	1	1/4	metal film	various
R15	100R	1	1/4	metal film	various
R15b	100R	1	1/4	metal film	various
R16	47R	1	1/4	metal film	various

Capacitor	*Value*	*Tol. (%)*	*Voltage (W)*	*Type*	*Manufacturer*
C1	68p	20	50	mono. ceramic	various
C2	1µ0	20	35	electrolytic	various
C3	330n	20	50	mono. ceramic	various
C4	100n	10	50	mono. ceramic	various
C5	1µ0	10	35	electrolytic	various
C6a	2µ2	20	35	electrolytic	various
C6b	100n	20	50	mono. ceramic	various
C7	100n	20	50	mono. ceramic	various

Part List for High Current Laser Driver [cont'd]

Capacitor	*Value*	*Tol. (%)*	*Voltage (W)*	*Type*	*Manufacturer*
C8	100n	10	50	mono. ceramic	various
C9a	2m2	20	50	mono. ceramic	various
C9b	2m2	20	50	mono. ceramic	various
C10a	2m2	20	50	electrolytic	various
C10b	10n	20	50	mono. ceramic	various
C11	100n	10	50	mono. ceramic	various
C12	2m2	20	50	mono. ceramic	various
C13	1m0	20	50	mono. ceramic	various
C14a	2m2	20	50	mono. ceramic	various
C14b	2m2	20	50	mono. ceramic	various
C15a	2m2	20	50	mono. ceramic	various
C15b	2m2	20	50	mono. ceramic	various
C15c	2m2	20	50	mono. ceramic	various
C15d	2m2	20	50	mono. ceramic	various

Semiconductor	*Description*	*Manufacture*	*Part no.*
D1	Quantum-well laser		
Q1	Low power UHF NPN	Motorola	BFR90
Q2	Medium power HF NPN	Motorola	2N3866A
Q3	General purpose NPN	National	2N4401
Q4	Power MOSFET	Motorola	MFR136
IC1	Dual TTL monostable	National	74LS123

Miscellaneous	*Description*	*Manufacturer*	*Part no.*
RFC1	Ferrite bead	Amidon	FB-43-6301
RFC2	Ferrite bead	Amidon	FB-43-6301
RFC3	Ferrite bead	Amidon	FB-43-6301
RFC4	10-µH Inductor	Miller	9230-44
	Heat sink for Q2	Wakefield	623A

G.2 OTDR Receiver Revision C

Schematic circuit diagram

Note: supply line decoupling and filtering elements are not shown.

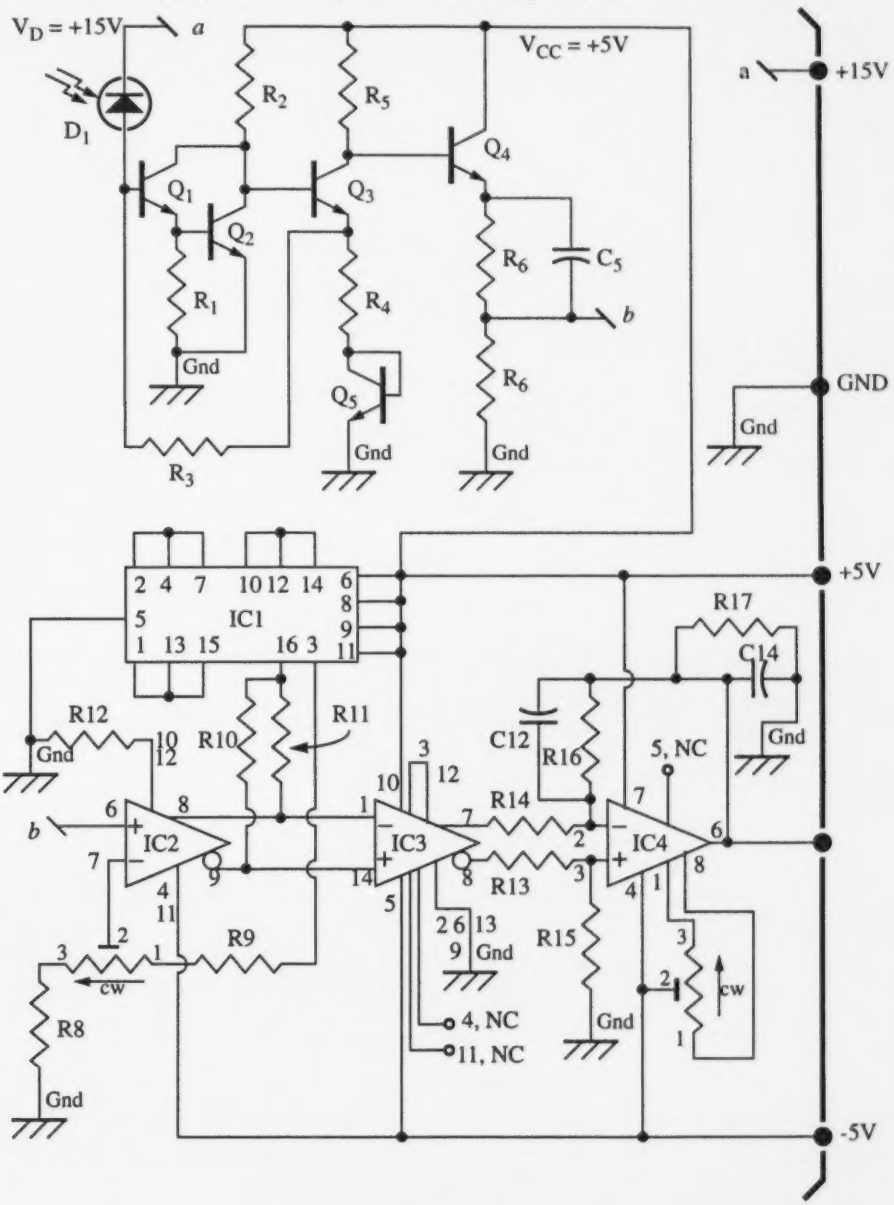

Circuit board component layout (1.5 ×)

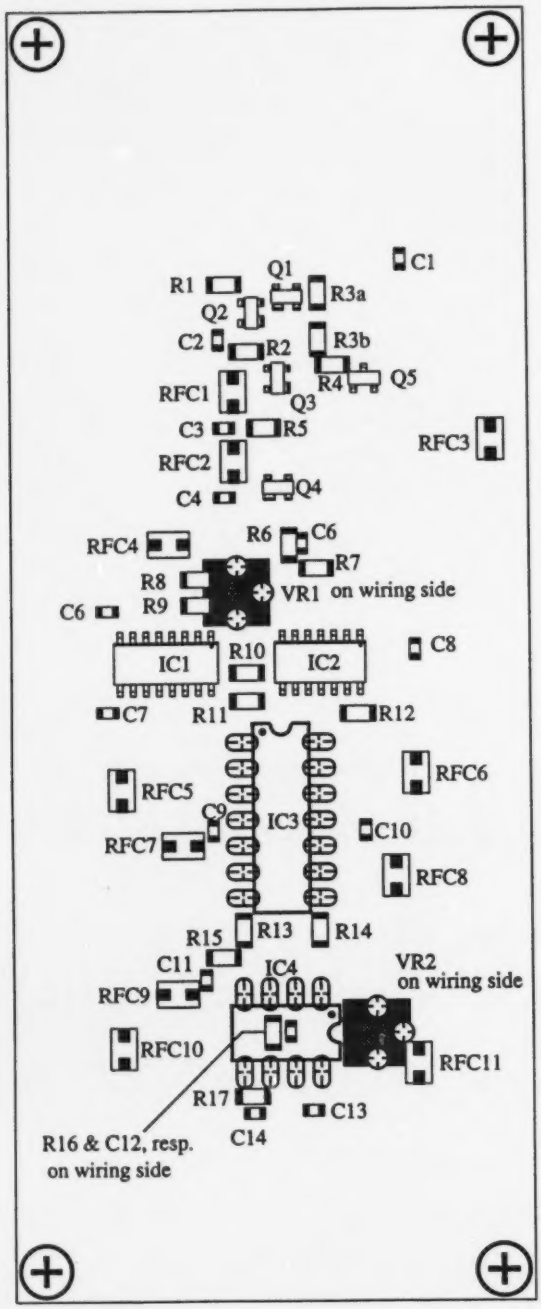

Ciruict board layout (a) component side (b) wiring side

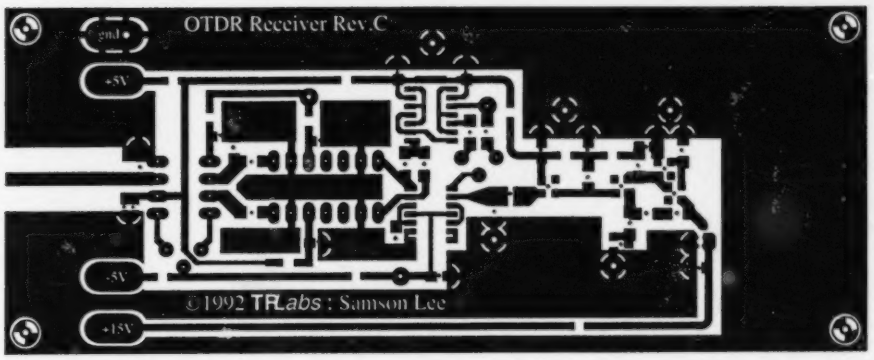

(a)

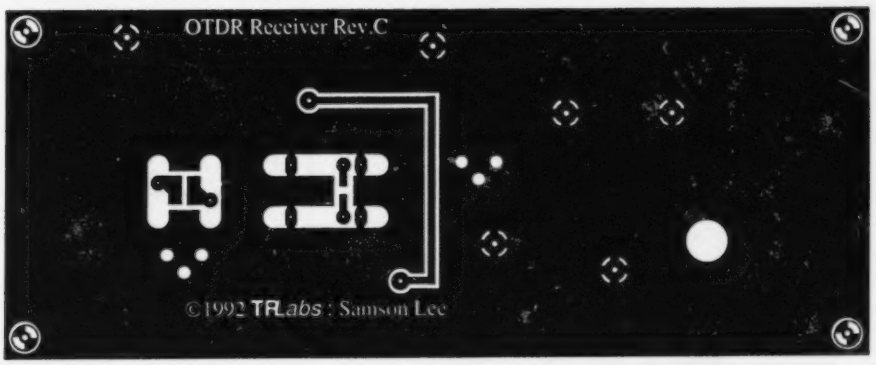

(b)

Part Lists

Table 7 Part List for OTDR Receiver, Revision C

Resistor	*Value*	*Tol. (%)*	*Power (W)*	*Type*	*Manufacturer*
R1	10k0	1	1/8	surface mount	Mallory
R2	1k20	1	1/8	surface mount	Mallory
R3a	33k0	1	1/8	surface mount	Mallory
R3b	39k0	1	1/8	surface mount	Mallory
R4	510R	1	1/8	surface mount	Mallory
R5	510R	1	1/8	surface mount	Mallory
R6	1k80	1	1/8	surface mount	Mallory
R7	220R	1	1/8	surface mount	Mallory
R8	220R	1	1/8	surface mount	Mallory
R9	1k80	1	1/8	surface mount	Mallory
R10	49R9	1	1/8	surface mount	Mallory
R11	49R9	1	1/8	surface mount	Mallory
R12	330R	1	1/8	surface mount	Mallory
R13	47R0	1	1/8	surface mount	Mallory
R14	220R	1	1/8	surfacemount	Mallory
R15	180R	1	1/8	surface mount	Mallory
R16	820R	1	1/8	surface mount	Mallory
R17	Reserved for frequency compensation.				
VR1	100R	10	1/2	multi-turn pot	Bourn
VR2	100k	10	1/2	multi-turn pot	Bourn

Capacitor	*Value*	*Tol. (%)*	*Voltage (W)*	*Type*	*Manufacturer*
C1	10n	20	50	surface mount	various
C2	10n	20	50	surface mount	various
C3	10n	20	50	surface mount	various
C4	10n	20	50	surface mount	various
C5	15p	20	25	surface mount	various
C6	10n	20	50	surface mount	various

Part List for High Current Laser Driver [cont'd]

Capacitor	*Value*	*Tol. (%)*	*Voltage (W)*	*Type*	*Manufacturer*
C7	10n	20	50	surface mount	various
C8	10n	20	50	surfacemount	various
C9	100n	20	50	surfacemount	various
C10	100n	20	50	surfacemount	various
C11	10n	20	50	surfacemount	various
C12	10n	20	50	surfacemount	various
C13	100n	20	50	surfacemount	various
C14	Reserved for frequency compensation.				

Semiconductor	*Description*	*Manufacture*	*Part no.*
D1	Photo-detector	various	
Q1	Low power UHF NPN	Motorola	MRF9331L
Q2	Low power UHF NPN	Motorola	MRF9331L
Q3	Low power UHF NPN	Motorola	MRF9331L
Q4	Low power UHF NPN	Motorola	MRF9331L
Q5	Low power UHF NPN	Motorola	MMBR931L
IC1	UHF NPN array	Plessey	SL3227ML
IC2	UHF NPN array	Plessey	SL2365ML
IC3	Video amplifier	Motorola	MC1733CP
IC4	Wideband op-amp	National	LM6365P

Miscellaneous	*Description*	*Manufacturer*	*type*
RFC1 through RFC11	Ferrite bead	various	surfacemount